

Contents lists available at ScienceDirect

# Mechanical Systems and Signal Processing

journal homepage: www.elsevier.com/locate/ymssp



# Reduced order modeling for the dynamics of jointed structures through hyper-reduced interface representation



Nidish Narayanaa Balaji <sup>a</sup>, Tobias Dreher <sup>b</sup>, Malte Krack <sup>b</sup>, Matthew R.W. Brake <sup>b,\*</sup>

#### ARTICLE INFO

Article history: Received 2 January 2020 Received in revised form 12 May 2020 Accepted 27 August 2020

Keywords: Reduced Order Modeling Interface Reduction Hyper Reduction Interfacial Mechanics Jointed Structures

#### ABSTRACT

One strategy to develop both accurate and computationally tractable models of jointed structures is reduced order modeling through hyper-reduced representations of the interfaces in contact. Hyper reduction refers to reduction techniques that result in a Reduced Order Model (ROM) that is complete by itself, i.e., all displacements and forces are fully described in the ROM coordinates directly. Focusing primarily on applications involving small relative displacement contacts, two fundamentally different approaches are formulated and compared for merits and limitations in applicability. The first is an adaptation of the stiffness-preserving RBE3 constraint elements, and the second is an interpolation approach based on remeshing the interface. Although RBE3 is extensively used in the literature, the current formulation derives stiffness preserving elements that are specifically useful for contact dynamics applications. Transformations are developed to express force-displacement relationships in the ROM coordinates that are congruent (in the sense of using the same contact models) as well as consistent (in the sense of being faithful to the quantities involved) with a high-fidelity model of the same structure. These approaches are applied to study a three-bolted lap-joint structure (the Brake-Reuß Beam (BRB) benchmark) that has been observed to demonstrate characteristic contact non-linearities. Multiple strategies for the hyper reduction are evaluated, including graph partitioning, finite element coarsening, and homogenization of field objectives, some of which involve an extra step of remeshing/choosing patches based on a field objective (e.g., contact pressure). The performances of the ROMs are assessed by conducting nonlinear modal analysis and computing a posteriori error metrics.

© 2020 Elsevier Ltd. All rights reserved.

#### 1. Introduction

The study of mechanical joints, and interfacial mechanics more broadly, has been a topic at the forefront of advances in efficiency and design within the aero-turbine, aerospace, automotive, and naval industries. Much of the recent research efforts in joint mechanics can be attributed to the efforts of Prof. Lothar Gaul who helped consolidate the state-of-the-art following SD2000 [29]. For this special issue dedicated to the late Prof. Gaul, the authors wish to express their gratitude

<sup>&</sup>lt;sup>a</sup> Department of Mechanical Engineering, Rice University, Houston, TX 77005, USA

<sup>&</sup>lt;sup>b</sup> Institute of Aircraft Propulsion Systems, University of Stuttgart, Keplerstraße 7, 70174 Stuttgart, Germany

<sup>\*</sup> Corresponding author.

E-mail addresses: nb25@rice.edu (N.N. Balaji), tdreher.ahausen@web.de (T. Dreher), malte.krack@ila.uni-stuttgart.de (M. Krack), brake@rice.edu (M.R.W.

for all of his efforts in establishing the presently flourishing research community, and the collaboration for this research in particular.

One major challenge within computational structural mechanics is model size reduction for systems with frictional and contact nonlinearities in order to make computationally tractable models. For systems with localized non-linearities (such as a jointed structure), linear reduction techniques (such as component mode synthesis approaches [20,28,19,9,52]) are typically employed to reduce the linear regions of the structure. Further reduction of the Degrees-of-Freedom (DoFs) of the non-linear regions (contacting interface in a jointed structure) forms the primary focus of the current work.

Even for relatively simple jointed structures, the representational requirements, as well as the amount of nonlinear evaluations necessary, can make the resulting system of equations both large as well as very costly for simulation. Contact nonlinearities are usually modeled using non-linear models that offer amplitude-dependent stiffness and hysteretic damping [25]. In the case of bolted joints, fine interfacial discretizations are usually necessary in order to capture the potentially complex stick–slip interactions, which arise due to the highly inhomogeneous pressure distribution. These interactions are often termed 'microslip' as part of the interface is sliding and part of the interface is stuck (as opposed to 'macroslip', defined as gross sliding, in which the entire interface is in slip, a condition rarely seen in bolted joints). While the main purpose of bolted joints is to align two sub-components together, these joints have been known to have significant influences in the dissipative characteristics of the structure.

Classical linear projection-based reduced order modeling approaches [22,17,50,36] alleviate the first issue above (representational requirements) by constructing reduced systems of equations that represent the complete model in a reduced form (using linear bases) through a projection [51]. More recently, there have also been some studies that have considered the second challenge (nonlinear evaluation overhead), namely "hyper-reduction" approaches [53,31]. First coined in [55], the term "hyper-reduction" refers to the reduction of a system of equations in such a way that it yields a Reduced Order Model (ROM) that is a complete description of the full order model, i.e., no evaluations in the original coordinates are necessary to obtain the forcing terms for the ROM. These methods result in the system evaluation cost scaling with the size of the ROM, which is a claim that may not be made for projection-based approaches.

There have been several recent approaches, such as in [54,32], where the projection ROMs are trained based on the forcing on the original model for the hyper-reduction step. This would involve expensive (one-time) full order model simulations for the training. Further, such approaches suffer from data-dependency and are known to extrapolate poorly in the general case for forcing amplitudes outside of the training regime. Although there have been improvements with regards to the first drawback (e.g., [30]), where manifold mapping has been successfully employed to do this without expensive simulations, the second drawback still remains. The current work, however, seeks to develop a hyper-reduction approach that is not training-based, and hence would not suffer from the drawbacks mentioned above.

The rest of the paper is organized as follows: section 2 details the mathematical formulations of the patch (in section 2.1) and the remeshing (in section 2.2) reduction approaches; and section 3 presents numerical applications of the developed strategies for a linear case (section 3.1) and a non-linear bolted joint case (section 3.2). In section 3.1 the developed techniques are applied for reduced representations of a surface that is a part of a linear elastic beam, and is mainly intended to highlight various aspects of the ROM strategies that can be observed using linear analyses, while section 3.2 conducts non-linear contact analyses, which form the primary purpose of the current effort. Finally, section 4 concludes the paper with a summary of contributions, key takeaways, and possible directions for future research.

#### 2. Interface reduction approaches

One main challenge with modeling structures with interfaces in contact is the sheer number of discretizations necessary for interfacial representation, as previously mentioned. In usual practice, standard Component Mode Synthesis (CMS) procedures (a popular example being the Hurty/Craig-Bampton (HCB) CMS [28,19]) are applied to represent the "linear portions" of the structure using component modes, while retaining the non-linear DoFs without any reduction (specifically, the contact nodal DoFs). For many tasks,  $\mathcal{O}\left(10^1\right)$  fixed interface modes (in HCB-CMS) are sufficient, while  $\mathcal{O}\left(10^2-10^3\right)$  nodal DoFs are involved for the interfacial representation. While these models (sometimes referred to as substructured models) are smaller in size than the original model, these are still large for computational purposes in practice. The interfacial Degrees-of-Freedom (DoFs) need to be reduced further in order to make the system more tractable for analysis (see [36] for a review of some classical approaches). Some of these methods seek to represent the interfacial DoFs as a linear combination of additional component modes by projection resulting in the introduction of generalized coordinates, which do not have readily apparent physical meanings (see [50] for a recent example). The approaches in the current paper, on the other hand seek physically meaningful ROMs by construction.

Two approaches, with very different formulations and properties, are formulated and explored here. For an unbiased comparison, identical contact models are employed across the reference Finite Element Model (FEM) and all of the ROMs. Unilateral penalty linear springs and coupled-planar elastic-dry friction elements are employed in the interface normal and tangential directions respectively.

The first method explored here (presented in section 2.1) introduces virtual nodes without any independent dynamics, which are constrained by their relationships with the interfacial nodal DoFs. This approach is similar but not identical in formulation to the popularly used "whole-joint" or patch approach [44,12,5,57,43,45] in bolted structures. The idea is to first

divide the interface into several partitions and simplify the kinematic descriptions on each partition to be only first order accurate (using displacement and rotations only). This does not reduce the system size, but using a substructuring step after this can make for a reduction that provides a representation with much fewer DoFs. Similar "elements" are implemented in commercial finite element software (such as ABAQUS, ANSYS, etc.) and are known by various names such as the RBE3 element [44,5], distributing coupling elements [45], etc. In these implementations, a user-defined weighting is introduced to distribute the forces on the coupling elements to the "slave" Degrees-of-Freedom (DoFs). In the current work, the implementation is conducted in a more convenient element-wise fashion using quadrature integration and the weights thereof instead of the nodes and user-defined weighting functions. Contiguous (path-connected) patches on the interface are chosen for the ROM based on different criteria such as weighted graph clustering and binning field objectives on level sets. Different numbers of graph clusters and level sets are demonstrated to provide progressively better representations. The multilevel graph partitioning approach in [33] is employed for the graph partitioning and static pressure and modal displacement fields are used as field objectives for the level-sets partitioning approach (see section 2.1.2 for details).

The second approach (presented in section 2.2) is based on a consistent representation of the interface using a coarser finite element mesh. Taking inspiration from a Voronoi patch approach for discretizing an interface [40], this paper develops consistent transformations for a hyper-reduced ROM. Previous efforts in the current direction include [21], where a simplified ROM formulation that was based on nodal interpolation was used. However, an improved formulation is developed here that is weak-form consistent. This yields a physically meaningful ROM with a coarser mesh that may be interpreted similarly (but not identically) to a finite element mesh. Appropriate transformations are developed to represent the DoFs as well as forces completely in the reduced domain. Two classes of mesh coarsening are also explored, with one involving uniform coarsening and the other involving a field objective similar to the ones used in the previous case (see section 2.2.2 for details).

#### 2.1. Whole-joint reduced order modeling

#### 2.1.1. Formulation

The Whole-Joint Reduced Order Modeling (WJROM) approach introduces additional DoFs, referred to as virtual node DoFs or simply virtual DoFs, which is a "lumped" or "averaged" representation of the deformation in a particular region. A schematic of a typical application scenario is provided in Fig. 1. There is a region  $\Gamma$  discretized by the mesh, and a "virtual" node placed at location  $x_v \in \mathbb{R}^3$  with Cartesian coordinates  $(x_v, y_v, z_v)$ . Three translational  $(u_x^v, u_v^v, u_z^v)$  and three rotational DoFs

 $(\theta_x^v, \theta_y^v, \theta_z^v)$  are defined for the virtual node to develop a representation of the kinematics of the meshed region. This is done by establishing a point-wise relationship between the DoFs at each point on  $\Gamma$  and the virtual node DoFs. For a point P with position vector  $x \in \Gamma$  with coordinates (x, y, z), the DoFs  $u_x, u_y, u_z$  are represented as

$$\underbrace{u_x \hat{x} + u_y \hat{y} + u_z \hat{z}^{\underline{u}(\underline{x})}}_{\sim} = u_x^{\nu} \hat{x} + u_y^{\nu} \hat{y} + u_z^{\nu} \hat{z} + \left(\theta_x^{\nu} \hat{x} + \theta_y^{\nu} \hat{y} + \theta_z^{\nu} \hat{z}\right) \times \left(\underbrace{(x - x_{\nu}) \hat{x} + (y - y_{\nu}) \hat{y} + (z - z_{\nu})}_{\sim} \hat{z}^{\underline{x} - \underline{x_{\nu}}}\right). \tag{1}$$

The unit vectors  $\hat{x}, \hat{y}, \hat{z}$  represent the basis vector components of the physical space. Expanding the cross product and representing the DoFs in component-vector notation, this is equivalently written as

$$\underbrace{\begin{cases} u_{x}(\underline{x}) \\ u_{y}(\underline{x}) \\ u_{z}(\underline{x}) \\ u_{z}(\underline{x}) \end{cases}}_{\underline{y}(\underline{x})} = \underbrace{\begin{bmatrix} 1 & 0 & 0 & 0 & (z-z_{v}) & -(y-y_{v}) \\ 0 & 1 & 0 & -(z-z_{v}) & 0 & (x-x_{v}) \\ 0 & 0 & 1 & (y-y_{v}) & -(x-x_{v}) & 0 \end{bmatrix}}_{\underline{\mathbf{g}}(\underline{x})} \underbrace{\begin{cases} u_{x}^{v} \\ u_{y}^{v} \\ u_{z}^{v} \\ \theta_{x}^{v} \\ \theta_{y}^{v} \\ \theta_{z}^{v} \end{cases}}_{\{u^{v}\}}.$$
(2)

Using the indicated notations  $(\mathbf{g}: \mathbb{R}^3 \to \mathbb{R}^{3 \times 6})$  and a finite element representation for u(x) through appropriate shape functions  $\mathbf{n}(x)$  and nodal DoFs  $\{u^n_{\widetilde{u}}\}$ , this yields the following point-wise relationship between nodal DoFs  $\{u^n_{\widetilde{u}}\}$  and the virtual DoFs  $\{u^n_{\widetilde{u}}\}$ :

$$\{\underbrace{u(\underline{x})}\} = \underbrace{n(\underline{x})\{u^n\}}_{\text{virtual DoF relationship}} = g(\underline{x})\{\underline{u}^v\} \qquad \underline{x} \in \Gamma.$$

$$(3)$$

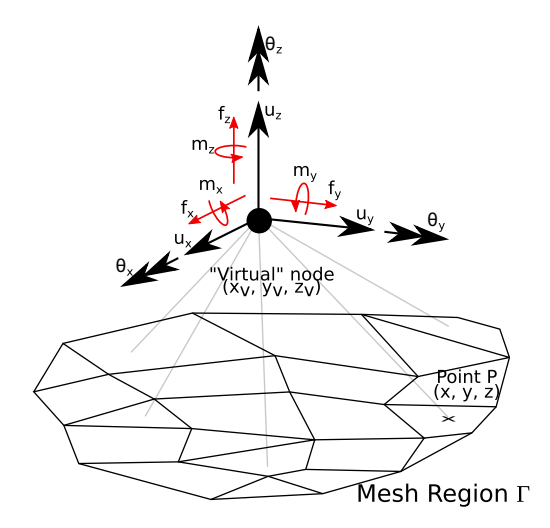


Fig. 1. Schematic illustration for a whole joint application. The degrees of freedom and forcing components are denoted using black and red arrows respectively.

The matrix-valued function  $\mathbf{g}(x)$  is used to represent the point-wise mapping of the virtual node DoFs and the finite element DoFs (Eq. 2) throughout the rest of this section.

In order to develop a consistently hyper-reduced formulation, Eq. 3 is substituted into the virtual work expression to yield

$$\delta W^{\nu} = \int_{\Gamma} \delta \underbrace{u}_{\mathcal{X}} \left( \underbrace{x} \right)^{T} \underbrace{t}_{\mathcal{X}} \left( \underbrace{x} \right) d\Gamma 
= \int_{\Gamma} \left( \mathbf{g} \left( \underbrace{x} \right) \left\{ \delta \underbrace{u}_{\mathcal{U}}^{\nu} \right\} \right)^{T} \underbrace{t}_{\mathcal{X}} \left( \underbrace{x} \right) d\Gamma \quad \text{(fromeq.3)} 
= \left\{ \delta \underbrace{u}^{\nu} \right\}^{T} \int_{\Gamma} \mathbf{g} \left( \underbrace{x} \right)^{T} \underbrace{t}_{\mathcal{X}} \left( \underbrace{x} \right) d\Gamma,$$
(4)

where  $\underline{t}(\underline{x}) = [t_x(\underline{x}), t_y(\underline{x}), t_z(\underline{x})]^T$  denotes the point-wise tractions in component-vector form,  $\delta \underline{u}(\underline{x})$  denotes a virtual displacement field, and  $\delta W^{\nu}$  denotes the virtual work contribution through the region  $\Gamma$ . Next, the point-tractions are rewritten using forces (f) and moments (m) on the virtual node. Considering an infinitesimal area  $d\Gamma$  on the patch, the following relationships are used:

$$\begin{cases}
t_{x}(\underline{x}) \\ t_{y}(\underline{x}) \\ t_{z}(\underline{x})
\end{cases} d\Gamma = \begin{cases}
f_{x}^{v} \\ f_{y}^{v} \\ f_{z}^{v}
\end{cases} \frac{d\Gamma}{\mathbf{a}_{v}} + 
\begin{bmatrix}
0 & (z - z_{v}) & -(y - y_{v}) \\ -(z - z_{v}) & 0 & (x - x_{v}) \\ (y - y_{v}) & -(x - x_{v}) & 0
\end{bmatrix} 
\underbrace{\begin{bmatrix}
I_{xx} & I_{xy} & I_{xz} \\ I_{yx} & I_{yy} & I_{yz} \\ I_{zx} & I_{zy} & I_{zz}
\end{bmatrix}^{-1} \begin{pmatrix} m_{x}^{v} \\ m_{y}^{v} \\ m_{z}^{v} \end{pmatrix}}_{\mathbf{d}\Gamma;$$
(5)

Here,  $\mathbf{a}_v$  and  $\mathbf{I}_v$  denote the total area of the patch and the matrix form of the second moment of area tensor respectively (observe that  $\mathbf{I}_v = \int_{\Gamma} \mathscr{I}_v(\mathbf{x}) d\Gamma$ ). Eq. 5 relates the traction and virtual node forces and moments (virtual forcing terms) on  $d\Gamma$  in a manner that is equivalent to the classic bolt-pattern force distribution (see [10]). For the distributing coupling elements in ABAQUS  $^1$ , a similar expression is employed, except that it is applied to relate nodal forces to the virtual forcing terms using user-defined weighting to define the distribution. The current expression does not involve any user-defined weight distribution since Eq. 5 is developed at the traction-level.

Evaluating the cross product of the relative location of each point with both sides in Eq. 5 yields

<sup>1</sup> See "Elements > Special-purpose elements > Distributing coupling constraints" in the theory manual [45] (Section 3.9.8 in the 2014 version)

$$\underbrace{\begin{bmatrix}
0 & -(z - z_{v}) & (y - y_{v}) \\
(z - z_{v}) & 0 & -(x - x_{v}) \\
-(y - y_{v}) & (x - x_{v}) & 0
\end{bmatrix}}_{\{z - z_{v}\}} \underbrace{\begin{cases}
t_{y}(\underline{x}) \\
t_{y}(\underline{x}) \\
t_{z}(\underline{x})
\end{cases}}_{\{t_{z}(\underline{x})\}} d\Gamma = \begin{bmatrix}
0 & -(z - z_{v}) & (y - y_{v}) \\
(z - z_{v}) & 0 & -(x - x_{v}) \\
-(y - y_{v}) & (x - x_{v}) & 0
\end{bmatrix}}_{\{z - z_{v}\}} \underbrace{\begin{cases}
t_{y} \\
t_{y} \\
t_{z}
\end{cases}}_{\{z - z_{v}\}} d\Gamma$$

$$+ \mathcal{I}_{v}(\underline{x}) \mathbf{I}_{v}^{-1} \begin{Bmatrix} m_{x} \\
m_{y} \\
m_{z}^{v} \\
m_{z}^{v}
\end{Bmatrix}}_{\{z - z_{v}\}} d\Gamma,$$
with, 
$$\mathcal{I}_{v}(\underline{x}) = \begin{bmatrix}
(y - y_{v})^{2} + (z - z_{v})^{2} & -(x - x_{v})(y - y_{v}) & -(x - x_{v})(z - z_{v}) \\
(x - x_{v})^{2} + (z - z_{v})^{2} & -(y - y_{v})(z - z_{v}) \\
sym & (x - x_{v})^{2} + (y - y_{v})^{2}
\end{bmatrix}.$$

This is the relationship between the whole-joint forcing terms and the local contributions to the moment.

Using these, and choosing the centroid of the patch as the location of the virtual node, the term  $\int_{\Gamma} \mathbf{g}(x)^{T} \underbrace{\mathcal{L}}(x) d\Gamma$  simplifies as:

$$\int_{\Gamma} \mathbf{g}(x)^{\mathsf{T}} t(x) d\Gamma = \int_{\Gamma} \begin{bmatrix} 1 & 0 & 0 \\ 0 & 1 & 0 \\ 0 & 0 & 1 \\ 0 & -(z-z_{v}) & (y-y_{v}) \\ (z-z_{v}) & 0 & -(x-x_{v}) \end{bmatrix} \begin{cases} t_{x}(x) \\ t_{y}(x) \\ t_{z}(x) \end{cases} d\Gamma$$

$$= \begin{cases}
\int_{\Gamma} \frac{d\Gamma}{a_{v}} \cdot \begin{cases} f_{x}^{v} \\ f_{y}^{v} \\ f_{z}^{v} \end{cases} + \int_{\Gamma} \begin{bmatrix} 0 & -(z-z_{v}) & (y-y_{v}) \\ (z-z_{v}) & 0 & -(x-x_{v}) \end{bmatrix} d\Gamma \cdot \mathbf{I}_{v}^{-1} \begin{cases} m_{x}^{v} \\ m_{y}^{v} \\ m_{z}^{v} \end{cases} \\
= \begin{cases}
\int_{\Gamma} \frac{d\Gamma}{a_{v}} \cdot \begin{cases} f_{x}^{v} \\ f_{y}^{v} \\ f_{z}^{v} \end{cases} - (y-y_{v}) & (x-x_{v}) & 0
\end{cases} d\Gamma \cdot \mathbf{I}_{v}^{-1} \begin{pmatrix} m_{x}^{v} \\ f_{y}^{v} \\ f_{z}^{v} \end{cases} \\
+ \int_{\Gamma} \begin{bmatrix} (y-y_{v})^{2} + (z-z_{v})^{2} & -(x-x_{v})(y-y_{v}) & -(x-x_{v})(z-z_{v}) \\ (x-x_{v})^{2} + (z-z_{v})^{2} & -(y-y_{v})(z-z_{v}) \end{cases} d\Gamma \cdot \mathbf{I}_{v}^{-1} \begin{pmatrix} m_{x}^{v} \\ m_{y}^{v} \\ m_{z}^{v} \end{pmatrix} \\
= \begin{cases}
f_{x}^{v} \\ f_{y}^{v} \\ f_{z}^{v} \\ m_{x}^{v} \\ m_{x}^{v} \end{cases} \triangleq \begin{cases}
f_{x}^{v} \\ f_{y}^{v} \\ f_{z}^{v} \end{cases} ((x_{v}, y_{v}, z_{v}) \text{ is the centroid of } \Gamma).
\end{cases}$$

Substituting this into Eq. 4 yields the virtual work contribution of the patch  $\Gamma$ ,

$$\delta W^{v} = \left\{ \delta \underset{\sim}{\overset{v}{u}} \right\}^{T} \left\{ \underset{\sim}{\overset{v}{f}} \right\}.$$

This is identical to the virtual work done by a virtual node's virtual displacements (translations and rotations) due to the corresponding virtual forcing terms (forces and moments).

The weak form (interpreted as the principle of virtual work) of a generic finite element model is given, in terms of its nodal displacement vector  $\left\{ \stackrel{n}{\underline{u}} \right\} \in \mathbb{R}^{|n|}$ , stiffness matrix  $\mathbf{K} \in \mathbb{R}^{|n| \times |n|}$  and forcing vector  $\left\{ f \right\} \in \mathbb{R}^{|n|}$  as

$$\delta W = \left\{ \delta \overset{n}{\underline{u}} \right\}^T \mathbf{K} \left\{ \overset{n}{\underline{u}} \right\} - \left\{ \delta \overset{n}{\underline{u}} \right\}^T \left\{ f \right\} = 0 \qquad \forall \quad \delta \overset{n}{\underline{u}} \in \mathbb{R}^{|n|}. \tag{9}$$

The symbol n is used to denote the complete set of DoFs in the system and |n| is its cardinality, i.e., the total number of DoFs. Denoting the DoF vector as  $\left\{ \overset{n}{u} \right\} = \begin{bmatrix} N^T & M^T \\ u & N \end{bmatrix}^T$ , where N and M denote the sets of DoFs belonging to the interface that will be reduced and the others respectively (with  $\overset{N}{u} \in \mathbb{R}^{|M|}$ ), the weak form may be rewritten as:

$$\delta W = \begin{bmatrix} \delta \overset{N^T}{u} \overset{M}{\delta \overset{M}{u}} \overset{M}{i} \end{bmatrix} \begin{bmatrix} \mathbf{K}_{NN} & \mathbf{K}_{NM} \\ \mathbf{K}_{MN} & \mathbf{K}_{MM} \end{bmatrix} \begin{bmatrix} \overset{N}{u} \\ \overset{N}{u} \\ \overset{N}{u} \end{bmatrix} - \begin{bmatrix} \delta \overset{N}{u} \overset{M}{\delta \overset{M}{u}} \overset{M}{i} \end{bmatrix} \begin{bmatrix} \overset{N}{h} \\ \overset{N}{u} \\ \overset{N}{h} \end{bmatrix} = 0, \qquad \forall \quad \delta \overset{N}{u} \in \mathbb{R}^{|N|}, \, \delta \overset{M}{\overset{M}{u}} \in \mathbb{R}^{|M|}.$$

$$(10)$$

with  $\mathbf{K}_{NN} \in \mathbb{R}^{|N| \times |N|}$ ,  $\mathbf{K}_{MN} \in \mathbb{R}^{|M| \times |N|}$ ,  $\mathbf{K}_{NM} \in \mathbb{R}^{|N| \times |M|}$ ,  $\mathbf{K}_{MM} \in \mathbb{R}^{|M| \times |M|}$  denoting the corresponding partitions of  $\mathbf{K}$ ; and f, f denoting corresponding parts of f. Here, the variational form for the static problem is adopted only for ease of presentation – generalization to the dynamic case is trivial if the stationarity of the corresponding action integral (Hamilton's principle in Lagrangian mechanics) is considered. The development of the reduced order model will be identical.

For a general case with  $N_p$  patches, the continuous constraint equation is expressed as

$$\mathbf{N}\left(\underline{x}\right)\left\{u^{N}\right\} = \mathbf{G}\left(\underline{x}\right)\left\{u^{V}\right\} \qquad \underbrace{x}_{i=1} \in \bigcup_{i=1}^{N_{p}} \Gamma^{i} \equiv \Gamma, \tag{11}$$

with, 
$$\mathbf{N} : \Gamma \to \mathbb{R}^{3N_p \times |N|}$$
  
 $\mathbf{G} : \Gamma \to \mathbb{R}^{3N_p \times |V|}$ . (12)

Note that the symbol V denotes the set of virtual DoFs introduced into the model;  $\mathbf{N}(\underline{x})$  is a matrix representing the finite element shape functions; and  $\mathbf{G}(\underline{x})$  is the  $\mathbf{g}(\underline{x})$  matrix defined above but generalized to accomodate multiple virtual nodes in the same matrix quantity. The Lagrange multiplier fields for enforcing this constraint, represented henceforward as  $\lambda:\Gamma\to\mathbb{R}^{3N_p}$  (each patch gives rise to three field constraints (Eq. 3), and  $N_p$  patches gives rise to  $3N_p$  field constraints (Eq. 11)), must be discretized for the development of the ROM. The choice of discretization determines how exactly the constraints will be enforced in the final dynamic model. This may be done by representing  $\lambda(\underline{x})$  in terms of corresponding virtual node contributions or in terms of interface-nodal contributions, mathematically represented as

$$\widetilde{\lambda}(x) = \mathbf{G}(x) \begin{Bmatrix} v \\ \lambda \\ z \end{Bmatrix} \text{ (In terms of virtual nodes)} \qquad \begin{Bmatrix} v \\ \lambda \\ z \end{Bmatrix} \in \mathbb{R}^{|V|}, \tag{13a}$$

and.

$$\widehat{\lambda}(\underline{x}) = \mathbf{N}(\underline{x}) \begin{Bmatrix} N \\ \lambda \\ \lambda \end{Bmatrix} \text{(IntermsofFEnodes)} \quad \begin{Bmatrix} N \\ \lambda \\ \lambda \end{Bmatrix} \in \mathbb{R}^{|N|}.$$
(13b)

The choice of the approach depends on the purpose of the constraint application, i.e., the former, Eq. 13a, is employed when the virtual nodes need to be representative of the actual patches, while the latter, Eq. 13b, is employed when the patches need to be rigidly tied to the virtual node displacements <sup>2</sup>. This is identical to the distinction between RBE3 and RBE2 constraint elements (in ANSYS terminology) or continuum distributing and kinematic distributing elements (in ABAQUS terminology) in finite element practice [44,5,45]. Since the intention for interfacial modeling is not to constrain the interfaces, but to develop a reduced representation, the former discretization (Eq. 13a) is employed (this leads to a "non-stiffening" formulation). The contribution of this constraint to the virtual work becomes,

$$\delta W^{C} = \int_{\Gamma} \left( \mathbf{G}(\underline{x}) \{ \delta \underline{u}^{V} \} - \mathbf{N}(\underline{x}) \{ \delta \underline{u}^{N} \} \right)^{T} \underline{\lambda}(\underline{x}) d\Gamma 
= \{ \delta \underline{u}^{VT} \} \underbrace{\left[ \int_{\Gamma} \mathbf{G}(\underline{x})^{T} \mathbf{G}(\underline{x}) d\Gamma \right]}_{[^{G}\mathbf{T}_{G}]} \{ \underline{\lambda}^{V} \} - \{ \delta \underline{u}^{NT} \} \underbrace{\left[ \int_{\Gamma} \mathbf{N}(\underline{x})^{T} \mathbf{G}(\underline{x}) d\Gamma \right]}_{[^{N}\mathbf{T}_{G}]} \{ \underline{\lambda}^{V} \} 
= \{ \delta \underline{u}^{VT} \} \begin{bmatrix} {}^{G}\mathbf{T}_{G} \end{bmatrix} \{ \underline{\lambda}^{V} \} - \{ \delta \underline{u}^{NT} \} \begin{bmatrix} {}^{N}\mathbf{T}_{G} \end{bmatrix} \{ \underline{\lambda}^{V} \}.$$
(14)

<sup>&</sup>lt;sup>2</sup> A simplistic, albeit informal, interpretation is possible by visualizing the Lagrange multipliers as "constraining forces". Eq. 13a, acting primarily on the virtual node, has more control over enforcing the constraint on the virtual node rather than on the FE nodes (see weak form in Eq. 14). The converse is true for Eq. 13b, which has sufficient independent forces in order to adjust the FE nodes.

If a "stiffening" formulation is desired and Eq. 13b is used instead, the right-hand-side of Eq. 14 will become  $\left\{\delta \overset{\mathsf{V}}{\overset{\mathsf{V}}}{\overset{\mathsf{V}}{\overset{\mathsf{V}}}{\overset{\mathsf{V}}{\overset{\mathsf{V}}{\overset{\mathsf{V}}{\overset{\mathsf{V}}{\overset{\mathsf{V}}}{\overset{\mathsf{V}}{\overset{\mathsf{V}}}{\overset{\mathsf{V}}{\overset{\mathsf{V}}}{\overset{\mathsf{V}}{\overset{\mathsf{V}}}{\overset{\mathsf{V}}{\overset{\mathsf{V}}}{\overset{\mathsf{V}}{\overset{\mathsf{V}}}{\overset{\mathsf{V}}{\overset{\mathsf{V}}}}{\overset{\mathsf{V}}{\overset{\mathsf{V}}{\overset{\mathsf{V}}}{\overset{\mathsf{V}}}}{\overset{\mathsf{V}}{\overset{\mathsf{V}}}}{\overset{\mathsf{V}}{\overset{\mathsf{V}}}{\overset{\mathsf{V}}{\overset{\mathsf{V}}}{\overset{\mathsf{V}}}{\overset{\mathsf{V}}}}{\overset{\mathsf{V}}{\overset{\mathsf{V}}}{\overset{\mathsf{V}}}}{\overset{\mathsf{V}}}{\overset{\mathsf{V}}}}{\overset{\mathsf{V}}}{\overset{\mathsf{V}}}}{\overset{\mathsf{V}}}}{\overset{\mathsf{V}}}}}{\overset{\mathsf{V}}{\overset{\mathsf{V}}}}{\overset{\mathsf{V}}}}}{\overset{\mathsf{V}}}{\overset{\mathsf{V}}}}{\overset{\mathsf{V}}}}}{\overset{\mathsf{V}}}}{\overset{\mathsf{V}}{\overset{\mathsf{V}}}{\overset{\mathsf{V}}}}}}{\overset{\mathsf{V}}}}}{\overset{\mathsf{V}}}}{\overset{\mathsf{V}}}}{\overset{\mathsf{V}}}}{\overset{\mathsf{V}}}}}{\overset{\mathsf{V}}}}{\overset{\mathsf{V}}}}{\overset{\mathsf{V}}}}{\overset{\mathsf{V}}}}{\overset{\mathsf{V}}}}{\overset{\mathsf{V}}}}{\overset{\mathsf{V}}}}{\overset{\mathsf{V}}}}{\overset{\mathsf{V}}}}{\overset{\mathsf{V}}}}{\overset{\mathsf{V}}}}{\overset{\mathsf{V}}}}}{\overset{\mathsf{V}}}}{\overset{\mathsf{V}}}}{\overset{\mathsf{V}}}}{\overset{\mathsf{V}}}}{\overset{\mathsf{V}}}}{\overset{\mathsf{V}}}}{\overset{\mathsf{V}}}}{\overset{\mathsf{V}}}}{\overset{\mathsf{V}}}}{\overset{\mathsf{V}}}}{\overset{\mathsf{V}}}}{\overset{\mathsf{V}}}}{\overset{\mathsf{V}}}}{\overset{\mathsf{V}}}}{\overset{\mathsf{V}}}}{\overset{\mathsf{V}}}}{\overset{\mathsf{V}}}}{\overset{\mathsf{V}}}{\overset{\mathsf{V}}}}}{\overset{\mathsf{V}}}}{\overset{\mathsf{V}}}}{\overset{\mathsf{V}}}{\overset{\mathsf{V}}}}{\overset{\mathsf{V}}}}{\overset{\mathsf{V}}}}{\overset{\mathsf{V}}}}{\overset{\mathsf{V}}}}{\overset{\mathsf{V}}}}{\overset{\mathsf{V}}}}{\overset{\mathsf{V}}}}{\overset{\mathsf{V}}}{\overset{\mathsf{V}}}}{\overset{\mathsf{V}}}}{\overset{\mathsf{V}}}}{\overset{\mathsf{V}}}}{\overset{\mathsf{V}}}}{\overset{\mathsf{V}}}}{\overset{\mathsf{V}}}{\overset{\mathsf{V}}}}{\overset{\mathsf{V}}}}{\overset{\mathsf{V}}}}{\overset{\mathsf{V}}}}{\overset{\mathsf{V}}}}{\overset{\mathsf{V}}}{\overset{\mathsf{V}}}}{\overset{\mathsf{V}}}}{\overset{\mathsf{V}}}{\overset{\mathsf{V}}}{\overset{\mathsf{V}}}}{\overset{\mathsf{V}}}{\overset{\mathsf{V}}}}{$ 

Introducing Eq. 14 into the weak form Eq. 10 yields

$$\delta W + \delta W^{C} = \begin{bmatrix} \delta \underline{u}^{NT} \delta \underline{u}^{MT} \end{bmatrix} \begin{pmatrix} \begin{bmatrix} \mathbf{K}_{NN} & \mathbf{K}_{NM} \\ \mathbf{K}_{MN} & \mathbf{K}_{MM} \end{bmatrix} \begin{pmatrix} \underline{u}^{N} \\ \underline{u}^{M} \end{pmatrix} - \begin{bmatrix} [^{N} \mathbf{T}_{G}] \\ \mathbf{0} \end{bmatrix} \{ \underline{\lambda}^{V} \} - \begin{pmatrix} \underline{f}^{N} \\ \underline{f}^{M} \end{pmatrix} \end{pmatrix} + \{ \delta \underline{u}^{VT} \} [^{G} \mathbf{T}_{G}] \{ \underline{\lambda}^{V} \} - \underbrace{\{ \delta \underline{u}^{VT} \} \{ \underline{f}^{V} \}}_{\delta W^{V}} = 0.$$

$$(15)$$

Note that the additional term  $\delta W^V$  represents virtual work done through virtual displacements through all of the virtual DoFs directly, and is consistent as shown in Eq. 4.

The unknowns in this system are the displacement-like quantities  $\begin{Bmatrix} u \\ u \end{Bmatrix}, \begin{Bmatrix} u \\ u \end{Bmatrix}, \begin{Bmatrix} v \\ u \end{Bmatrix}$  and the virtual-node Lagrange multipliers  $\begin{Bmatrix} v \\ \lambda \end{Bmatrix}$ . In addition to this, variations of the Lagrange multiplier field gives rise to the variational

$$\delta \mathcal{W} = \int_{\Gamma} \left\{ \delta_{\tilde{\mathcal{X}}} \left( \mathbf{x} \right) \right\}^{T} \left( \mathbf{G} \left( \mathbf{x} \right) \left\{ \begin{matrix} \mathbf{v} \\ \mathbf{u} \end{matrix} \right\} - \mathbf{N} \left( \mathbf{x} \right) \left\{ \begin{matrix} \mathbf{v} \\ \mathbf{u} \end{matrix} \right\} \right) d\Gamma$$

$$= \left\{ \delta_{\tilde{\mathcal{X}}}^{V} \right\}^{T} \left( \left[ \int_{\Gamma} \mathbf{G} \left( \mathbf{x} \right)^{T} \mathbf{G} \left( \mathbf{x} \right) d\Gamma \right] \left\{ \begin{matrix} \mathbf{v} \\ \mathbf{u} \end{matrix} \right\} - \left[ \int_{\Gamma} \mathbf{G} \left( \mathbf{x} \right)^{T} \mathbf{N} \left( \mathbf{x} \right) d\Gamma \right] \left\{ \begin{matrix} \mathbf{u} \\ \mathbf{u} \end{matrix} \right\} \right)$$

$$= \left\{ \delta_{\tilde{\mathcal{X}}}^{V} \right\}^{T} \left( \left[ {}^{G} \mathbf{T}_{G} \right] \left\{ \begin{matrix} \mathbf{v} \\ \mathbf{u} \end{matrix} \right\} - \left[ {}^{N} \mathbf{T}_{G} \right]^{T} \left\{ \begin{matrix} \mathbf{u} \\ \mathbf{u} \end{matrix} \right\} \right).$$

$$(16)$$

Combining this with Eq. 15 and setting the sum to zero yields the governing equations for the static case

$$\begin{bmatrix} \mathbf{K}_{NN} & \mathbf{K}_{NM} & \mathbf{0} & -\begin{bmatrix} {}^{N}\mathbf{T}_{G} \end{bmatrix} \\ \mathbf{K}_{MN} & \mathbf{K}_{MM} & \mathbf{0} & \mathbf{0} \\ \mathbf{0} & \mathbf{0} & \mathbf{0} & \begin{bmatrix} {}^{G}\mathbf{T}_{G} \end{bmatrix} \\ -\begin{bmatrix} {}^{N}\mathbf{U}_{\alpha} \\ \mathbf{0} \\ \mathbf{0} \end{bmatrix}^{T} & \mathbf{0} & \begin{bmatrix} {}^{G}\mathbf{T}_{G} \end{bmatrix}^{T} & \mathbf{0} \end{bmatrix} \begin{bmatrix} {}^{N}\mathbf{U}_{\alpha} \\ {}^{N}\mathbf{U$$

For a "stiffening" formulation, the Lagrange-multiplier field variational becomes,

$$\delta \mathcal{W} = \left\{ \delta_{\lambda}^{V} \right\}^{T} \left( \begin{bmatrix} {}^{N}\mathbf{T}_{G} \end{bmatrix} \begin{Bmatrix} u \\ v \\ \sim \end{Bmatrix} - \begin{bmatrix} {}^{N}\mathbf{T}_{N} \end{bmatrix} \begin{Bmatrix} u \\ v \\ \sim \end{Bmatrix} \right), \tag{18}$$

which is exactly satisfied if the nodal DoFs are represented as  $\begin{Bmatrix} u \\ u \\ z \end{Bmatrix} = \begin{bmatrix} {}^{N}\mathbf{T}_{N} \end{bmatrix}^{-1} \begin{bmatrix} {}^{N}\mathbf{T}_{G} \end{bmatrix} \begin{Bmatrix} v \\ u \\ z \end{Bmatrix}$ . Treating the nodal DoFs as "slaves" and the virtual DoFs as "masters", and denoting  $\Psi = \begin{bmatrix} {}^{N}\mathbf{T}_{N} \end{bmatrix}^{-1} [{}^{N}\mathbf{T}_{G}]$ , this relationship can be used to project the original system to lead to

$$\begin{bmatrix} \mathbf{\Psi}^T \mathbf{K}_{NN} \mathbf{\Psi} & \mathbf{\Psi}^T \mathbf{K}_{NM} \\ \mathbf{K}_{MN} \mathbf{\Psi} & \mathbf{K}_{MM} \end{bmatrix} \begin{Bmatrix} \mathbf{u} \\ \mathbf$$

This is however, not the focus of the current work and will not be pursued further in this paper. Using Eq. 17 to augment the original dynamical system, represented as

$$\begin{bmatrix} \mathbf{M}_{NN} & \mathbf{M}_{NM} \\ \mathbf{M}_{MN} & \mathbf{M}_{MM} \end{bmatrix} \begin{Bmatrix} \overset{N}{u} \\ \overset{N}{u} \\ \overset{N}{u} \\ \overset{N}{u} \end{Bmatrix} + \begin{bmatrix} \mathbf{K}_{NN} & \mathbf{K}_{NM} \\ \mathbf{K}_{MN} & \mathbf{K}_{MM} \end{bmatrix} \begin{Bmatrix} \overset{N}{u} \\ \overset{N}{u} \\ \overset{N}{u} \\ \overset{N}{z} \end{Bmatrix} = \begin{Bmatrix} \overset{N}{f} \\ \overset{N}{u} \\ \overset{N}{f} \\ \overset{N}{z} \\ & & \\ &$$

with an appropriately partitioned inertia matrix  $\mathbf{M}$ , the statically constrained dynamical system is written as

$$\underbrace{\begin{bmatrix} \mathbf{M}_{NN} & \mathbf{M}_{NM} & \mathbf{0} & \mathbf{0} \\ \mathbf{M}_{MN} & \mathbf{M}_{MM} & \mathbf{0} & \mathbf{0} \\ \mathbf{0} & \mathbf{0} & \mathbf{0} & \mathbf{0} \\ \mathbf{0} & \mathbf{0} & \mathbf{0} & \mathbf{0} \end{bmatrix}}_{\mathbf{M}_{\mathbf{A}}} \underbrace{\begin{bmatrix} \overset{N}{u} \\ \overset{N}{u} \\ \overset{N}{u} \\ \overset{N}{v} \\ \overset{N}{\lambda} \end{bmatrix}}_{K_{\mathbf{A}}} + \underbrace{\begin{bmatrix} \mathbf{K}_{NN} & \mathbf{K}_{NM} & \mathbf{0} & -\begin{bmatrix} ^{N}\mathbf{T}_{G} \end{bmatrix} \\ \mathbf{K}_{MN} & \mathbf{K}_{MM} & \mathbf{0} & \mathbf{0} \\ \mathbf{0} & \mathbf{0} & \mathbf{0} & \begin{bmatrix} ^{C}\mathbf{T}_{G} \end{bmatrix} \\ \overset{N}{u} \\ \overset{N}{v} \\ \overset{N}{v} \\ \overset{N}{\lambda} \end{aligned}}_{K_{\mathbf{A}}} = \underbrace{\begin{bmatrix} \overset{N}{f} \\ \overset{N}{M} \\ \overset{N}{f} \\ \overset{N}{v} \\ \overset{N}{\lambda} \\ \overset{N}{\lambda} \end{aligned}}_{K_{\mathbf{A}}} = \underbrace{\begin{bmatrix} \overset{N}{f} \\ \overset{N}{M} \\ \overset{N}{f} \\ \overset{N}{v} \\ \overset{N}{\lambda} \\ \overset{N}{v} \end{bmatrix}}_{K_{\mathbf{A}}} = \underbrace{\begin{bmatrix} \overset{N}{f} \\ \overset{N}{M} \\ \overset{N}{f} \\ \overset{N}{v} \\ \overset{N}{\lambda} \\ \overset{N}{v} \end{bmatrix}}_{K_{\mathbf{A}}} = \underbrace{\begin{bmatrix} \overset{N}{f} \\ \overset{N}{M} \\ \overset{N}{f} \\ \overset{N}{v} \\ \overset{N}{f} \\ \overset{N}{v} \\ \overset{N}{h} \\ \overset{N}{v} \\ \overset{N}{v} \\ \overset{N}{h} \\ \overset{N}{v} \\$$

With the constraint being enforced statically, it must be observed that the inertia matrix of this system is singular (and hence only positive semi-definite). The spectral description (modal frequencies, mode shapes, etc.) of this system may easily be shown to be identical to that of the original system (for instance, LaSalle's invariance principle [35] may be invoked for static stability results <sup>3</sup> for the autonomous case on the zero-subspace, which can be used to establish relevant spectral properties). Numerically, this manifests as a singular generalized eigenvalue problem [37].

Note here that for this whole joint representation, there is no model reduction (the augmented system is larger than the original system) unless a substructuring is conducted to develop a "reduced representation" of the parts of the DoF vector other than those corresponding to the virtual node  $(\overset{V}{u})$ . Therefore whole joint models will only be considered in a substructured fashion. In this study, a HCB CMS reduction [28,19] of the system in Eq. 21 is conducted, yielding a ROM that is expressed only in terms of the virtual DoFs and generalized coordinates. After reordering the system appropriately, this reduction may be expressed as

$$\begin{pmatrix} v \\ u \\ N \\ u \\ N \\ \lambda \\ \lambda \end{pmatrix} = \underbrace{\begin{bmatrix} \mathbf{I}_{|V|} & \mathbf{0} \\ \mathbf{\Phi}_C & \mathbf{\Phi}_N \end{bmatrix}}_{\mathbf{T}_{\mathbf{HCB}}} \begin{pmatrix} v \\ u \\ N \\ u \\ N \\ \lambda \end{pmatrix}}_{\mathbf{T}_{\mathbf{HCB}}}, \qquad \overset{\eta}{u} \in \mathbb{R}^{|\eta|} \tag{22}$$

where the "fixed-interface" component modes  ${}^4\Phi_C \in \mathbb{R}^{|\eta| \times |V|}$  are calculated as the solution of the linear system

$$\begin{bmatrix} \mathbf{K}_{NN} & \mathbf{K}_{NM} & -\begin{bmatrix} ^{N}\mathbf{T}_{G} \end{bmatrix} \\ \mathbf{K}_{MN} & \mathbf{K}_{MM} & \mathbf{0} \\ -\begin{bmatrix} ^{N}\mathbf{T}_{G} \end{bmatrix}^{T} & \mathbf{0} & \mathbf{0} \end{bmatrix} \begin{bmatrix} \mathbf{\Phi}_{C} \end{bmatrix} + \begin{bmatrix} \mathbf{0} \\ \mathbf{0} \\ \begin{bmatrix} ^{C}\mathbf{T}_{G} \end{bmatrix} \end{bmatrix} = \begin{bmatrix} \mathbf{0} \end{bmatrix}, \tag{23}$$

and  $\Phi_N$  is the matrix of chosen eigenvectors for the "fixed" system as per Eq. 21, solving the eigenproblem,

$$\begin{pmatrix}
\mathbf{K}_{NN} & \mathbf{K}_{NM} & -\begin{bmatrix} {}^{N}\mathbf{T}_{G} \end{bmatrix} \\
\mathbf{K}_{MN} & \mathbf{K}_{MM} & \mathbf{0} \\
-\begin{bmatrix} {}^{N}\mathbf{T}_{G} \end{bmatrix}^{T} & \mathbf{0} & \mathbf{0}
\end{pmatrix} - \omega_{N}^{i} {}^{2} \begin{bmatrix} \mathbf{M}_{NN} & \mathbf{M}_{NM} & \mathbf{0} \\
\mathbf{M}_{MN} & \mathbf{M}_{MM} & \mathbf{0} \\
\mathbf{0} & \mathbf{0} & \mathbf{0}
\end{bmatrix} \right) \phi_{N}^{i} = 0, \tag{24}$$

with  $\phi_N^i$  denoting the *i*th column of  $\Phi_N$  (*i*th eigenvector) and  $\omega_N^{i,2}$ , its eigenvalue. Since the weight matrix of this problem is singular, this is treated as a singular generalized eigenproblem and there exist several techniques <sup>5</sup> for the solution (see [37] for an early reference). The reduced equations of motion (following the corresponding Galerkin projection) in terms of the virtual DoFs and the generalized DoFs are

$$\underbrace{\begin{bmatrix} \mathbf{T}_{\mathbf{HCB}}^{T} \mathbf{M}_{\mathbf{A}} \mathbf{T}_{\mathbf{HCB}} \end{bmatrix}}_{\mathbf{M}_{\mathbf{A}}} \left\{ \begin{array}{c} \overset{V}{\ddot{u}} \\ \overset{V}{\ddot{u}} \\ \overset{V}{\ddot{u}} \end{array} \right\} + \underbrace{\begin{bmatrix} \mathbf{T}_{\mathbf{HCB}}^{T} \mathbf{K}_{\mathbf{A}} \mathbf{T}_{\mathbf{HCB}} \end{bmatrix}}_{\mathbf{K}_{\mathbf{A}}} \left\{ \begin{array}{c} \overset{V}{u} \\ \overset{V}{\eta} \\ \overset{V}{\eta} \\ \overset{V}{u} \end{array} \right\} = \mathbf{T}_{\mathbf{HCB}}^{T} \left\{ \begin{array}{c} \overset{V}{f} \\ \overset{V}{\eta} \\ \overset{$$

 $<sup>\</sup>overline{\phantom{a}}^3$  the set  $\Re = \left\{ \left( u, \dot{u} \right) : \left\{ \dot{u}^N \right\} = 0, \left\{ \dot{u}^M \right\} = 0 \right\}$  is a superset of the set over which  $\left\{ \dot{u}^V \right\} = 0$ .

<sup>&</sup>lt;sup>4</sup> The term "fixed-interface" has nothing to do with interfacial mechanics, but is just a commonly adopted terminology in CMS

<sup>&</sup>lt;sup>5</sup> This is not a major concern as long as the eigenproblem is well-posed, since almost all modern numerical software come pre-equipped to handle this.

where the subscripts **A** are used to denote the augmented matrices in Eq. 21. The model in Eq. 25 allows for the application of interfacial forces in two ways: through the original finite element nodes f and through the virtual nodes f. Although this may

be seen as notational redundancy (having  $f_{\infty}^N$  in addition to  $f_{\infty}^V$ ), this has its own practical utilities <sup>6</sup>. Presently, however, the contact laws are completely represented through the virtual nodes alone This is a *hyper-reduction* formulation in the sense that the model is now self-contained, i.e., the nonlinear forces that must be evaluated can be fully described in the reduced coordinates in terms of reduced DoFs. The generalized force vector at the end of efeq:wjsseom represents the "carried-over" terms that could come from some initial load-step in the model such as a prestress that could have been applied in the original coordinates. In the present study, however,  $f_{gen}$  is fully set to zero.

The above development, while similar, is not identical to the RBE3 element in [44]. Where RBE3 begins with constraints applied on a node-by-node basis for a weighted least-squares representation of the nodal forces in terms of the virtual node forces and moments, the current formulation seeks a consistent representation of the lumped DoFs. The current implementation is more convenient since it is built on a traction-based formulation instead of nodal forces. Moreover, since the interpretations for the virtual DoFs, as well as the forces, are established using the underlying interfacial physics, no arbitrariness is introduced as in the weighted least-squares in RBE3. Possible extensions of the formulation include the incorporation of higher order terms (the current approach is first-order consistent), considering stresses and 3D regions for the reduction, etc.

#### 2.1.2. Patch selection

Following the development of the substructured model in Eq. 25, it becomes necessary to have a consistent way of defining the interfacial patches. Two methods are explored in the current work:

Graph Clustering: There have been several studies, mostly in the parallel programming community, that have explored the concept of constructing graphs from a finite element mesh to produce partitions based on some objective. The current study employs what is commonly referred to as a *dual graph* [59], where each element of the mesh is considered as a *graph node* and two graph nodes are connected if their corresponding elements share at least two nodes in the original finite element mesh. This graph is then clustered into the required number of components <sup>7</sup>, and the corresponding partitions of the underlying mesh are recovered by recalling the elements corresponding to each *graph node*. Fig. 2 provides a schematic illustration of this.

In the current work, the mesh partitioning binary <code>mpmetis</code> from the serial graph partitioning tools <code>Metis</code> [34,1] is employed to partition the interfacial mesh. The element areas are provided as <code>graph node</code> weights so that the produced partitions are approximately of equal size. Details of the implementation may be found in [33]. More generally, however, several techniques exist for graph clustering (see, for instance, [56]), which are very attractive for whole joint applications, but a comprehensive assessment of these is beyond the scope of the current work.

Field Objective Binning: The second method uses the contour level sets of scalar field objectives from non-linear simulations (e.g., the contact pressure field) to form patches on the interface. Suppose the field objective is denoted by  $\mathscr{P}(x)$  ( $x \in \Gamma$ ), the objective is first split into a set of discrete levels  $\mathscr{P}_{min} = \mathscr{P}_0 < \mathscr{P}_1 < \ldots << \mathscr{P}_{\mathscr{N}_{\ell m}} = \mathscr{P}_{max}$ . Elements are then labeled based on which of these intervals the field objective at its centroid evaluates to. For instance, an element with element scalar  $\mathscr{P}^e \in [\mathscr{P}_{i-1}, \mathscr{P}_i)$  is labeled "i". Following this, adjacency matrices of the *nodal graph* (with FE nodes as *graph nodes* 8) are built for each level "i" and the elements that constitute the nodes in the disconnected trees are defined as discrete patches. Off-the-shelf MATLAB routines are employed for the graph operations here.

In both of the above, contiguity (path-connectedness) of the resulting patches is enforced by requiring each patch to be a connected tree. Convexity, however, is not explicitly enforced since the influence of convexity on the developed ROM is currently unclear.

## 2.2. Re-meshing reduced order modeling

## 2.2.1. Formulation

The Re-Meshing Reduced Order Modeling (RMROM) approach is based on re-discretizing the interface using a coarser mesh for the ROM. The re-meshed representation of the interface develops a model that is of smaller size in the interface while at the same time minimizing the loss of system-level accuracy. The initial parts of the formulation are motivated similar to that of the whole joint formulation - developing a representation of the displacement vector in the reference mesh

<sup>&</sup>lt;sup>6</sup> An as-yet unpublished work of the authors [14] involve a constitutive modeling strategy that involves a fully discretized representation of the interface-normal DoFs and a reduced representation of the planar tangential DoFs.

<sup>&</sup>lt;sup>7</sup> An interesting recent work in these lines that may be of interest for some readers is [58], where the graph clustering problem has been shown to converge to the partitioning of a "continuum domain" in the variational sense as the number of nodes goes to infinity.

<sup>&</sup>lt;sup>8</sup> Contrast this with the *dual graph* employed before.

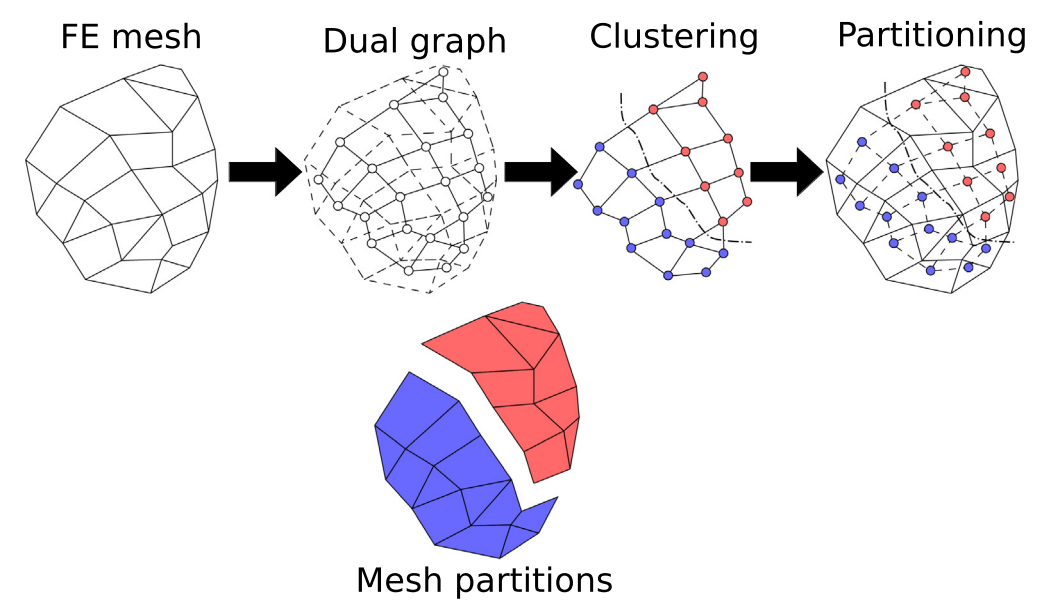


Fig. 2. Schematic illustration of the partitioning of a Finite Element (FE) mesh through the construction and clustering of its dual graph.

with respect to the reduced mesh in a point-wise fashion. The crucial difference here is that the remeshing is not intended to produce an exact model (with respect to the DoFs) - instead, a weighted/projection-based representation of the original nodal DoFs in terms of the re-meshed DoFs is sought. Distinguishing the original and new (reduced) mesh using subscripts o and r respectively (with the sets of DoFs in each represented by  $n_o$  and  $n_r$  respectively), the point-wise and weighted residue integral may be written as

$$\underbrace{\overline{N_{o}(\underline{x})\{u_{o}^{N}\}}}_{N_{o}(\underline{x})\{u_{o}^{N}\}} - \underbrace{\overline{N_{r}(\underline{x})\{u_{\underline{x}}^{N}\}}}_{\mathbb{R}^{3} \to \mathbb{R}^{3}} = \underbrace{\{\underline{r}(\underline{x})\}, \quad \mathbf{N}_{o} : \mathbb{R}^{3} \to \mathbb{R}^{3 \times |n_{o}|}, \, \mathbf{N}_{r} : \mathbb{R}^{3} \to \mathbb{R}^{3 \times |n_{r}|} \\
\underbrace{\sum_{\mathbb{R}^{3} \to \mathbb{R}^{3}}}_{\mathbb{R}^{3} \to \mathbb{R}^{3}} + \underbrace{\sum_{\mathbb{R}^{3} \to \mathbb{R}^{3}}}_{\mathbb{R}^{3} \to \mathbb{R}^{3} \to \mathbb{R}^{3} \to \mathbb{R}^{3}} = \underbrace{\{\underline{r}(\underline{x})\}, \quad \mathbf{N}_{o} : \mathbb{R}^{3} \to \mathbb{R}^{3 \times |n_{o}|}, \, \mathbf{N}_{r} : \mathbb{R}^{3} \to \mathbb{R}^{3 \times |n_{r}|} \\
\underbrace{\int_{\Gamma} \{\underline{w}(x)\}^{T} \left(\mathbf{N}_{o}(\underline{x})\{u_{o}^{N}\} - \mathbf{N}_{r}(\underline{x})\{u_{\underline{x}}^{N}\}\right) d\Gamma}_{\mathbb{R}^{3} \to \mathbb{R}^{3} \to \mathbb{R}^{3} \to \mathbb{R}^{3}}$$
(26)

Here,  $\left\{r\left(x\right)\right\}$  represents the residue function and  $\left\{w(x)\right\}$  represents the weighting function. Since the "unknowns" here are  $\left\{u_o^N\right\} \in \mathbb{R}^{|n_o|}$  (being the finer mesh), the Galerkin weight function can be expressed as interpolations of nodal quantities using the corresponding shape functions  $(N_o(x))$  in the finer mesh, without loss of generality since this spans the solution space), whereby the Galerkin form yields

$$\{u_{\underline{o}}^{N}\} = \underbrace{\left[\int_{\Gamma} \mathbf{N}_{o}(\underline{x})^{T} \mathbf{N}_{o}(\underline{x}) d\Gamma\right]^{-1} \left[\int_{\Gamma} \mathbf{N}_{o}(\underline{x})^{T} \mathbf{N}_{r}(\underline{x}) d\Gamma\right]}_{\mathbf{R}_{or} \in \mathbb{R}^{|\mathbf{n}_{o}| \times |\mathbf{n}_{r}|}} \{u_{\underline{r}}^{N}\}.$$
(27)

In Eq. 27, the first matrix ( $\left[\int_{\Gamma} \mathbf{N}_o(x)^T \mathbf{N}_o(x) d\Gamma\right]$ ) may be computed using (element) piece-wise integration on the original mesh. The calculation of the second matrix ( $\left[\int_{\Gamma} \mathbf{N}_o(x)^T \mathbf{N}_r(x) d\Gamma\right]$ ), however, involves the shape functions of the original mesh as well as those of the reduced mesh. Here, this is carried out numerically through 2D Gauss-Legendre quadrature.

In constructing the relationship matrix  $\mathbf{R}_{or}$ , element-search routines for each quadrature location in the corresponding meshes are used. In order to maintain the accuracy of the integrals (accounting for some points missed out on the boundary), both of the integrals are performed using quadrature points placed in the original mesh (and searched for in the reduced mesh). An alternative approach would be to use a nodal collocation method [21], wherein the shape functions of the reduced mesh are evaluated at the locations of the nodes in the initial mesh. This approach, however, is inconsistent with the weak form since it does not ensure the consistency of the displacement over the whole region  $\Gamma$ , and is thus not used here.

Using the same notation as in section 2.1.1, the DoFs are reordered and represented using the above transformation matrix as

Substituting this transformation into the standard second order equations of motion

$$\begin{bmatrix} \mathbf{M}_{NN} & \mathbf{M}_{NM} \\ \mathbf{M}_{MN} & \mathbf{M}_{MM} \end{bmatrix} \begin{Bmatrix} \overset{N}{\overset{u}{\overset{\sim}{u}}} \\ \overset{N}{\overset{\sim}{u}} \\ \overset{N}{\overset{u}{\overset{\sim}{u}}} \end{Bmatrix} + \begin{bmatrix} \mathbf{K}_{NN} & \mathbf{K}_{NM} \\ \mathbf{K}_{MN} & \mathbf{K}_{MM} \end{bmatrix} \begin{Bmatrix} \overset{N}{\overset{u}{\overset{\sim}{u}}} \\ \overset{N}{\overset{\sim}{u}} \\ \overset{M}{\overset{\sim}{u}} \\ \overset{N}{\overset{\sim}{u}} \end{Bmatrix} = \begin{Bmatrix} \overset{N}{\overset{N}{\overset{\sim}{u}}} \\ \overset{N}{\overset{\sim}{u}} \\ \overset{N}{\overset{N}{\overset{\sim}{u}}} \\ \overset{N}{\overset{\sim}{u}} \\ \overset{N}{\overset{N}{\overset{\sim}{u}}} \\ \overset{N}{\overset{N}} \overset{N}{\overset{N}} \\ \overset{N}{\overset{N}} \overset{N}{\overset{N}} \\ \overset{N}{\overset{N}} \\ \overset{N}{\overset{N}} \\ \overset{N}{\overset{N}} \\ \overset{N}{\overset{N}} \\ \overset{N}{\overset{N}} \\ \overset{N}{\overset{N}} \overset{N}{\overset{N}} \\ \overset{N}{\overset{N}} \overset{N}{\overset{N}} \\ \overset{N}{\overset{N}} \overset{N}{\overset{N}} \\ \overset{N}{\overset{N}} \overset{N}$$

yields the reduced form

$$\begin{bmatrix} \mathbf{R}_{or}^{\mathsf{T}} \mathbf{M}_{NN} \mathbf{R}_{or} & \mathbf{R}_{or}^{\mathsf{T}} \mathbf{M}_{NM} \\ \mathbf{M}_{MN} \mathbf{R}_{or} & \mathbf{M}_{MM} \end{bmatrix} \begin{Bmatrix} \ddot{u}_{r}^{\mathsf{N}} \\ \overset{\sim}{u} \\ \ddot{u} \\ \overset{\sim}{u} \end{Bmatrix} + \begin{bmatrix} \mathbf{R}_{or}^{\mathsf{T}} \mathbf{K}_{NN} \mathbf{R}_{or} & \mathbf{R}_{or}^{\mathsf{T}} \mathbf{K}_{NM} \\ \mathbf{K}_{MN} \mathbf{R}_{or} & \mathbf{K}_{MM} \end{bmatrix} \begin{Bmatrix} u_{r}^{\mathsf{N}} \\ \overset{\sim}{u} \\ \overset{\sim}{u} \\ \overset{\sim}{t} \end{Bmatrix} = \begin{Bmatrix} \mathbf{R}_{or}^{\mathsf{T}} \mathbf{f}_{o}^{\mathsf{N}} \\ \overset{\sim}{n} \\ \overset{\sim}{f} \\ \overset{\sim}{t} \end{Bmatrix}.$$
(30)

The forces at this level may be linear or non-linear. The term  $f_r^N = \mathbf{R}_{or}^T f_o^N$  does not yet have any direct physical interpretation, and additional relationships need to be established in order to complete the formulation. In the Zero-Thickness Element (ZTE) formulation followed here [47,26,11,8], traction constitutive laws are evaluated at quadrature locations within each element. Since the purpose of the hyper-reduction is to reduce the number of nonlinear function evaluations, it is necessary to establish a method of evaluating  $f_o^N$  using quadrature locations in the reduced mesh. The force-traction relationship in the original mesh is given by

$$\begin{cases} f_o^N \\ \\ \\ \\ \\ \end{cases} = \int_{\Gamma} \mathbf{N}_o(\mathbf{x})^T \underbrace{t(\mathbf{x})}_{\sim} d\Gamma. \tag{31}$$

The conventional way of evaluating this integral is by first evaluating the tractions t(x) at all of the quadrature locations, pre-multiplying them by the matrix  $\mathbf{N}_o(x)^T$  (evaluated at the quadrature points), and then summing them up using the quadrature weights. In a practical implementation, the last two steps may be conducted together as the product of the 2 matrices involved, simplifying the procedure. Denoting the quadrature weights and locations as  $w_i$  and  $x_i$  respectively (with  $i=1,\ldots,N_q$ , from, e.g., 2D Gauss-Legendre quadrature), the number of quadrature points as  $N_q$ , the total number of elements as  $N_e$  (yielding a total of  $N_qN_e$  quadrature points) and the element Jacobi integrals at each quadrature point organized as a diagonal matrix  $\mathbf{J}(x_i)$  (see below), this may be expressed as the sum 9

$$\left\{ f_o^N \right\} \cong \sum_{i=1}^{N_q N_e} w_i \mathbf{N}_o \left( \mathbf{x}_i \right)^T \mathbf{J} \left( \mathbf{x}_i \right) \underbrace{t}_{\sim} \left( \mathbf{x}_i \right), \tag{32}$$

with, 
$$\mathbf{J}\begin{pmatrix} \mathbf{x}_i \\ \mathbf{x}_i \end{pmatrix} = \begin{bmatrix} J^1\begin{pmatrix} \mathbf{x}_i \\ \mathbf{x}_i \\ \mathbf{y} \end{pmatrix} \\ J^2\begin{pmatrix} \mathbf{x}_i \\ \mathbf{x}_i \end{pmatrix} \\ \vdots \end{bmatrix} \otimes \begin{bmatrix} 1 & 0 & 0 \\ 0 & 1 & 0 \\ 0 & 0 & 1 \end{bmatrix} \in \mathbb{R}^{3N_e \times 3N_e}; \quad t\begin{pmatrix} \mathbf{x}_i \\ \mathbf{x}_i \end{pmatrix} = \begin{cases} t_x^1\begin{pmatrix} \mathbf{x}_i \\ \mathbf{x}_i \\ \mathbf{x}_i \end{pmatrix} \\ t_z^1\begin{pmatrix} \mathbf{x}_i \\ \mathbf{x}_i \\ \mathbf{x}_i \end{pmatrix} \\ t_x^2\begin{pmatrix} \mathbf{x}_i \\ \mathbf{x}_i \end{pmatrix} \\ \vdots \end{bmatrix} \in \mathbb{R}^{3N_e}.$$

Note that  $J^e\left(x_i\right)$  and  $t_q^e\left(x_i\right)$  denote the Jacobi determinant and traction "q" of element e evaluated at  $x_i$ , and  $\otimes$  denotes the Kronecker product. Expressing the tractions at the quadrature locations  $(t_{\sim}(x_i))$  as elements of a column matrix  $t_{\sim}^{QP}$  and the summation operation using a block-diagonal matrix

<sup>&</sup>lt;sup>9</sup> The presented formulae (Eq. 32) are just for representation. More efficient representations of quadrature is followed for the actual implementation.

$$\mathbf{W}_{or} = \begin{bmatrix} w_1 \mathbf{N}_o \begin{pmatrix} x_1 \\ x_1 \end{pmatrix}^T \mathbf{J} \begin{pmatrix} x_1 \\ x_2 \end{pmatrix} & \mathbf{0} \\ \mathbf{0} & w_2 \mathbf{N}_o \begin{pmatrix} x_2 \end{pmatrix}^T \mathbf{J} \begin{pmatrix} x_2 \\ x_2 \end{pmatrix} & \mathbf{0} \\ \mathbf{0} & \ddots \end{bmatrix}, \tag{33}$$

the discretized form of the integral in Eq. 31 becomes the matrix-vector product,

$$\left\{ f_{o}^{N} \right\} = \boldsymbol{W}_{or} \left\{ t_{r}^{QP} \right\}, \tag{34}$$

where the superscript QP and the subscript r on the vector of tractions indicate that it stores the tractions evaluated at the quadrature points of the reduced mesh. Substituting this back into the Galerkin projection in Eq. 30 yields the final form of the ROM.

$$\begin{bmatrix} \mathbf{R}_{or}^{T} \mathbf{M}_{NN} \mathbf{R}_{or} & \mathbf{R}_{or}^{T} \mathbf{M}_{NM} \\ \mathbf{M}_{MN} \mathbf{R}_{or} & \mathbf{M}_{MM} \end{bmatrix} \begin{Bmatrix} \ddot{\mathbf{u}}_{r}^{N} \\ \overset{\sim}{\mathbf{u}} \\ \ddot{\mathbf{u}} \\ \overset{\sim}{\mathbf{u}} \end{Bmatrix} + \begin{bmatrix} \mathbf{R}_{or}^{T} \mathbf{K}_{NN} \mathbf{R}_{or} & \mathbf{R}_{or}^{T} \mathbf{K}_{NM} \\ \mathbf{K}_{MN} \mathbf{R}_{or} & \mathbf{K}_{MM} \end{bmatrix} \begin{Bmatrix} \mathbf{u}_{r}^{N} \\ \overset{\sim}{\mathbf{u}} \\ \overset{\sim}{$$

Additional substructuring strategies (similar to the one presented in the end of section 2.1.1) to restrict the "M-DoFs" that are not involved in the nonlinear interface can be further employed at this point.

By saving the matrix product  $\mathbf{R}_{or}^{\mathsf{T}} \mathbf{W}_{or}$ , the formulation looks near-identical to that of a finite element model with the reduced mesh native to it. The only difference is that such a model would use integration matrices constituted by its own nodal shape functions and weights, but the present formulation first integrates the tractions on a different mesh, then projects that force vector onto the ROM basis. Therefore, the reduced mesh, in the strictest sense, must not be confused as a finite element mesh in and of itself. Integrals on the reduced mesh do not have a natural meaning in the current formulation, although displacements and tractions still retain their meanings.

#### 2.2.2. Mesh reduction

Two different approaches employed to develop reduced meshes are explored here:

Uniform Mesh Coarsening: Fundamentally, this can be done by using any coarser mesh on the surface that needs to be reduced. In the present work, the reference mesh is used as a starting point. Adjacent elements are combined to coarsen the mesh based on the required level of coarsening. All of the nodes of the reduced mesh coincide with nodes of the original mesh. This simple algorithm can be carried out for cases where the reference surface meshes consists only of quadrilateral elements (such as enforced in the numerical studies for the present work). When this is not so, more general 2D meshing techniques may be followed for generating a coarse mesh.

Field Objective Method: The second reduction method aims for better consideration of the salient physics for the reduction by considering field objectives representative of the interfacial physics. Contours of the chosen field objective are used to place *new* nodes on the interface. The number of contour lines and the density used to place nodes on each contour line is determined through an iterative process, depending on the target number of elements for the reduced mesh. It is ensured that the produced elements are of nearly equivalent areas (biased meshes are prevented). The newly placed nodes are re-meshed using triangular and quadrilateral elements. To ensure that elements with a *fair* quality are generated, an upper limit of 0.75 is set for the equi-angular skewness of the elements (see [5] for more details on the metric). section C provides a step-by-step description of remeshing for the bolted joint interface considered in section 3.2.

## 2.3. Metrics for error analysis

Quantitative assessment of the solutions from the developed ROMs is conducted by comparing it with the reference finite element solution for this study in the spirit of a posteriori error analysis. A priori approaches will not be explored here since this can be highly non-trivial for nonlinear hysteretic systems and is beyond the scope of the current work.

Consider a solution in the original finite element space  $\overset{ref}{u} \in \mathscr{H}^{ref}(\Omega)$  (taken as "reference" solution), and its approximation in the reduced-space  $\overset{red}{u} \in \mathscr{H}^{red}(\Omega)$  (representing the reduced order model solution). Here,  $\Omega \subset \mathbb{R}^3$  denotes the problem domain (body of the structure of interest), and  $\mathscr{H}^{ref}(\Omega)$  and  $\mathscr{H}^{red}(\Omega)$  denote appropriate function spaces with domain  $\Omega$  (with  $\mathscr{H}^{red}(\Omega) \subseteq \mathscr{H}^{ref}(\Omega)$ ). Let the discretized representations of the two be denoted as  $\overset{d,ref}{u} \in \mathbb{R}^{|d,ref|}$  and  $\overset{d,red}{u} \in \mathbb{R}^{|d,red|}$  respectively, related through the matrix  $\mathbf{T}_{rom} \in \mathbb{R}^{|d,ref| \times |d,red|}$  by the approximation,

$$\overset{d,ref}{u} \approx \widehat{u} \sim d, ref = \mathbf{T}_{rom} \overset{d,red}{u}.$$
 (36)

Here,  $\{d,ref\}$  and  $\{d,red\}$  are used to denote the sets of discretized DoFs in the reference and reduced representations respectively, and the term  $\widehat{u} \sim d,ref$  denotes the approximation from the ROM. The discretization in  $\mathscr{H}^{ref}(\Omega)$  is taken to be expressed using appropriate shape functions  $\mathbf{n}:\Omega\to\mathbb{R}^{|ref|\times|d,ref|}$  (with ref denoting the set of DoFs in the reference-space) through

$$\overset{ref}{u}(x) = \mathbf{n}(x) \overset{d,ref}{u}.$$
 (37)

Using the ROM approximation (Eq. 36), the effective discretization of the ROM is

$$\overset{red}{\overset{u}{\overset{\sim}{\sim}}} \left( \overset{\times}{\overset{\sim}{\sim}} \right) = \mathbf{n} \left( \overset{\sim}{\overset{\sim}{\sim}} \right) \mathbf{T}_{rom} \overset{d,red}{\overset{\sim}{\sim}} . \tag{38}$$

The  $L^2$ -norm in  $\mathscr{K}^{ref}(\Omega)$  of the deviation between  $\overset{ref}{\overset{}{u}}$  and  $\overset{red}{\overset{}{u}}$  scaled by the density of the structure  $\overset{10}{\overset{}{}}$  (denoted  $\rho\left(\overset{}{\overset{}{x}}\right)$ ) will be employed as the a posteriori error metric. Numerically, denoting the deviation as  $\overset{}{\overset{}{u}} = \overset{red}{\overset{}{\overset{}{u}}} - \overset{ref}{\overset{}{\overset{}{u}}}$  (and its discretized counterpart as  $\overset{}{\overset{}{u}} = \overset{d_red}{\overset{}{\overset{}{u}}} - \overset{d_ref}{\overset{}{\overset{}{u}}}$ ), this can be shown to be

$$||\tilde{\underline{u}}||_{L^{2}(\Omega)}^{2} = \{\tilde{\underline{u}}^{d}\}^{T} \underbrace{\left[\int_{\Omega} \mathbf{n}(\underline{x})^{T} \rho(\underline{x}) \mathbf{n}(\underline{x}) d\Omega\right]}_{\mathbf{M}^{d,ref}} \{\tilde{\underline{u}}^{d}\}$$

$$\implies err(\underline{\underline{u}}^{d,red}) = \sqrt{\{\tilde{\underline{u}}^{d}\}^{T} \mathbf{M}^{d,ref} \{\tilde{\underline{u}}^{d}\}},$$
(39)

where  $\mathbf{M}^{d,ref} \in \mathbb{R}^{|d,ref| \times |d,ref|}$  is the discretized reference mass matrix. Denoting the reduced order mass matrix  $\mathbf{M}^{d,red} \in \mathbb{R}^{|d,red| \times |d,red|}$  (numerically written as  $\left[\mathbf{T}^T_{rom}\mathbf{M}^{d,red}\mathbf{T}_{rom}\right]$  through the Galerkin projection), this may be simplified further (assuming symmetric mass matrix) to

$$err\begin{pmatrix} d,red \\ u \\ \tilde{u} \end{pmatrix} = \sqrt{\begin{Bmatrix} d,ref \\ u \\ \tilde{u} \end{Bmatrix}}^T \mathbf{M}^{d,ref} \begin{Bmatrix} d,ref \\ u \\ \tilde{u} \end{Bmatrix} + \begin{Bmatrix} d,red \\ u \\ \tilde{u} \end{Bmatrix}^T \mathbf{M}^{d,red} \begin{Bmatrix} d,red \\ u \\ \tilde{u} \end{Bmatrix} - 2\begin{Bmatrix} \mathbf{T}_{rom} \overset{d,red}{u} \\ \tilde{u} \end{Bmatrix}^T \begin{bmatrix} \mathbf{M}^{d,ref} \end{bmatrix} \begin{Bmatrix} d,ref \\ u \\ \tilde{u} \end{Bmatrix}} = \sqrt{||\overset{d,ref}{u}||^2_{d,ref} + ||\overset{d,red}{u}||^2_{d,ref} - 2\mathbf{T}_{rom} \overset{d,red}{u}, \overset{d,ref}{u}, \overset{d,ref}{u}}{u}, \frac{d,ref}{u}}$$

$$(40)$$

with  $||\cdot||_{d,ref}$  and  $||\cdot||_{d,red}$  denoting mass-weighted 2-norms in the discretized reference and reduced spaces respectively and  $\cdot$ ,  $\cdot_{d,ref}$  denoting the mass-weighted inner product in the discretized reference space. The relative error norm is defined by

$$relerr\begin{pmatrix} d, red \\ u \\ \sim \end{pmatrix} = \frac{err\begin{pmatrix} d, red \\ u \\ \sim \end{pmatrix}}{\left\| \begin{array}{c} d, ref \\ u \\ \parallel d, ref \end{array} \right\|}.$$
(41)

Since the primary focus of the current effort is on dynamics, deviations in linear/non-linear mode shapes is of interest. In these cases, the deviation in the discretized mode-shape from the ROM,  $\phi \in \mathbb{R}^{|d,red|}$  with respect to the reference  $\phi \in \mathbb{R}^{|d,ref|}$ ,  $\phi \in \mathbb{R}^{|d,ref|}$ ,  $\phi \in \mathbb{R}^{|d,ref|}$ ,

assuming both are mass-normalized (||  $\stackrel{d,ref}{\phi}$  || $_{d,ref}$  = ||  $\stackrel{d,red}{\phi}$  || $_{d,red}$  = 1) becomes

$$dev\begin{pmatrix} d, red & d, ref \\ \phi & , & \phi \\ & & \sim \end{pmatrix} = \sqrt{2\left(1 - \mathbf{T}_{rom} & \phi & d, ref \\ \phi & , & \phi & d, ref \\ & & \sim \end{pmatrix}}.$$
 (42)

Recognizing the similarity with the modal assurance criterion [3] (MAC; specifically the Weighted MAC (WMAC) with the mass matrix as the weighting), a MAC-Deviation, or MACDEV criterion will be used throughout the paper for comparing mode shapes. The MACDEV is defined as,

$$\textit{MACDEV} \begin{pmatrix} \textit{d,red} & \textit{d,ref} \\ \phi & , & \phi \\ \sim & \sim \end{pmatrix} = 1 - \left\langle \mathbf{T}_{rom} \stackrel{\textit{d,red}}{\phi} & \textit{d,ref} \\ \sim & \sim \\ \sim & \sim \\ \sim & \sim \\ \rangle \textit{d,ref} \, .$$
 (43)

 $<sup>^{10}</sup>$  This is done so that the mass matrix can directly be used, see Eq. 39

#### 3. Numerical illustrations

In what follows, the application of the developed reduced order modeling strategies is illustrated numerically. The first case study is focused on the linear behavior of the reduced order models applied to reducing the representation of a surface, while providing appropriate comparisons with corresponding procedures implemented in ABAQUS; and the second case study focuses on the behavior of the reduced order model for a non-linear finite element model of a bolted joint, see Fig. 3.

## 3.1. Solid beam with holes – A linear case study

The first case study is conducted on the reduced order modeling of a linear elastic solid beam with three holes, as shown in Fig. 4. The goal of this example is to demonstrate the fact that the hyper-reduction is consistent with the modal properties of the system (in the absence of any non-linearities). The geometry  $^{11}$  is chosen so as to provide a sufficiently complicated geometry while at the same time being simple enough to be intuitive. The density, Young's modulus, and Poisson's ratio are set as 7800 kg m $^{-3}$ , 200 GPa, and 0.3 respectively. The natural frequencies of the first five elastic modes in the fully-free boundary configuration are tabulated in Table 1. A reduced representation of the  $120 \times 25.4$  mm surface (with the three holes) is pursued for the investigations.

A meshed model is generated in ABAQUS to serve as the reference (see Fig. 5). Both the ROM strategies will be pursued in order to make key observations about their behavior in relation to established procedures. The WJROMs will be compared with models constructed with distributed coupling elements in ABAQUS; and the RMROMs will be compared with models uniformly meshed in a coarse fashion. Linear C3D8R elements [45] are used everywhere unless otherwise specified.

Fig. 6 depicts the first five elastic mode-shapes of this structure in the fully-free boundary configuration (see Table 1 for frequencies). As can be observed, the top surface (with the holes) undergoes significant strains in all of these modes, necessitating the developed representations to be sufficiently consistent in order to yield to acceptable ROMs.

# 3.1.1. Whole joint reduced order modeling

The first aspect that must be considered for a numerical implementation of the WJROM is conditioning. The stiffness matrix of the augmented system (Eq. 21) has the terms corresponding to the constraint enforcement. In practice, it is found that the conditioning of this matrix is critical for a numerically well-behaved reduced order model. In the current paper, the constraints are scaled by a conditioning coefficient  $\xi$ , leading to an augmented stiffness matrix  $\mathbf{K}_A^c$  parameterized by  $\xi$  through

$$\mathbf{K}_{A}^{c}(\xi) = \begin{bmatrix} \mathbf{K}_{NN} & \mathbf{K}_{NM} & \mathbf{0} & -\xi \begin{bmatrix} {}^{N}\mathbf{T}_{G} \end{bmatrix} \\ \mathbf{K}_{MN} & \mathbf{K}_{MM} & \mathbf{0} & \mathbf{0} \\ \mathbf{0} & \mathbf{0} & \mathbf{0} & \xi \begin{bmatrix} {}^{C}\mathbf{T}_{G} \end{bmatrix} \\ -\xi \begin{bmatrix} {}^{N}\mathbf{T}_{G} \end{bmatrix} & \mathbf{0} & \xi \begin{bmatrix} {}^{C}\mathbf{T}_{G} \end{bmatrix} & \mathbf{0} \end{bmatrix}.$$
(44)

For each case, a three-point quadratic search is conducted (in  $\log_{10}$ -scale) to determine the critical  $\xi^*$  that minimizes the condition number of  $\mathbf{K}_A^c$ . For all the studies in this paper, three values of  $\xi$ ,  $\xi_1 = 10^0$ ,  $\xi_2 = 10^{15}$  and  $\xi_3 = 10^{30}$  are used as initialization for this search. Denoting the corresponding condition numbers as  $\kappa_1$ ,  $\kappa_2$ , and  $\kappa_3$  respectively, a local quadratic fit is established (in log-scale) as follows:

such that,  $\log_{10}(\kappa) \cong a_0 + a_1 \log_{10}(\xi) + a_2 \log_{10}(\xi)^2$ .

From this, the optimal coefficient is estimated as  $\xi^* = 10^{-a_1/(2a_2)}$ . Although one could potentially iterate on this, conducting just a single estimate was found to be sufficient for all the studies here.

For a whole-joint model with five patches, as shown in Fig. 7a. The element sets have been chosen manually and the virtual nodes have been placed at the centroids of each patch. Fig. 7b depicts the trend of the conditioning number of  $\mathbf{K}_A^c$  for different  $\xi$  values, along with the initialization and critical value. As can be seen, while the conditioning of the critically conditioned system is only slightly more than that of the reference unconstrained system, a poor choice of this could lead to highly ill-conditioned systems.

Following this, a HCB reduced model with 50 fixed-interface component modes retained is generated (WJROM). For comparison an ABAQUS model is prepared with identical patches and virtual nodes located at the same points, coupled using the ABAQUS Distributed Coupling elements with "uniform" weighting (ABAQUS DC). Also, the ABAQUS model is substructured using 50 fixed-interface modes, like the WJROM.

Table 2 tabulates the natural frequencies of the first five modes along with percentage deviations from the reference unconstrained system. For the mode-shapes, the MAC-Deviation (MACDEV, defined in Eq. 43) is used to quantify deviations.

<sup>11</sup> It may be noted that the geometry is similar to the Brake-Reuß Beam interface (see section 3.2).

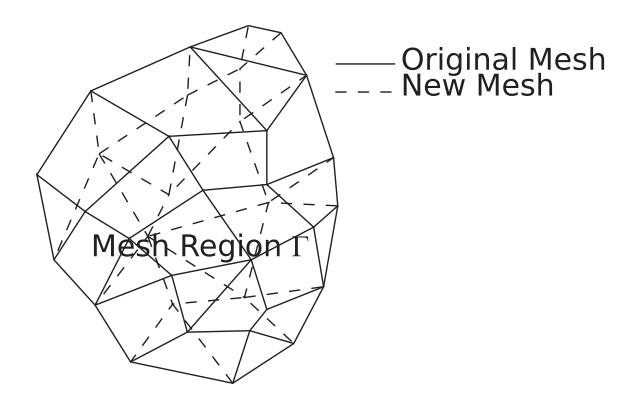


Fig. 3. Illustration of a re-meshed region.

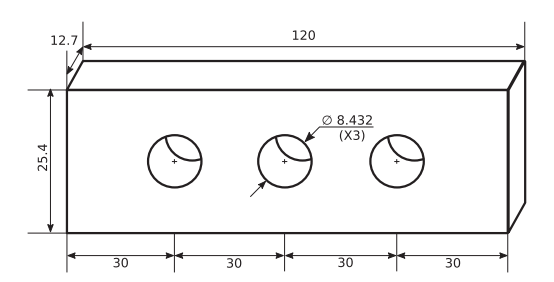


Fig. 4. Dimensional schematic of the solid beam benchmark (dimensions in mm, not to scale).

**Table 1** Elastic modal frequencies.

Mode	Frequency (Hz)		
1	4014.21		
2	7903.23		
3	8592.07		
4	10,520.13		
5	17,398.38		

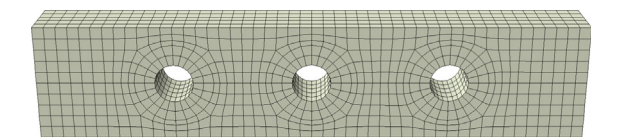
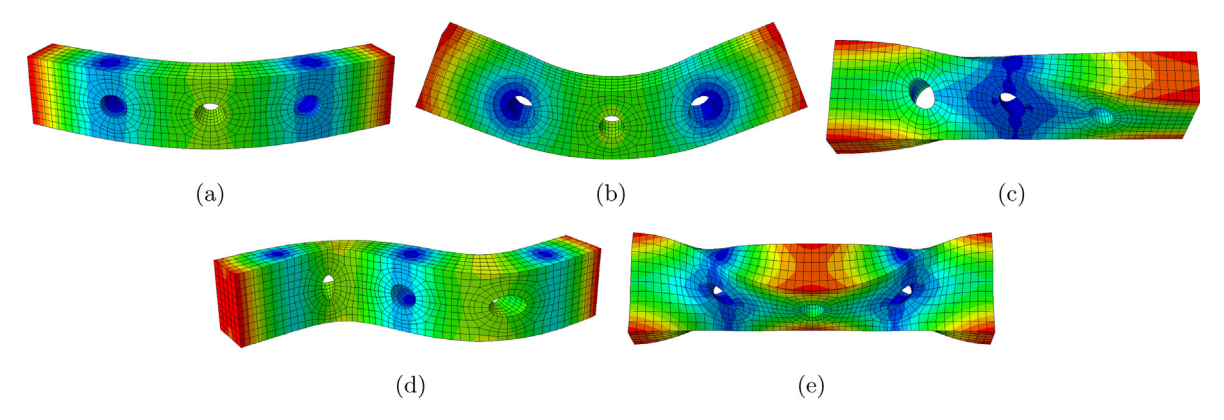


Fig. 5. Reference meshed model for solid beam benchmark.

Here,  $\mathbf{T}_{rom}$  denotes the appropriate parts of the recovery matrix for the HCB reduced model ( $\mathbf{T}_{HCB}$  in Eq. 22) in the case of the WJROM and appropriate rows of the substructure recovery matrix in the case of the ABAQUS DC.

The deviations (both frequency and mode-shape) of the current WJROM and the ABAQUS DC approaches are approximately identical for the considered example, as shown in Table 2. In order to complete the comparison, Metis (see "Graph Clustering" in section 2.1.2) is used to generate different numbers of patches (ranging from 3 to 90) and the convergence of the current WJROM and ABAQUS DC are compared in terms of the frequency and MAC deviations. Fig. 8 depicts some of these models along with the coupling nodes.

Fig. 9 depicts the frequency error and MAC-deviation as a function of the number of patches selected for the reduction,  $N_p$ . It can be observed that the trends of both of the ROMs seem to be approximately identical. Note here that the present strategy has a fundamentally different derivation, motivated by representation of surface tractions, in comparison with the coupling elements in ABAQUS.



**Fig. 6.** Mode shapes considered for study: (a–e) denote the first five elastic mode shapes. Colors denoted mass-normalized absolute displacement amplitudes. (For interpretation of the references to colour in this figure legend, the reader is referred to the web version of this article.)

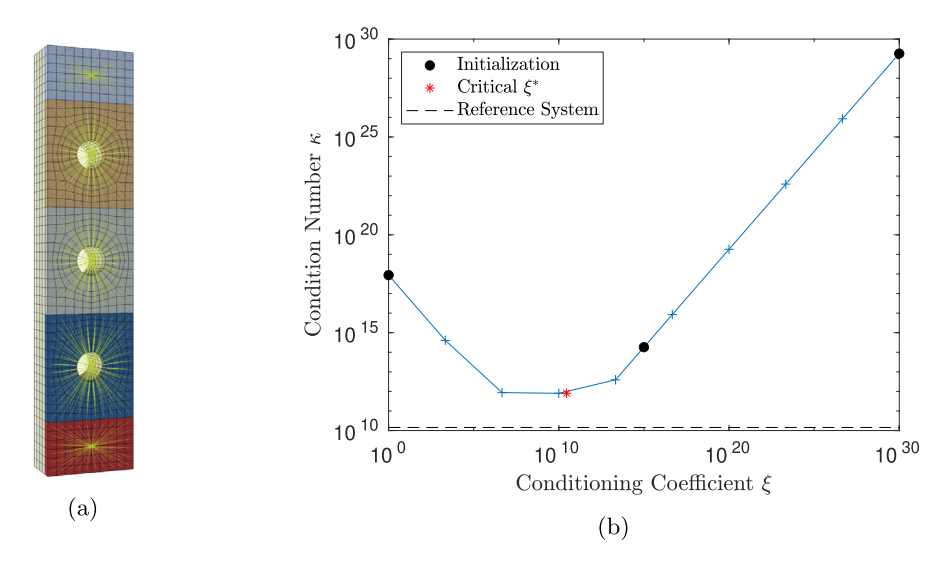


**Fig. 7.** (a) The five-patch configuration for the solid beam benchmark; and (b) The condition number  $\kappa$  as a function of coefficient  $\xi$ . Also plotted (in (b)) is the conditioning of the unconstrained (reference) system, initialization, and the estimated critical point.

**Table 2** First five elastic mode frequencies of the reference  $(\omega_{ref})$  and reduced models  $(\omega_n)$ ; percentage frequency error; and MAC-Deviations. The current approach is denoted WJROM and the ABAQUS Distributing Coupling elements approach is denoted ABAQUS DC.

	Reference		WJROM		ABAQUS DC		
Mode	$\omega_{ref}$ (Hz)	$\omega_n$ (Hz)	$\Delta\omega_n/\omega_{ref}$ (%)	MACDEV	$\omega_n$ (Hz)	$\Delta\omega_n/\omega_{ref}$ (%)	MACDEV
1	4014.21	4016.94	0.07	$6.04 \times 10^{-7}$	4017.15	0.07	$6.11 \times 10^{-7}$
2	7903.23	7983.20	1.01	$1.04\times10^{-4}$	7982.56	1.00	$1.01\times10^{-4}$
3	8592.07	8633.08	0.48	$1.73\times10^{-5}$	8633.15	0.48	$1.72\times10^{-5}$
4	10520.13	10573.00	0.50	$2.80\times10^{-5}$	10573.21	0.50	$2.80\times10^{-5}$
5	17398.38	17881.04	2.77	$9.87\times10^{-4}$	17880.93	2.77	$9.77\times10^{-4}$

## 3.1.2. Remeshing reduced order modeling

In order to investigate the RMROM approach, reduced meshes are constructed for the solid beam using the uniform coarsening approach (see section 2.2.2). The interface is composed using linear quadrilateral elements. The objective here is to compare the presented reduced order modeling strategy (RMROM) with models of the beam that are coarsely meshed uniformly. Fig. 10 depicts the different meshes used for finite element analysis. Note that the remeshing procedure outlined above only generates surface meshes. These are repeated along the thickness to form solid C3D8R elements [45].

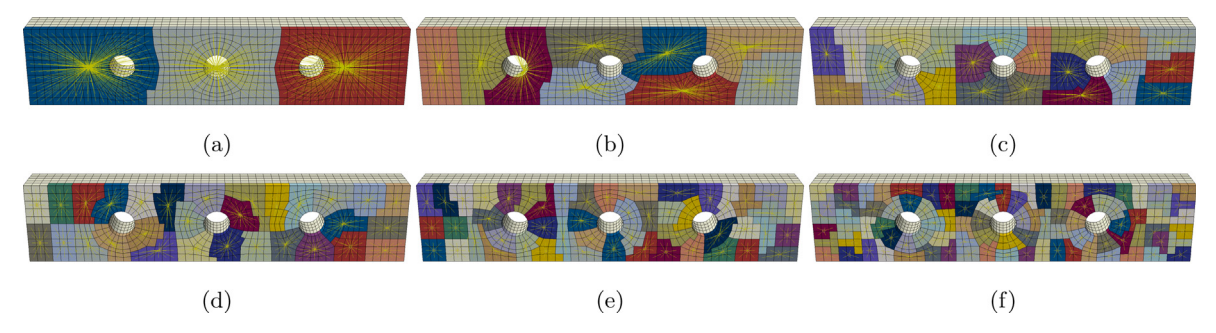
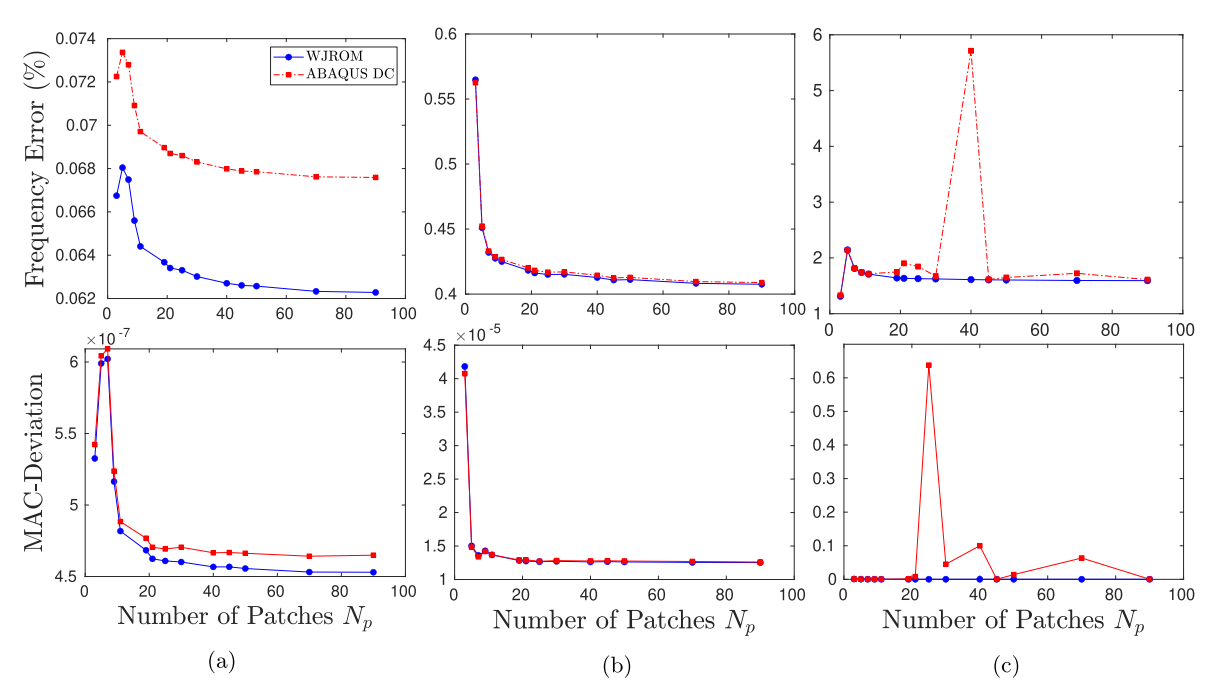


Fig. 8. Whole Joint Models with different numbers of patches generated using metis: (a-f) correspond to models with 3, 9, 21, 30, 50, and 90 patches respectively.



 $\textbf{Fig. 9.} \ \ \textbf{Whole-Joint convergence of (a) Mode 1; (b) Mode 3; and (c) Mode 5.}$ 

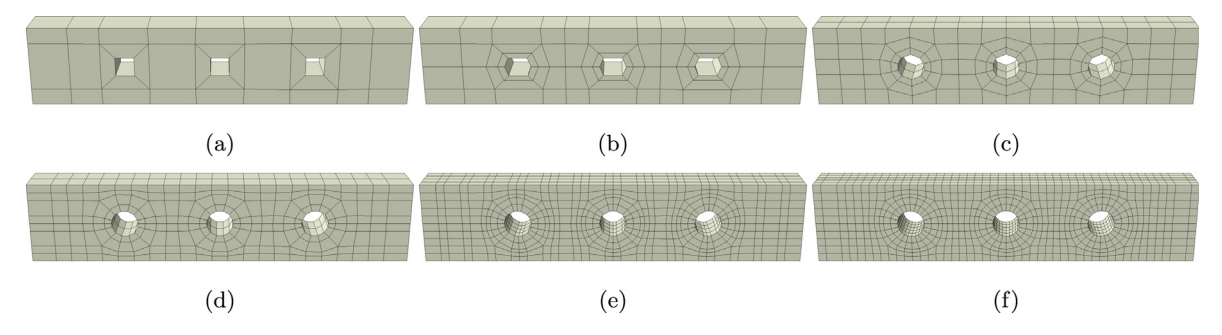


Fig. 10. ABAQUS models of the solid beam meshed with coarser elements. The number of elements along the thickness is fixed by requiring the element aspect ratios to be approximately constant. (a–f) correspond to 36, 74, 122, 232, 448, and 568 elements on the top surface respectively.

This study is mainly conducted in order to understand how much improvement the developed remeshing approach offers in comparison to just using a coarser mesh. Relative errors in natural frequencies are taken as the sole criterion of analysis since comparing the mode-shapes of the coarsely meshed models with the reference would involve 3D interpolation, and

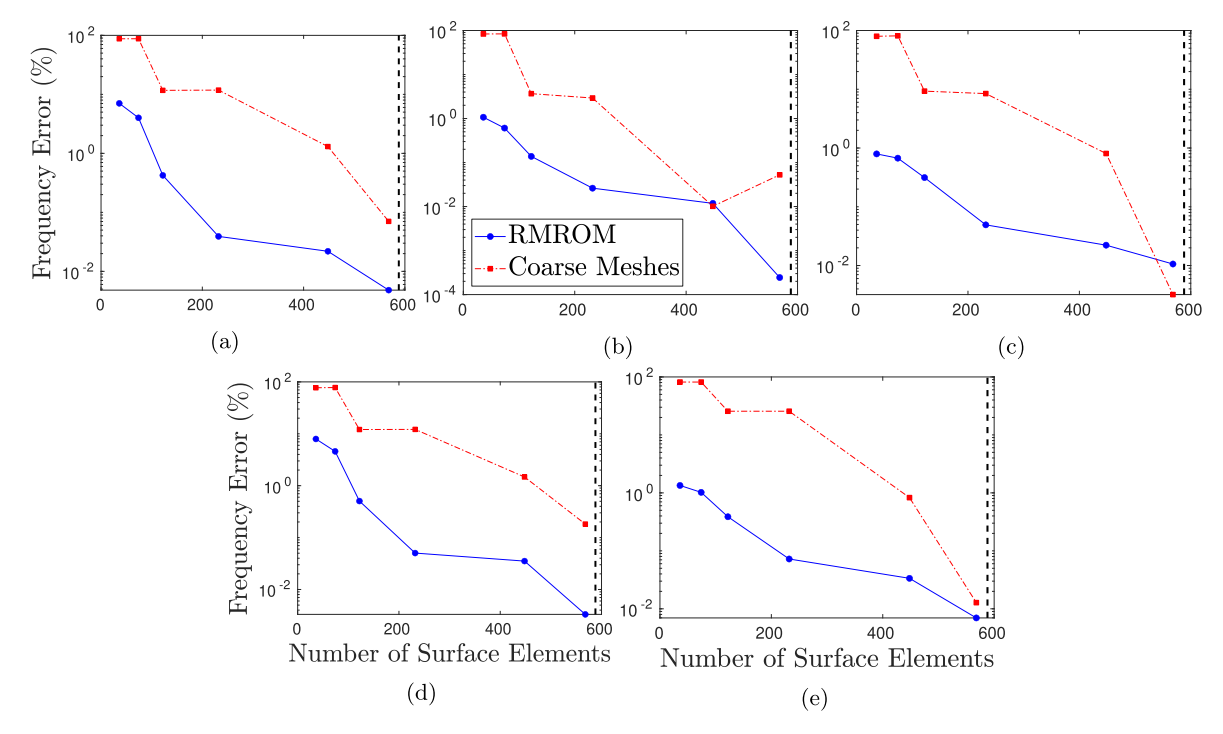


Fig. 11. Convergence of modal frequencies – comparison of the remeshing approach (RMROM) with finite element models with coarser meshes: (a–e) present results for elastic modes 1–5 respectively. The dashed vertical line indicates the number of surface elements in the original mesh.

that is not carried out presently. <sup>12</sup> Fig. 11 depicts the convergence behavior of the first five natural frequencies (as functions of the number of elements on the surface). It can be observed that RMROM has a characteristically different behavior in comparison to mesh coarsening. For smaller number of elements the RMROM performs much better, but larger models exhibit lower improvements, as expected. It is worth recalling here that while the RMROM is developed to converge to the finite element reference, the finite element meshes are developed to converge to the continuum limit.

Another aspect that is of great relevance for modeling jointed systems is the case where only a substructured model of the reference is available. This is often the case for non-linear analysis of large-scale jointed systems. Therefore, the convergence of the RMROMs are assessed between cases where the whole model and a HCB reduced model with 50 fixed-interface component modes are employed for the reduction. Fig. 12 shows the frequency convergence trends in these cases. It is evident that although the ROMs do exhibit convergence in both cases, there seems to be a hard lower bound for the case with the HCB reduced reference. This is thought to be a relic of the HCB reduction itself (which is based on a truncated modal representation of the fixed-interface dynamical system), which restricts the accuracy of the solution with respect to the reference.

In conclusion, the most important feature of the proposed RMROM approach is that the imposed mesh on the surface need not be the same type as the underlying mesh – any popular 2D mesh may be employed on the surface independent of the 3D mesh the body is discretized with. This is particularly useful for substructured analyses of jointed systems wherein only the joint nodes are readily available and the rest are represented using component modes. Although using the RMROMs as secondary reductions on substructured models is not ideal, as Fig. 12 demonstrates, the method is still applicable if one is cognizant of the convergence behavior. The next case study (section 3.2) illustrates one such scenario for a bolted joint where a substructured model is used as reference.

# 3.2. Modeling and analysis of bolted structures - a nonlinear case study

The current section applies the developed ROM approaches to the Brake-Reuß Beam (BRB) benchmark [15,13,6], a three-bolted lap-joint structure. A substructured finite element model with 20 fixed interface component modes and all of the interfacial nodes retained is used as the reference model, and all ROMs are developed from it. The reference finite element model is constructed using linear C3D8R elements in ABAQUS [45]. Rayleigh Quotient-based Non-linear Modal Analysis [7] (RQNMA), a recently developed quasi-static non-linear modal analysis procedure, is used to characterize the amplitude-

<sup>&</sup>lt;sup>12</sup> The mode-shapes and frequencies are, however, not independent quantities but demonstrating convergence in terms of just the frequency is considered sufficient here.

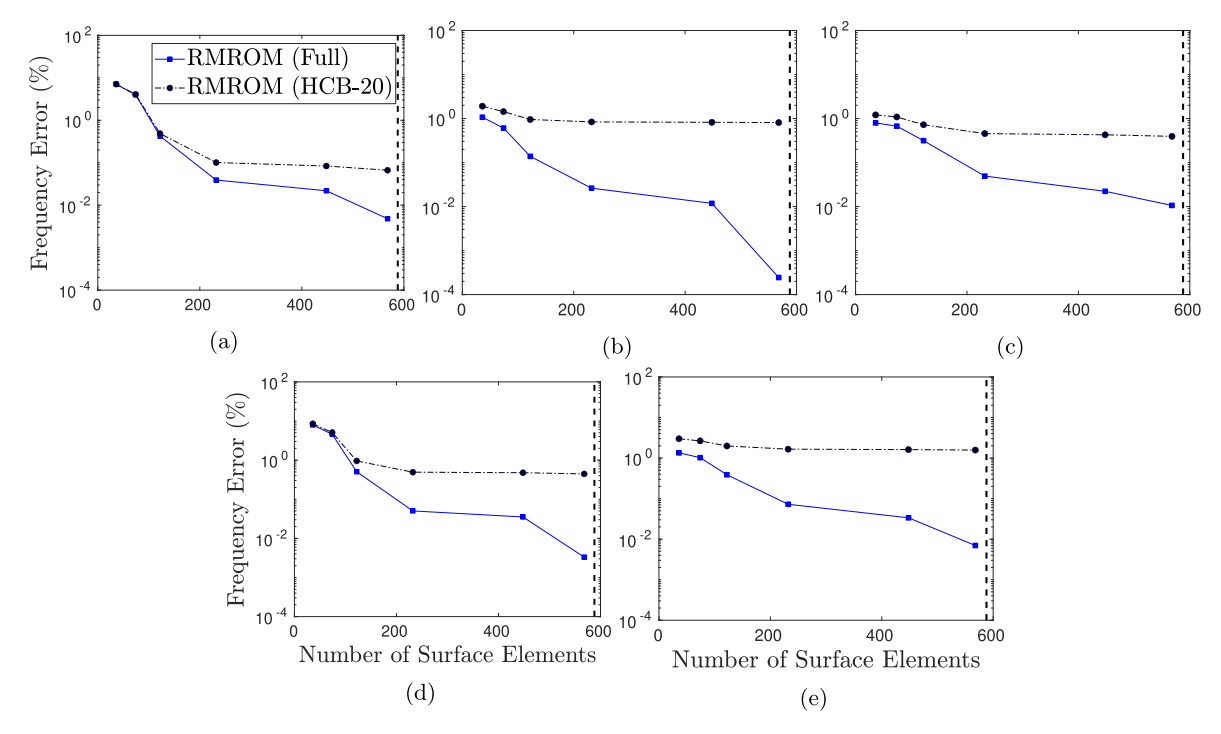


Fig. 12. Convergence of modal frequencies - comparison of the remeshing applied to reference models with and without HCB Reduction: (a–f) present results for elastic modes 1–5 respectively. The dashed vertical line indicates the number of surface elements in the original mesh.

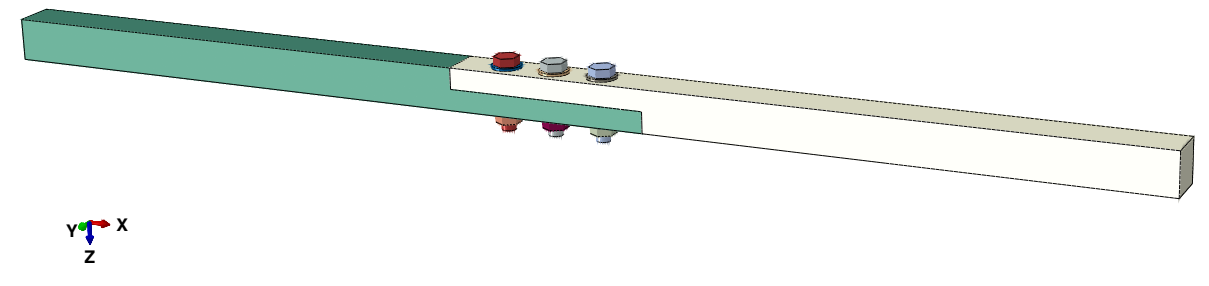


Fig. 13. CAD model of the Brake-Reuß Beam.

dependent modal characteristics of the systems. The characterizations from the ROMs are compared with the reference simulations and deviations are presented as a comparative metric for assessment.

## 3.2.1. Model description

The BRB assembly, depicted in Fig. 13, consists of two "half-beams" connected through a three-bolted lap-joint. The total length of the beam is about 720 mm (28.375 in) and the cross-section of the beams is a 25.4 mm  $\times$  25.4 mm (1 in  $\times$  1 in) square. Three sets of 5/16-inch bolts, nuts and washers are used for the assembly, which has a 120 mm  $\times$  25.4 mm contacting interface (the interface geometry is identical to the solid beam model considered in section 3.1). The exact dimensions and drawings of the structure may be found in [13,6]. Each bolt is statically pre-stressed to a load of 11,580 N at static equilibrium, and is considered present throughout the analyses. The density, Young's modulus and Posson's ratio are 7857.8 kg m<sup>-3</sup>, 192.85 GPa, and 0.29 respectively.<sup>13</sup>

#### 3.2.2. Interface constitutive modeling

In order to maintain consistency, a planar elastic dry friction model and a unilateral linear penalty stiffness (see [60,24,61]) are used as the constitutive models for the interface in the tangential and normal directions respectively. The

<sup>&</sup>lt;sup>13</sup> Numbers estimated from a physical assembly used in [8].

current section provides implementational details of the same in the context of the reference ZTE as well as the ROM implementations.

#### 3.2.3. Traction-constitutive model for the zero-thickness elements

For the ZTEs (both in the reference and remeshed ROMs), the implementation used is identical to earlier works ([26,47,8]). For the contact constitutive model, the formulation is identical to the one in [2], but these are employed in the traction-level and integrated over the elements by evaluating them at quadrature locations followed by a weighted summation. In all simulations, 25 2D Gauss–Legendre points are used per element. The traction  $(t_n)$  displacement  $(u_n)$  relationship in the normal direction is

$$t_n(u_n) = \begin{cases} k_n u_n & u_n > 0 \quad (contact) \\ 0 & u_n < 0 \quad (separated) \end{cases}, \tag{46}$$

where  $k_n$  is the normal contact stiffness. The coordinate systems are defined such that when the normal (relative) displacement is positive, the interfaces are in contact and when it is negative, the interfaces are separated.

In the tangential directions, the traction  $(t_x^x, t_y^y)$  displacement  $(u_x^x, u_y^y)$  relationship is given by

$$t_{t}^{q}(u_{t}^{x}, u_{t}^{y}) = \begin{cases} 0 & t_{n} = 0 & (separation) \\ \frac{t_{sp}^{q}}{k_{t}^{q}(u_{t}^{q} - u_{t0}^{q}) + t_{t0}^{q}} & \sqrt{t_{sp}^{x}^{2} + t_{sp}^{y}^{2}} < \mu t_{n} & (stick) \\ \mu t_{n} \frac{t_{sp}^{q}}{\sqrt{t_{sp}^{x}^{2} + t_{sp}^{y}^{2}}} & otherwise & (slip) \end{cases}$$

$$(47)$$

Here, the superscripts q denote the tangential directions x and y, and terms with a subscript 0 denote the terms from the previous point on the hysteretic curve. Tractions  $t_{sp}^x$  and  $t_{sp}^y$  denote the "stick-prediction" tractions, i.e., the predicted tractions assuming the point is in the stuck condition (used to check the condition for slippage). As can be seen, the model is parameterized by a coefficient of friction  $\mu$  and two tangential stiffnesses  $k_t^x$ ,  $k_t^y$ . Isotropic friction is assumed throughout, and therefore  $k_t^x = k_t^y$  throughout the interface. This model, when implemented on the actual finite element mesh, is taken as the reference for comparing all of the ROMs.

## 3.2.4. Force-constitutive model for the whole-joint patches

Most whole joint implementations use a force–displacement constitutive law instead of the traction form discussed above [57]. However, since the current study seeks to maintain consistency across interfacial representations, phenomenological relationships are needed between the virtual node DoFs (u, consisting of translations and rotations) and virtual node

forcing terms ( $\int_{-\infty}^{v}$ , consisting of forces and moments), which are equivalent to the traction-constitutive planar elastic dry friction model described above. Before beginning the development, it is first assumed, for simplicity, that the "patch" is parallel to the coordinate xy-plane, and the virtual node lies at the centroid of the plane. There is no loss of generality here for flat patches since appropriate coordinate transformations may be employed to suit this description.

Recalling Eq. 1, the displacements at a point  $x \in \Gamma^{\nu}$  is written in terms of the virtual node DoFs as

For a linear traction-displacement constitutive law (the "stuck" condition of the elastic dry friction model), the corresponding tractions may be expressed as

Substituting this in Eq. 5 and integrating over the patch  $\Gamma^v$ , assuming that the traction-stiffness coefficients  $k_t^x, k_t^y$ , and  $k_n$  are constant over the whole patch, yields the force–displacement relationship for the virtual node:

$$\int_{\Gamma^{v}} \begin{cases} t_{x} \begin{pmatrix} x \\ x \end{pmatrix} \\ t_{y} \begin{pmatrix} x \\ x \end{pmatrix} \\ t_{z} \begin{pmatrix} x \\ x \end{pmatrix} \end{cases} d\Gamma = \int_{\Gamma^{v}} \begin{bmatrix} k_{t}^{x} & 0 & 0 \\ 0 & k_{t}^{y} & 0 \\ 0 & 0 & k_{n} \end{bmatrix} \begin{pmatrix} u_{x}^{v} \\ u_{y}^{v} \\ u_{z}^{v} \end{pmatrix} + \begin{bmatrix} 0 & 0 & (y - y_{v}) \\ 0 & 0 & -(x - x_{v}) \\ -(y - y_{v}) & (x - x_{v}) & 0 \end{bmatrix} \begin{pmatrix} \theta_{x}^{v} \\ \theta_{y}^{v} \\ \theta_{z}^{v} \end{pmatrix} d\Gamma$$

$$\Rightarrow \begin{cases} f_{x}^{x} \\ f_{y}^{v} \\ f_{z}^{z} \end{cases} = \begin{bmatrix} k_{t}^{x} \mathbf{a}_{v} & 0 & 0 \\ 0 & k_{t}^{y} \mathbf{a}_{v} & 0 \\ 0 & 0 & k_{n} \mathbf{a}_{v} \end{bmatrix} \begin{pmatrix} u_{x}^{v} \\ u_{y}^{v} \\ u_{z}^{v} \end{cases} \qquad \text{(using, } \int_{\Gamma^{v}} (x - x_{v}) d\Gamma = \int_{\Gamma^{v}} (y - y_{v}) d\Gamma = 0 \text{)},$$

$$(50)$$

with  $\mathbf{a}_v$  denoting the total area of the patch. Similarly, by substituting Eqs. 48, into Eq. 6 leads to the moment-rotation relationship:

$$\left\{ \begin{array}{l} m_{x}^{v} \\ m_{y}^{v} \\ m_{z}^{v} \end{array} \right\} = \left( k_{n} \begin{bmatrix} I_{xx}^{v} & I_{xy}^{v} & 0 \\ I_{xy}^{v} & I_{yy}^{v} & 0 \\ 0 & 0 & 0 \end{bmatrix} + \begin{bmatrix} 0 & 0 & 0 \\ 0 & 0 & 0 \\ 0 & 0 & k_{t}^{x} \int_{\Gamma^{v}} y^{2} d\Gamma + k_{t}^{y} \int_{\Gamma^{v}} x^{2} d\Gamma \end{bmatrix} \right) \left\{ \begin{array}{l} \theta_{x}^{v} \\ \theta_{y}^{v} \\ \theta_{z}^{v} \end{array} \right\}, \tag{51}$$

with  $I_{pq}^{\nu}(p,q=x,y)$  denoting appropriate terms of the second moment of area of the patch. Assuming an isotropic surface  $(k_t^x = k_t^y = k_t)$ , the linear phenomenological model may be summarized as,

$$\begin{pmatrix}
f_{y}^{x} \\
f_{y}^{y} \\
f_{z}^{z} \\
m_{y}^{y} \\
m_{y}^{y} \\
m_{y}^{y}
\end{pmatrix} = \begin{bmatrix}
k_{t}\mathbf{a}_{v} & 0 & 0 & & & \\
0 & k_{t}\mathbf{a}_{v} & 0 & & & \\
0 & 0 & k_{n}\mathbf{a}_{v} & & & \\
k_{n}I_{xx}^{y} & k_{n}I_{xy}^{y} & 0 & \\
k_{n}I_{xy}^{y} & k_{n}I_{yy}^{y} & 0 & \\
0 & 0 & 0 & k_{t}I_{zz}^{y}
\end{bmatrix} \begin{pmatrix}
u_{x}^{y} \\
u_{y}^{y} \\
u_{y}^{y} \\
\theta_{x}^{y} \\
\theta_{y}^{y} \\
\theta_{y}^{y}
\end{pmatrix}.$$
(52)

Since the current work employs applications involving contact-separation in the normal direction and stick-slip in the tangential directions, this has to be adapted further. The linear model is useful, however, in that the non-linear contact models, upon linearization, must be consistent with this. Since a thorough treatment of this is beyond the scope of the current work, a simplified generalization is developed. The terms  $f_x^v, f_y^v$ , and  $f_n^v$  are written as a direct generalization of Eqs. 46, 47 as

$$f_n^{\nu}(u_n) = \left\{ egin{array}{ll} (k_n \mathbf{a}_{\nu}) u_n & u_n > 0 & (contact) \\ 0 & u_n < 0 & (separation) \end{array} 
ight.,$$

$$(53) f_{q}^{\nu} \left( u_{x}^{\nu}, u_{y}^{\nu} \right) = \begin{cases} 0 & f_{n}^{\nu} = 0 \\ f_{q,sp}^{\nu} & \sqrt{f_{x,sp}^{\nu-2} + f_{y,sp}^{\nu-2}} < \mu f_{n}^{\nu} & (stick) \\ \mu f_{n}^{\nu} \frac{f_{q,sp}^{\nu}}{\sqrt{f_{x,sp}^{\nu} + f_{y,sp}^{\nu-2}}} & \text{otherwise} & (slip) \end{cases}$$
(54)

Eqs. 53, 54 are nearly identical to the traction constitutive equations, except for the patch area  $\mathbf{a}_v$  that multiplies the traction stiffness coefficients, and upon linearization, this yields the first three equations in Eq. 52.

For the moment terms, the simplest formulation would be to adopt the corresponding part of the linear model in Eq. 52. However, this will not be consistent across the different kinematic states (separation; stick; slip) the patch can potentially undergo. For  $m_z^v$ , it is assumed that the linear relationship above holds when the patch is stuck, and vanishes when the patch is slipping. Physically, this is reasonable only when the rotational DoF  $\theta_z^v$  is small enough that the whole patch is either completely stuck or completely slipped translationally, and the  $\theta_z^v$  DoF does not influence a change-of-state at any point on the patch. Making a similar assumption for the in-plane moments (with contact-separation governing the moments) is a possibility  $^{14}$ , but this was numerically found to make the non-linear solvers fail for cases with small-sized patches. Therefore, for the current study, the in-plane moments  $m_z^v$  and  $m_z^v$  are both set to zero at all times and the out-of-plane moment  $m_z^v$  is related by,

<sup>14</sup> i.e., the patch separates or comes into contact "as a whole" (i.e., all points on it are either in contact or separated), implying that the terms  $m_x^v, m_y^v$  both vanish when the patch is in separated condition

$$m_z^v = \begin{cases} (k_t I_{zz}^v) \theta_z^v & \text{stuck} \\ 0 & \text{otherwise} \end{cases}$$
 (55)

There is considerable scope for improvement here since the linearization of the current phenomenological model is consistent with the linearization of the traction-based relationship only for four of the six forcing terms in Eq. 52. Furthermore, the constitutive law for the out-of-plane moment is only valid for cases where no point on the patch slips due to rotation alone 15.

#### 3.2.5. Parameter selection

In order to have some physical motivation for the parameters, rough contact results (from [48]) for a surface with asperities assumed to be distributed as a  $\beta$ -distribution are used to fix the contact stiffnesses for the reference model. Mathematically, the expressions for  $k_t$  and  $k_n$  that are used are

$$k_{t} = \frac{2(1-\nu)}{(2-\nu)} \frac{P_{avg}}{\sigma}$$

$$\frac{k_{t}}{k_{n}} = \chi \frac{(1-\nu)}{(2-\nu)},$$
(56)

wherein  $\sigma$  is the standard deviation of the interfacial asperity peak heights (taken as 1  $\mu$ m),  $\nu$  is the Poisson's ratio of the material (taken as 0.29), and  $P_{avg}$  is the averaged total pressure in the interface (fixed as total prestress divided by total area of joint). The multiplier  $\gamma$  is fixed to 2.0, following Mindlin [49]. The coefficient of friction,  $\mu$ , is arbitrarily fixed as 0.20.

#### 3.2.6. Analysis procedure

RONMA is chosen as the simulation technique used for comparing the ROMs here. The RONMA approach is a quasi-static non-linear modal analysis procedure that can be used to draw conclusions about the amplitude-modal characteristics of the system in a consistent manner. The utility of RQNMA is that it is able to calculate the hysteretic response of a nonlinear system more accurately than other quasi-static approaches. From the computed hysteresis curves, the non-linear properties of the system (i.e., the amplitude dependent natural frequencies, damping ratios, and mode shapes) can be directly deduced. A brief presentation is provided in section A for completeness. The interested reader is referred to [7] for more details.

The reference static (bolt) prestress solution is computed with the HCB model described above. Although this ignores possible nonlinear geometric effects, the magnitudes of displacements from the prestress analysis have been found to be sufficiently small in order not to make geometric effects appreciable. Therefore, the only source of nonlinearity that is considered is the contact interface itself. Furthermore, for all of the ROM simulations, the prestress solutions are computed completely using the ROMs. Special emphasis is placed on this since it is common practice in the analysis of jointed structures to linearize these systems about the static solution and conduct the nonlinear dynamic analysis separately, but the present work does not decouple the static and dynamic portions of the analysis at all. Such a coupled approach, also used in [8] (albeit with a slightly different analysis technique), is thought to be more consistent than a decoupled approach, especially when no geometric effects need to be considered (see [23,62,8] for further discussions).

For the nonlinear modal studies in the current work, twenty logarithmically spaced modal amplitude levels (denoted  $q_{i}$ , with  $k = 1, 2, \ldots$ ) are chosen to calculate the amplitude-dependent properties. RQNMA yields the relevant natural frequency for each given amplitude level, denoted by  $\omega_k$ . For the damping estimates, the solution is evaluated at 10 linearly spaced integration points (Gauss-Lobatto quadrature is used for this) between each of the above amplitude levels, and the area under the modal displacement-acceleration curve is estimated. Fig. 14 shows a schematic representation of this, with points 1 through n representing the points along the loading curve corresponding to the chosen displacement amplitude levels. Denoting the areas below each segment as  $\Delta D_i$ 's as shown, the cumulative area at any amplitude level  $q_k$  is given as the partial sum.

$$D_k = \sum_{i=1}^k \Delta D_i. \tag{57}$$

Making a computational simplification by assuming that the modal displacement-acceleration curve follows Masing's rules [16], the cyclic dissipation and effective viscous damping factor at  $q_k$  are evaluated by

$$D_k^{cyc} = -4q_k^2\omega_k^2 + 8D_k$$
, and (58)

$$D_{k}^{cyc} = -4q_{k}^{2}\omega_{k}^{2} + 8D_{k}, \text{ and}$$

$$\zeta_{k}^{eff} = \frac{D_{k}^{cyc}}{2\pi q_{k}^{2}\omega_{k}^{2}}.$$
(59)

The above simplification, in general, introduces systematic errors in the damping estimates, and a more accurate approach would not assume that Masing's rules rules hold, such as in [8]. This is, however, not of concern presently, since the above damping measure 16 is only meant to serve as a dissipation measure that is computed consistently across all the models for making comparative observations.

<sup>15</sup> Initial efforts have indicated that a trivial superposition of the contributions of the in-plane forces and out-of-plane moment is not valid for such cases.

<sup>16</sup> Strictly speaking, however, the damping factor in Eq. 59 could be referred to as the "effective Masing dissipation".

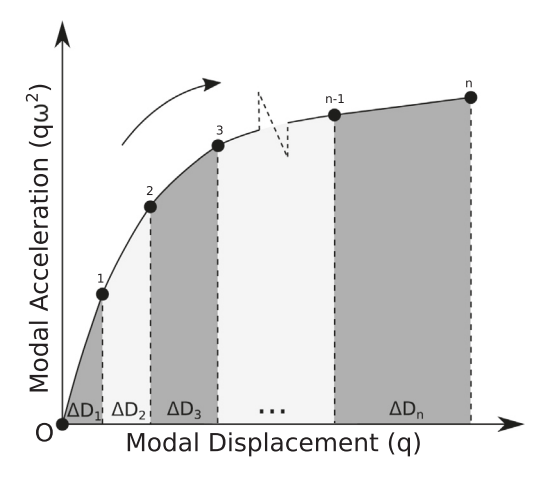


**Fig. 14.** Schematic of hysteretic analysis with n modal displacement amplitude levels.

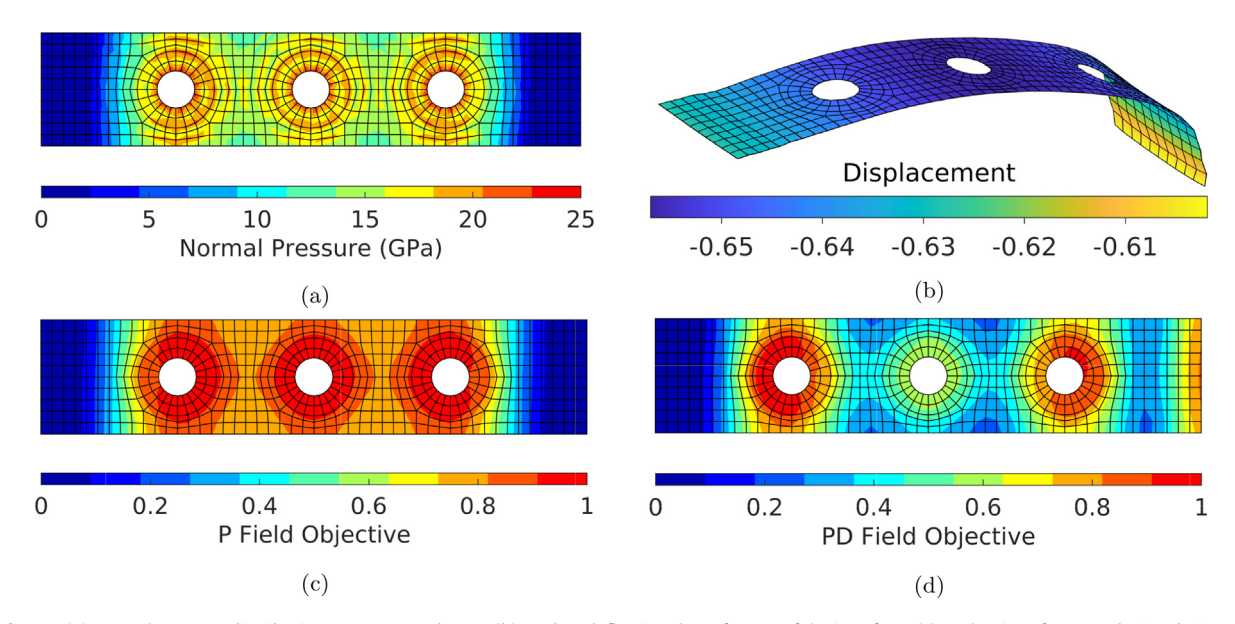


**Fig. 15.** (a) Normal pressure distribution at prestressed state, (b) mode 1 deflection shape for one of the interfaces (the other interface, not depicted, sits on top of this), and the (c) P- and (d) PD- field objectives. The P-objective is Normalized Normal pressure and the PD-objective is the normalized sum of the P-objective and normalized mass-weighted modal displacement of mode 1.

## 3.2.7. Reduced order modeling results

The current subsection presents the ROM results for the two approaches in separate subsections, followed by a comparative discussion in the last subsection where key observations are made.

For both of the ROM approaches, at least two types of field-objectives are employed for the ROM setup. The first approach, assigned the identifier "P-objective", uses as field objective the normal traction distribution at the end of static prestress analysis. The normal traction is evaluated at the nodal locations and normalized to have numerical values in the interval [0, 1]. The second approach, identified as "PD-objective", uses the average of the P-objective and the normalized mass-weighted mode-shape at the interfacial nodes (normalized, once again, to lie in the interval [0, 1]) as its field objective. The first bending mode arising from the linearization of the statically prestressed structure (with the reference mesh, depicted in Fig. 15b) is employed for the latter case <sup>17</sup>. Figs. 15c-15d plot both of these field objectives for the considered case.

The field objectives are passed through a smoothening operator in order to make the ROMs less sensitive to small variations in the field objective. A kernel-like smoothening operator is employed by resetting as nodal values a weighted average of a node's value and its connected nodal neighbour's values. The weight for its own value is fixed as 1/2 and those for the

<sup>&</sup>lt;sup>17</sup> Note that the asymmetry in the depiction arises from the fact that the inertial loading on the interface is not symmetric (see Fig. 13). The left end in Fig. 15b is connected to the rest of the corresponding half beam while the right end is free (and hence the larger deflection)

others are fixed inversely proportional to their distances such that their weights sum up to 1/2. The P-objective, therefore, looks smoother in Fig. 15c in comparison to the pressure distribution in Fig. 15a. This is a justifiable smoothening step since this is conducted only for the development of the ROMs and not after/during the non-linear simulations of any of the models.

The reference model is transformed into a "relative coordinate" system and the ROM strategies reduce the relative interfacial DoFs, i.e., the difference between the "top" and "bottom" interfaces. Denoting the set of top and bottom nodes as  $\mathscr{T}$  and  $\mathscr{B}$  respectively (with corresponding DoF vectors denoted by  $u \in \mathbb{R}^{|\mathscr{T}|}$  and  $u \in \mathbb{R}^{|\mathscr{T}|}$ ), and the set of generalized DoFs as  $\eta$  (with DoF vector  $u \in \mathbb{R}^{|\eta|}$ ), the relative coordinate transformation may be mathematically represented as

The transformation matrix  $\mathbf{T}_{rel}$  is composed of appropriate identity matrices as shown. This can be done only if the top and bottom surfaces are identically meshed (implying  $|\mathscr{T}| = |\mathscr{B}|$ ). The main advantage with this transformation is that the interfacial nonlinearites simplify by using the fact that the forces on the top and bottom nodes are of equal magnitudes and opposite signs at all times (f = -f). The nonlinear forcing vector in the relative coordinates is expressed as,

$$f_{nl}^{rel} = \underbrace{\begin{bmatrix} \mathbf{I}_{|\mathcal{F}|} & \mathbf{0} & \mathbf{0} \\ \mathbf{I}_{|\mathcal{B}|} & \mathbf{I}_{|\mathcal{F}|} & \mathbf{0} \\ \mathbf{0} & \mathbf{0} & \mathbf{I}_{|\eta|} \end{bmatrix}}_{\mathbf{T}^{T}} \underbrace{\begin{cases} \tilde{f} \\ \tilde{f} \\ \tilde{g} \\ \tilde{f} \\ \tilde{0} \\ \tilde{0} \\ \tilde{0} \end{cases}}_{\mathbf{T}^{T}} = \underbrace{\begin{cases} \tilde{f} \\ \tilde{f} \\ \tilde{o} \\ \tilde{0} \\ \tilde{o} \\ \tilde{o} \end{cases}}_{\mathbf{T}^{T}} = \underbrace{\begin{cases} \tilde{f} \\ \tilde{f} \\ \tilde{o} \\ \tilde{0} \\ \tilde{o} \\ \tilde{o} \end{cases}}_{\mathbf{T}^{T}} = \underbrace{\begin{cases} \tilde{f} \\ \tilde{f} \\ \tilde{o} \\ \tilde{o} \\ \tilde{o} \\ \tilde{o} \end{cases}}_{\mathbf{T}^{T}} = \underbrace{\begin{cases} \tilde{f} \\ \tilde{f} \\ \tilde{o} \\ \tilde{o} \\ \tilde{o} \\ \tilde{o} \end{cases}}_{\mathbf{T}^{T}} = \underbrace{\begin{cases} \tilde{f} \\ \tilde{f} \\ \tilde{o} \\ \tilde{o} \\ \tilde{o} \end{cases}}_{\mathbf{T}^{T}} = \underbrace{\begin{cases} \tilde{f} \\ \tilde{f} \\ \tilde{o} \\ \tilde{o} \\ \tilde{o} \end{cases}}_{\mathbf{T}^{T}} = \underbrace{\begin{cases} \tilde{f} \\ \tilde{f} \\ \tilde{o} \\ \tilde{o} \\ \tilde{o} \end{cases}}_{\mathbf{T}^{T}} = \underbrace{\begin{cases} \tilde{f} \\ \tilde{f} \\ \tilde{o} \\ \tilde{o} \\ \tilde{o} \end{cases}}_{\mathbf{T}^{T}} = \underbrace{\begin{cases} \tilde{f} \\ \tilde{f} \\ \tilde{o} \\ \tilde{o} \\ \tilde{o} \end{cases}}_{\mathbf{T}^{T}} = \underbrace{\begin{cases} \tilde{f} \\ \tilde{f} \\ \tilde{o} \\ \tilde{o} \\ \tilde{o} \end{cases}}_{\mathbf{T}^{T}} = \underbrace{\begin{cases} \tilde{f} \\ \tilde{f} \\ \tilde{o} \\ \tilde{o} \\ \tilde{o} \end{cases}}_{\mathbf{T}^{T}} = \underbrace{\begin{cases} \tilde{f} \\ \tilde{f} \\ \tilde{o} \\ \tilde{o} \\ \tilde{o} \end{cases}}_{\mathbf{T}^{T}} = \underbrace{\begin{cases} \tilde{f} \\ \tilde{f} \\ \tilde{o} \\ \tilde{o} \\ \tilde{o} \end{cases}}_{\mathbf{T}^{T}} = \underbrace{\begin{cases} \tilde{f} \\ \tilde{f} \\ \tilde{o} \\ \tilde{o} \\ \tilde{o} \end{cases}}_{\mathbf{T}^{T}} = \underbrace{\begin{cases} \tilde{f} \\ \tilde{f} \\ \tilde{o} \\ \tilde{o} \\ \tilde{o} \end{cases}}_{\mathbf{T}^{T}} = \underbrace{\begin{cases} \tilde{f} \\ \tilde{f} \\ \tilde{o} \\ \tilde{o} \\ \tilde{o} \end{cases}}_{\mathbf{T}^{T}} = \underbrace{\begin{cases} \tilde{f} \\ \tilde{f} \\ \tilde{o} \\ \tilde{o} \\ \tilde{o} \end{cases}}_{\mathbf{T}^{T}} = \underbrace{\begin{cases} \tilde{f} \\ \tilde{f} \\ \tilde{o} \\ \tilde{o} \\ \tilde{o} \\ \tilde{o} \end{cases}}_{\mathbf{T}^{T}} = \underbrace{\begin{cases} \tilde{f} \\ \tilde{f} \\ \tilde{o} \\ \tilde{o} \\ \tilde{o} \\ \tilde{o} \\ \tilde{o} \\ \tilde{o} \end{cases}}_{\mathbf{T}^{T}} = \underbrace{\begin{cases} \tilde{f} \\ \tilde{f} \\ \tilde{o} \\$$

If the meshes are not identical, one has to choose either a master–slave formulation or an intermediate surface mesh to represent both interfaces and appropriate interpolation matrices must be employed to compose  $T_{rel}$ . The above projection can be carried out once this is done. It must also be noted here that relative coordinate transformation may be carried out only when the relative displacements in the interface are expected to be much smaller than the sizes of the elements. This is generally found to be reasonable for bolted joint applications [8].

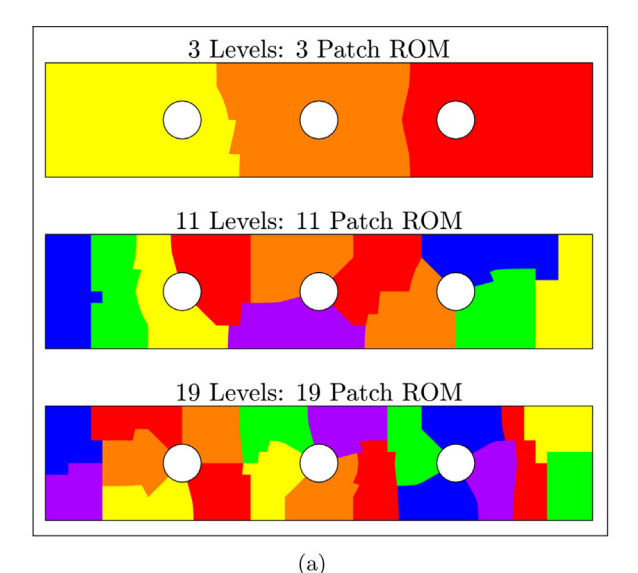
The model resulting from Eq. 60 is first reduced using another HCB step to consist of just  $\Delta u$  and generalized coordinates (using the same number of component modes as before). This is possible since the non-linearities are only expressed in the first  $|\mathcal{F}|$  DoFs of the forcing vector, with the rest being zeros, in the relative coordinate representation. All of the reference calculations are carried out using this representation. The ROM strategies developed are used as secondary reductions on this model to yield reduced representations of  $\Delta u$ . Since all simulations are conducted in a fully-free boundary configuration, the six "stuck-interface" rigid body modes are transformed out by projecting the solution onto their null-space (see [8] for the details). All of the transformation matrices are multiplied in the appropriate order and saved as the recovery matrix so as to enable the computations of the post hoc error metrics defined in section 2.3 using the mass matrix corresponding to the representation in Eq. 60, wherein the DoF vector is  $\{\Delta u \sim T, u^{sg} \sim T, u^{rg} \sim T\}^T$ , which is a common starting point for all of the ROMs.

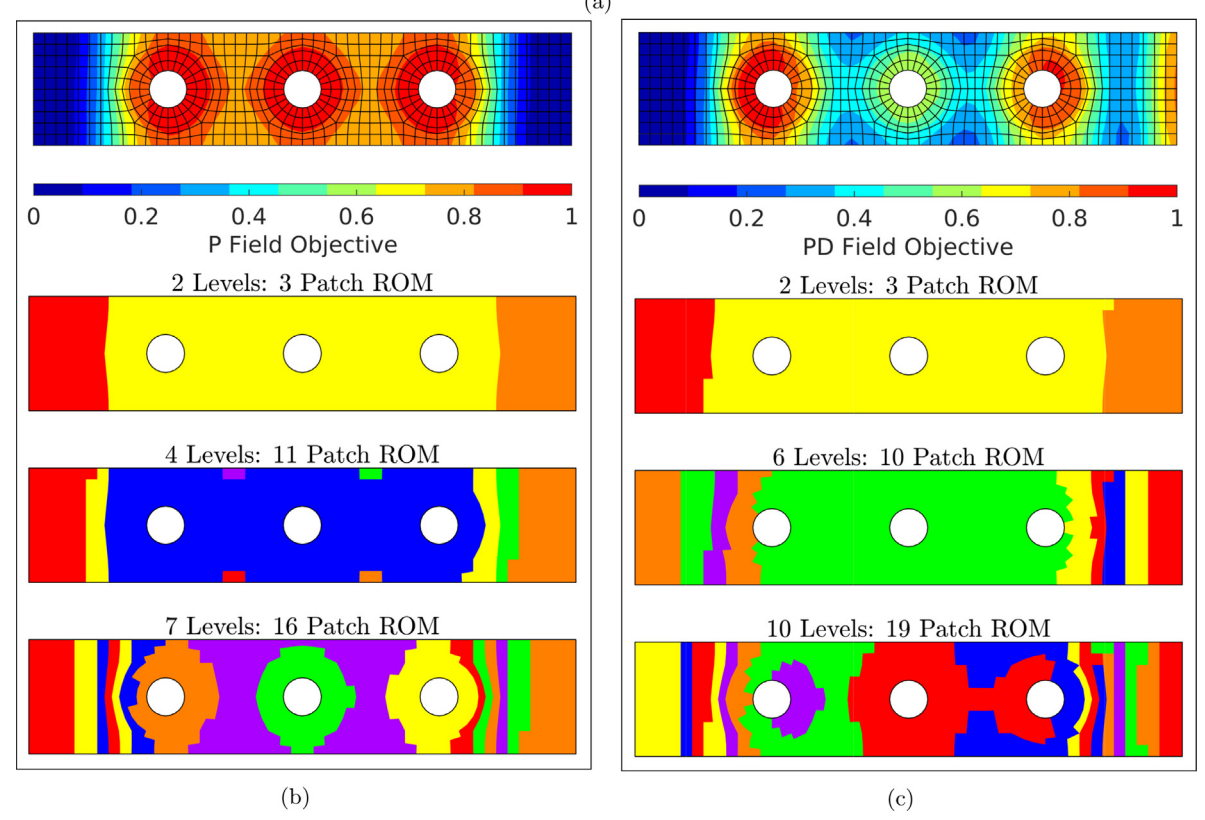
#### 3.2.8. Whole-joint approach

Employing the patching approaches outlined in section 2.1.2, several WJROMs of varying fidelity (number of DoFs) were produced. Numerical conditioning is dealt with in the same manner as in section 3.1. Indicative patches are presented in Fig. 16a-16c for the graph-clustering method, the P-objective binning and the PD-objective binning respectively.

The graph clustering approach, identified as the "U-method" in the ensuing descriptions (section 2.1.2), uses the routine mpmetis from the software package Metis [34] (version 5.1.0) to partition the dual graph of the interfacial mesh with each element weighted by its element area. The program computes a k-way partitioning for both the elements as well as the nodes of the supplied mesh. The element weights act as an additional balancing constraint that ensures that the resulting partitions all contain approximately the same areas. In general, these partitions need not be contiguous, i.e., path-connected. Appropriate flags are therefore provided to the program to ensure that the resulting partitions are contiguous.

The other two approaches, P- and PD-objective binning, are carried out in the same manner as described in section 2.1.2 (Metis is not used for these). Unlike the U-method, balancing the element areas is not a constraint here, and therefore the resulting patches can vary significantly in areas. Considerations on the appropriateness of the constraints and a careful assessment of different types of constraints are beyond the scope of the current investigation.

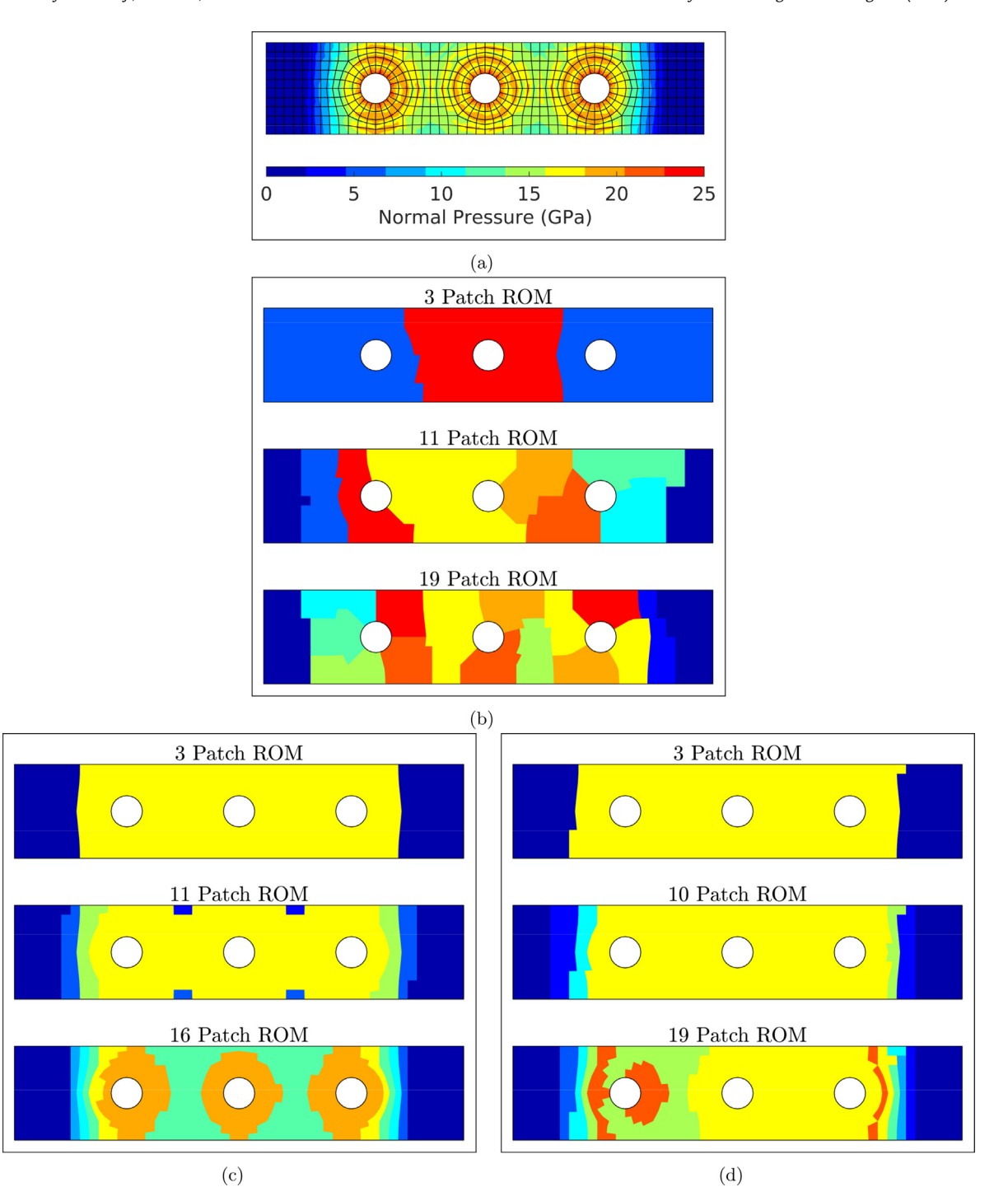




**Fig. 16.** Different fidelity patches for the Whole-Joint ROMs: (a) Metis graph-clustering based patches ("U" method); (b) P-objective on the reference mesh and the binned patches; and (c) PD-objective on the reference mesh and the binned patches. Unique arbitrary colors are assigned to each patch.

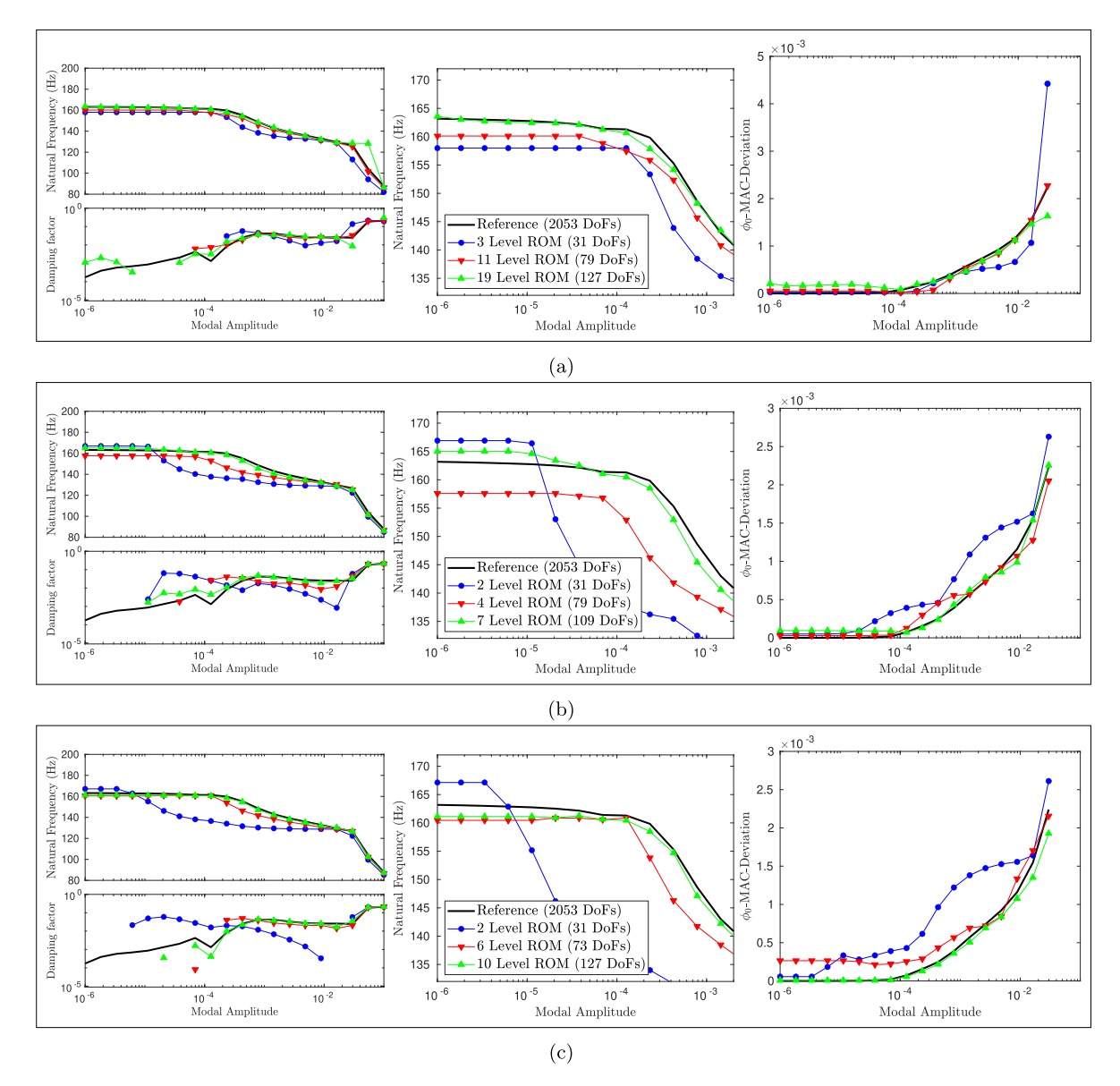
## 3.2.9. Simulation results

Fig. 17 presents the results of the prestress analysis for the different types of WJROMs. Interfacial tractions are plotted for the reference mesh alongside indicative WJROM patches. Being a prestress analysis, the patches did not develop significant out-of-plane moments (the in-plane moments are always set to zero presently, see section 3.2.4). This can be seen to be reflected in Figs. 17b–d where each patch has a constant color under the present color-mapping. Qualitatively, the P- and PD-objective patches seem to be converging to the general traction distribution of the reference for the largest DoF cases (22 and 21 patches respectively). For the U-method, on the other hand, such qualitative trends do not seem to be as directly apparent since each patch is irregularly shaped and (seemingly) arbitrarily positioned.



**Fig. 17.** Comparison of the prestress results from the Whole-Joint ROMs (WJROMs) with (a) the reference solution. Results presented for indicative whole-joint ROMs prepared using (b) U-method, (c) P-objective binning, and (d) PD-objective binning. All the figures share the colorbar in (a).

Fig. 18 depicts the RQNMA characteristics for each of the WJROMs. In terms of convergence, it can be seen that all of them demonstrate relatively acceptable convergence to the reference frequency trend. The ROMs however, seem to have more difficulty in predicting the non-linear damping trends. Particularly, at low amplitudes, the WJROMs predict nearly zero damping since none of the patches have completely slipped. The damping estimates at these amplitude levels, therefore, do not appear in the plots (which are in log-scale). At larger amplitudes, however, all of the WJROMs follow the reference closely in terms of damping too. A crucial detail that has to be mentioned at this point is the fact that unilateral linear-penalty springs



**Fig. 18.** RQNMA characteristics for the Whole-Joint ROMs (WJROMs): comparisons with reference. Results presented for indicative WJROMs prepared using (a) U-method, (b) P-objective binning, and (c) PD-objective binning. Plotted, in three columns, are the modal characteristics, magnifications of the frequency characteristics and the mode-shape deviations from the reference low amplitude mode-shape. The figure legends note the total number of DoFs (including the generalized ones) of the models in each case.

are employed to model the normal contact here. Most of the past work employing whole-joint models have only used linear springs in the normal direction (see, for instance [38,27,41,40,18,4]). However, as mentioned already, the way the unilateral normal contact is employed is not completely consistent since their influence on the in-plane moments are not modeled here.

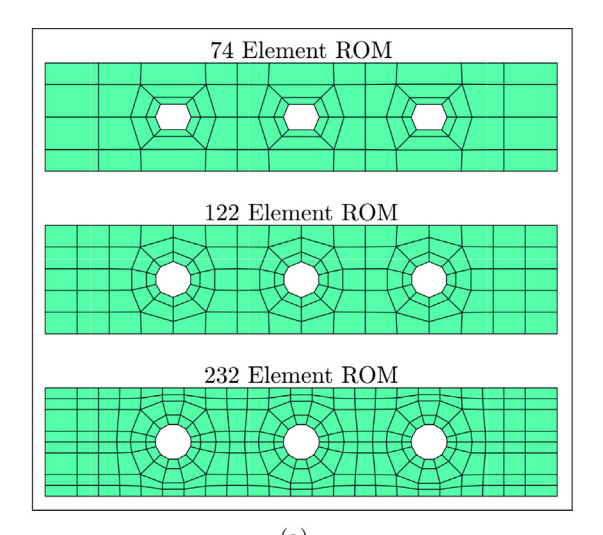
Focusing on the low amplitude behavior with respect to both frequency and damping factors (left panels in Fig. 18), it can be observed that while all of the models seem to converge to the true trend, the PD-objective and U-method binning seem to converge fastest for a comparable number of DoFs. A few outliers may also be spotted in the damping characteristics. These outliers are relics of the employment of penalty contact laws on patches that have (in the reference) only a part of its domain in contact. Due to this, a whole patch may be spuriously "flagged" as being in contact or fully separated, which may result in a spurious increase or decrease in overall stiffness.

Also plotted in the right panels in Fig. 18 are the MAC-Deviations (see Eq. 42) of the ROM predictions with the reference low-amplitude mode-shape at each modal amplitude. This metric is selected in order to make observations on the trend by which the non-linear mode-shapes deviate from the low-amplitude mode-shape of the reference. At low amplitudes, the ROMs show slight deviations from the reference, but it can be seen that the overall trend is captured satisfactorily.

## 3.2.10. Interface re-meshing approach

The mesh-reduction approaches outlined in section 2.2.2 are used to generate uniform and field-objective weighted meshes. To guarantee a symmetric reduced mesh, the reduced mesh is developed only on a quarter of the interface, and reflected twice before application. section C provides a step-by-step example for one particular case.

Fig. 19 depicts the reduced meshes generated. The uniform coarsening approach (identified as the "U-method", also followed before in section 3.1.2) yields regular meshes (see Fig. 19a), but these do not perform very well near the holes, i.e., faceting of the geometry. The P-objective remeshing (see Fig. 19b), due to the nature of the objective, produces skewed elements. As the number of required elements is increased, some elements are generated that are even smaller than those in the reference mesh, leading to spurious results (e.g., see the "304 Element ROM" in Fig. 19b). This indicates that the field objective employed is critical in determining the nature and applicability of the reduced mesh. The PD-objective remeshing (see Fig. 19c) does not seem to have similar issues at comparable numbers of elements. Related observations may be observed in



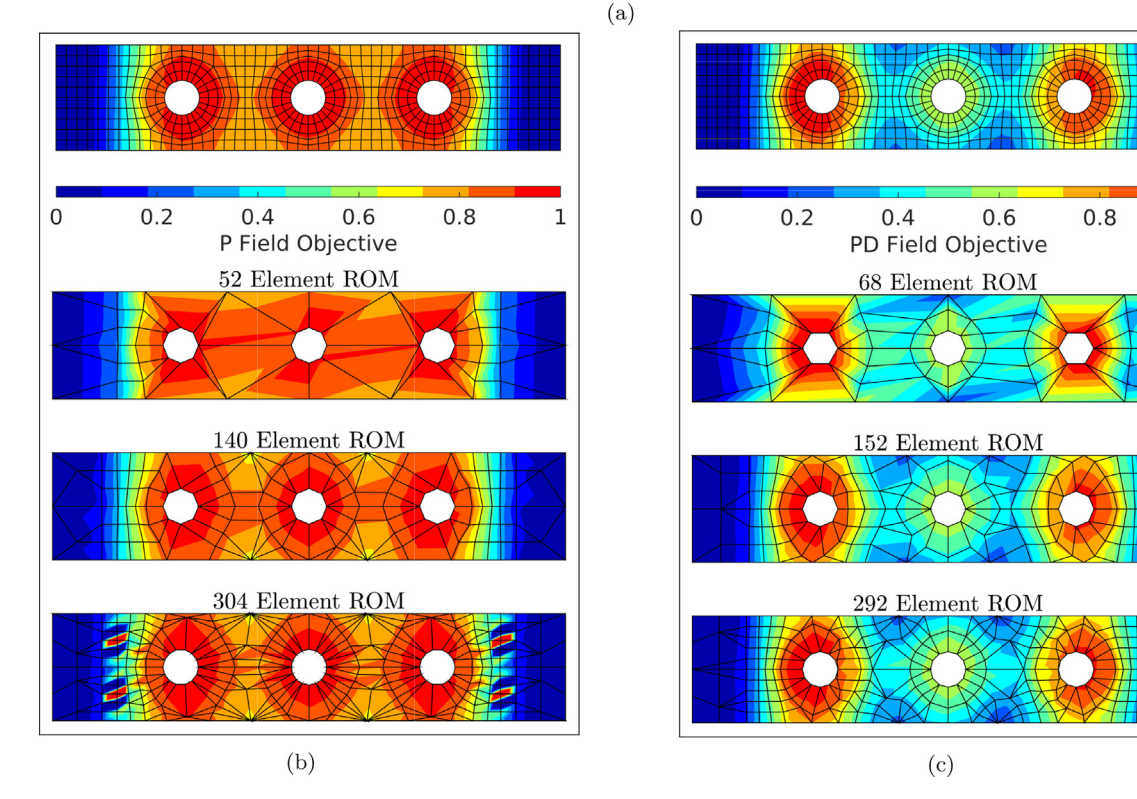


Fig. 19. Depiction of the reduced meshes for studying the Re-Meshing ROMs (RMROMs) for the (a) uniform remeshing (U-method), (b) P-objective remeshing, and (c) PD-objective remeshing cases. (b)–(c) also contain their corresponding field objectives on the reference mesh and interpolations of the same on the reduced meshes.

the interpolations of the field objectives in the corresponding figures above: the PD-objective approach seems to exhibit better capacity in interpolating its objective.

# 3.2.11. Simulation results

Fig. 20 presents the results of static prestress analysis conducted on the RMROMs. Note that since the interpretation of the traction is preserved across all of the meshes, the traction fields may be compared consistently with the reference. The first

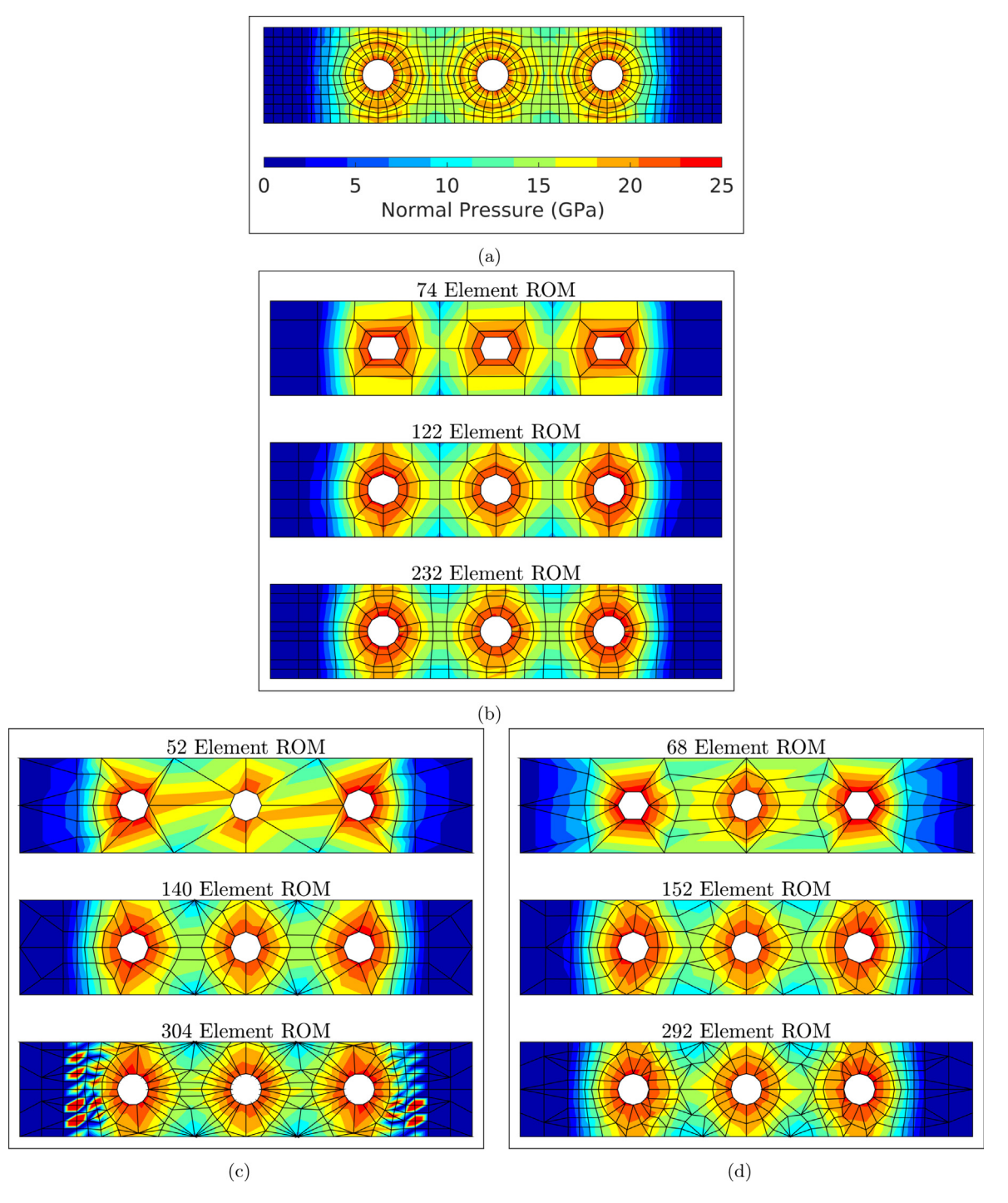


Fig. 20. Comparison of the prestress results from the Re-Meshing ROMs (RMROMs) with the (a) reference normal traction field. Results presented for indicative RMROMs prepared using (a) U-method, (b) P-objective remeshing, and (c) PD-objective remeshing. All of the figures share the colorbar in (a).

observation that may be made from the figure is that the U-method and the PD-objective remeshing exhibit much more regular traction distributions (qualitatively similar to the reference), while the P-objective remeshing seems to show spurious structures in the high gradient sections. This compliments the observations made from the interpolations and the element shapes in Fig. 19. Note that the developed procedure was unable to make all of the elements on the meshes for the P-objective element satisfy the shape regularity requirements.

The RQNMA characteristics of the RMROMs, depicted in Fig. 21, demonstrate convergence in terms of both the frequency and damping factor characteristics. The P-objective seems to diverge after first converging to the reference for larger element numbers (see Fig. 21, – possibly due to the poor quality of the elements in such regimes. Looking at the low amplitude regimes for the frequency, a clear asymptote is visible and convergence is seen for the other two approaches. The damping factor, save for the very low amplitude regime (corresponding to nearly zero damping), converges almost exactly to the reference. As in Fig. 18, the third column here shows the trend in mode-shape deviation from reference low-amplitude mode-shape. Unlike the WJROMs, it can be seen that there are no remarkable deviations in the low-amplitude regimes. For larger amplitudes, the trends can be seen to be captured satisfactorily. The RMROMs are therefore hyper-reduced ROMs with more than fourfold size (DoF) reduction, which means that non-linear function evaluations as well as hysteretic variable storage

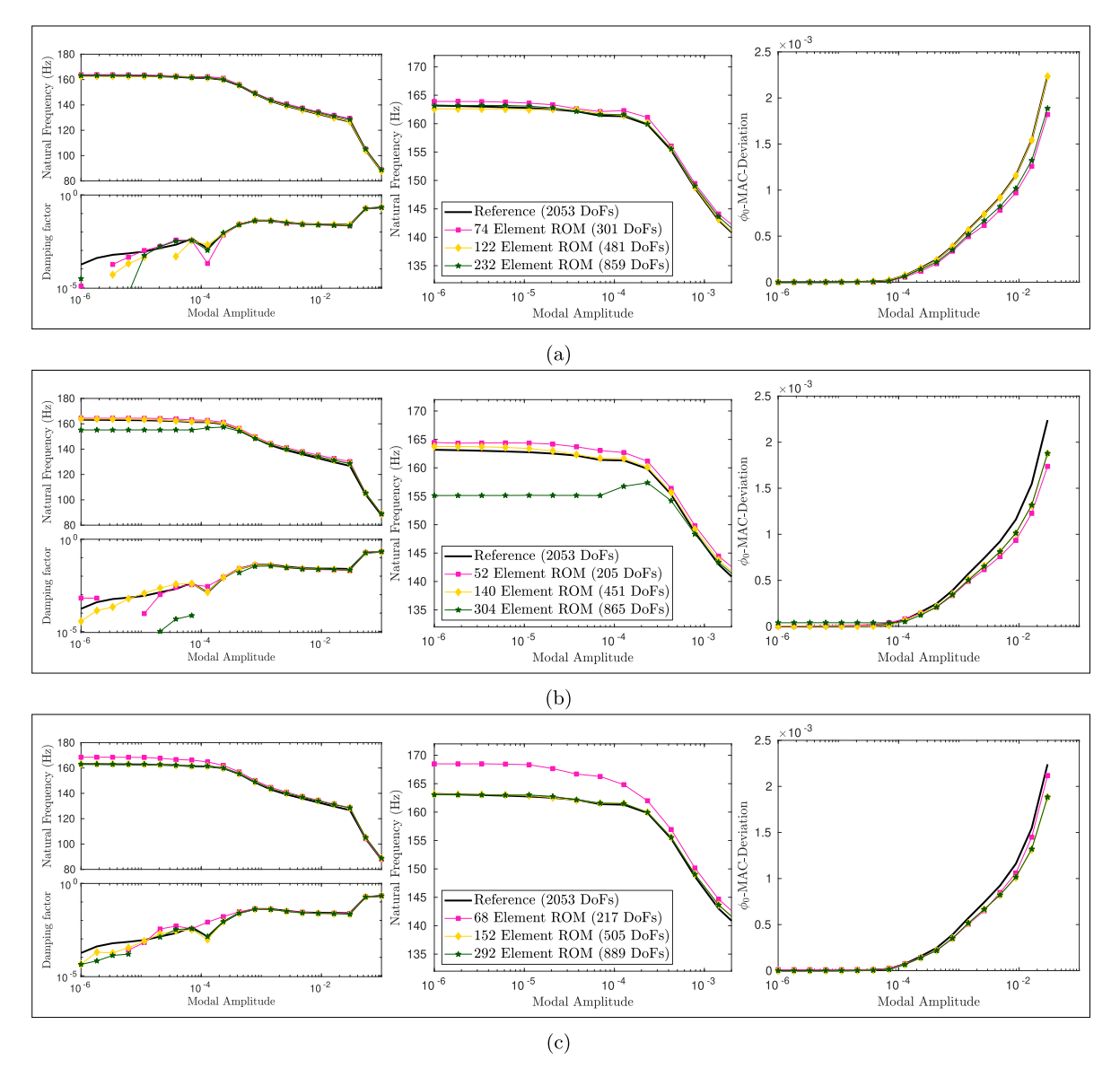


Fig. 21. RQNMA characteristics for the Re-Meshing ROMs (RMROMs): comparisons with reference. Results presented for indicative RMROMs prepared using (a) U-method, (b) P-objective remeshing, and (c) PD-objective remeshing. Plotted, in three columns, are the modal characteristics, magnifications of the frequency characteristics and the mode-shape deviations from reference low amplitude mode-shape. The figure legends note the DoFs of the models in each case.

overhead is at least that many times improved, and matrix operations and solve steps can be expected to be 16-  $(\mathcal{O}(N^2))$  and 64-fold  $(\mathcal{O}(N^3))$  faster than the original model.

#### 3.2.12. Discussions

In addition to the error metrics described in section 2.3, relative RMS errors are defined for assessing the frequency and damping characteristics with the following definitions:

$$\Delta \omega \triangleq \sqrt{\frac{1}{n} \sum_{i=1}^{n} \left( \frac{\left(\omega_{rom}(Q_i) - \omega_{ref}(Q_i)\right)}{\omega_{ref}(Q_i)} \right)^2}, \quad \text{and},$$
 (62)

$$\Delta \zeta \triangleq \sqrt{\frac{1}{n} \sum_{i=1}^{n} \left( \left( \frac{\zeta_{rom}(Q_i) - \zeta_{ref}(Q_i)}{\zeta_{ref}(Q_i)} \right)^2}.$$
 (63)

The trends of the relative static solution errors, mean mode shape deviations, and the above RMS errors are plotted against the ROM size (model DoF) in Fig. 22. For the WJROMs, it was possible only in the case of the "U-method" (graph clustering) to develop WJROMs with very large model sizes. For the field objective approaches, increasing the number of levels resulted in ROMs with one or more patches consisting of just a single element on the interface. Such configurations were avoided since such a scenario is not a realistic application of a whole-joint reduced model.

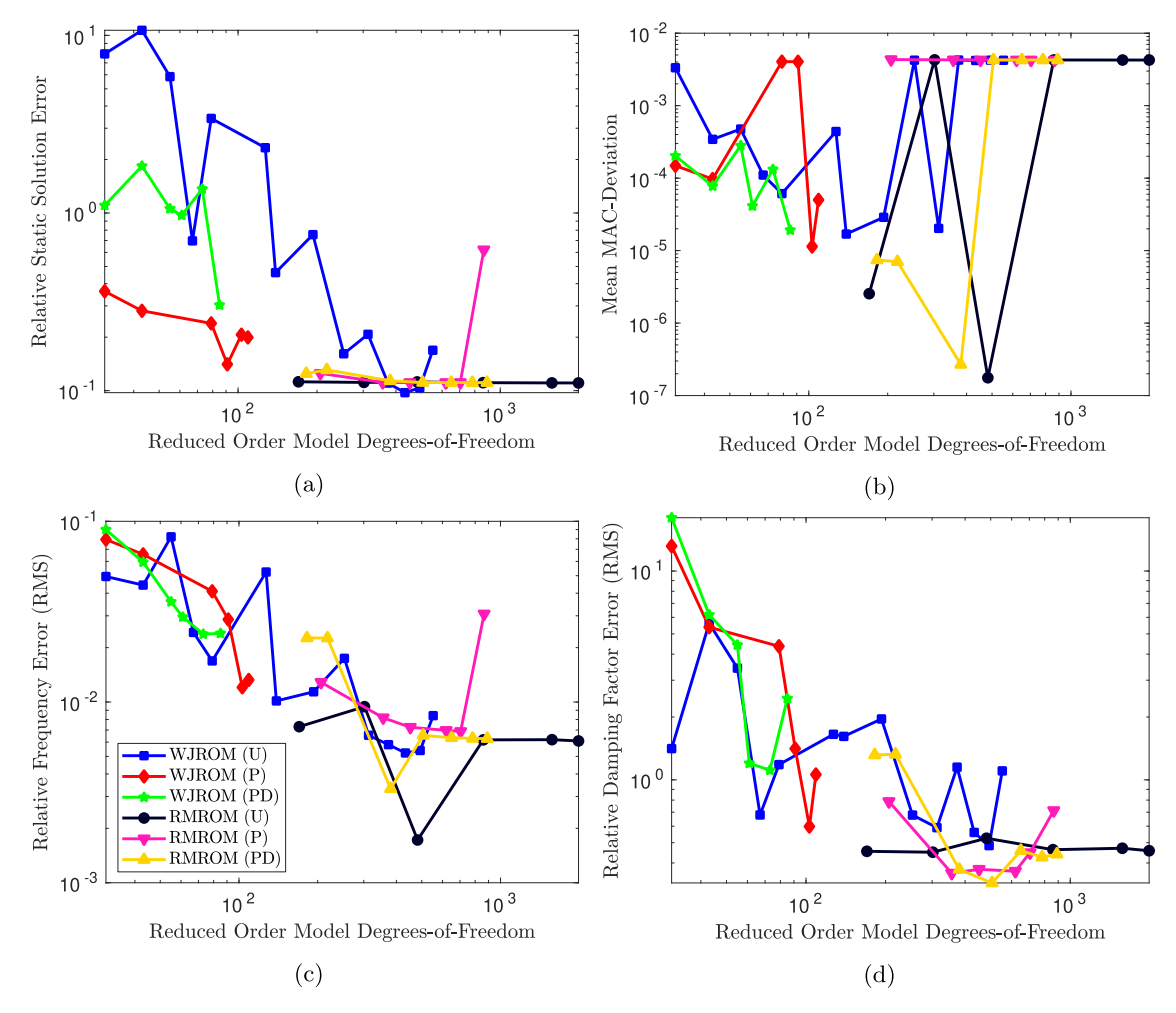


Fig. 22. Error trends for the Whole-Joint (WJROM) and Re-Meshing (RMROM) reduced order modeling approaches. Plotted are the (a) Relative static solution errors (see Eq. 41), (b mean non-linear mode shape deviation over the range of modal amplitudes, and relative root-mean-squared errors in the non-linear modal (c) frequency and (d) damping factor characteristics with respect to the reference characteristics. The quantities are plotted against the ROM DoFs to illustrate comparative trends across the ROMs.

In terms of the static solution error characteristics (Fig. 22a), it can be observed that small sized WJROMs perform very poorly but the larger models all seem to converge consistently to some lower limit of about  $10^{-1}$ . The lower bound is reminiscent of trends observed earlier in section 3.1 due to the (fixed-interface modal) truncation errors introduced by HCB. This is conjectured to be the case for the non-linear results here too.

The non-linear mode-shapes are compared by evaluating the mean MAC-Deviation (see Eq. 43) between the mode-shapes predicted by the reference and the ROM, over the set of modal amplitudes considered. Fig. 22b depicts the trends of this mean MAC-Deviation, wherein it can be observed that there is a good match between the mode-shapes for all of the ROMs.

From the frequency error characteristics (Fig. 22c), it can be observed that, save for a few outliers, all of the ROMs seem to have a similar trend of convergence with the model size. All of the models have an initial convergence region, with the errors saturating at a lower limit for large-sized ROMs (once again strongly reminiscent of the trends seen for the linear case in section 3.1 due to HCB-truncation). The RMROM model with the P-objective remeshing shows how the error increases at the last point (for reasons discussed previously). In terms of the damping errors, Fig. 22d shows a trend similar to the frequency errors. In both of these, the "U-method" ROMs are the most versatile, while at the same time seem to yield models that are at par with the field-objective approaches. This shows that the pursued field objective approaches do not offer any advantages over the uniformly reduced models.

Fig. 23 reports the CPU-times taken for reduced order model preparation (Fig. 23 and the RQNMA simulations that were conducted for the studies before (Fig. 23b). All of the computations were conducted on an intel i7-7700 HQ machine with 16 GB of RAM and 2.5 GHz clock-speed with four physical cores (no explicit parallelization was conducted other than MATLAB vectorization). For the WJROMs, the U-method can be seen to take significantly less preparation time than the field objective approaches. This is possibly due to the fact that metis, written primarily in C, is used for generating the patches for the U-method while MATLAB implementations (invovling graph adjacency matrix computation, connected component search, etc.) are employed for the field objective approaches. It may also be seen that the RMROM approaches generally take longer to be set up. The most expensive operations here, apart from matrix-matrix multiplications and linear solves, is mesh searching to obtain interpolants of the quadrature locations of the reference mesh using the reduced mesh nodal coordinates. Significant improvements may be made in each of these cases through optimized (and parallel) codes.

With regards to the simulation times, it can be seen that all of the models seem to scale identically with the number of DoFs (asymptote to  $\mathcal{O}(N^2)$ ). Note that the reported time is for the complete hysteretic calculation, not just a single matrix solve - so these times include influences of number of iterations for convergence, specific solver employed, etc., and can be expected to differ from application to application. It can, however, be seen that computational gains of a few orders of magnitude is possible with the proposed ROM techniques.

The main observation that may be made from the convergence plots in Fig. 22 and the CPU times in Fig. 23 is that sufficiently large whole joint models with patches selected using graph partitioning approaches compares favorably among the other techniques under consideration for finite element interface reductions for the current class of problems. These are observed to lead to ROMs with accuracy comparable to the remeshing approach even though their descriptions (and setup) are much simpler than the latter. However, the fact remains that the employed constitutive model is not completely consistent with the reference and more work is necessary here before these ROMs may be used confidently. Moreover, as already noted, no significant improvement in the performance of the ROMs that employed the adopted field objective approaches are observed (in comparison to the U-methods). The fact that the U-method ROMs, which have been constructed independent of

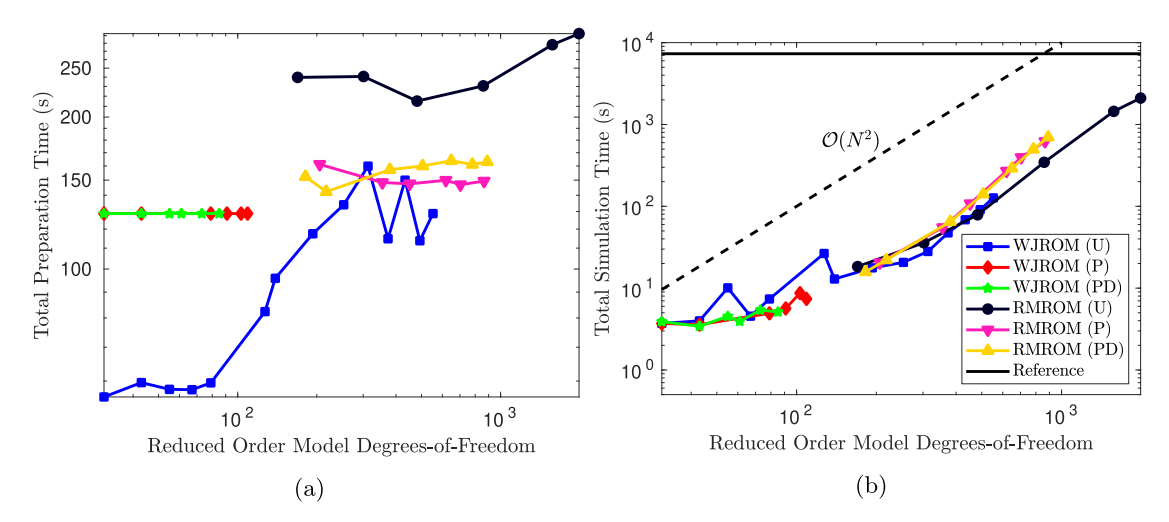


Fig. 23. CPU-time taken for (a) ROM preparations (offline costs), and (b) nonlinear simulation (online costs). The  $\mathcal{O}(N^2)$  trend-line is shown in (b) using a dashed line.

the results from the non-linear simulations or any parameters employed therein, perform well for the non-linear case considered here is indicative of the fact that it could perform well for other conditions (higher vibration modes, different prestress levels, boundary conditions, geometries, etc.).

#### 4. Conclusions

Two hyper-reduction formulations have been developed and formulated for applications of structures with contact nonlinearities. The physical interpretation of the developed Reduced Order Models (ROMs) is preserved through the formulations so that there will be no necessity for one to shift to and from the reference model for the evaluation of the nonlinear forces. Since the formulations here are not based on data training, neither of these approaches suffer from the drawbacks related to data extrapolation, and are as accurate as the fidelity of the ROM and the consistency of the constitutive models allow them to be.

The specific contributions of this paper are,

- A whole-joint constraint formulated specifically for contact applications;
- Initial efforts at developing a whole-joint constitutive modeling approach for a contact interface that is consistent with a high-fidelity FE representation of the same;
- A hyper-reduced interface remeshing approach that is verified against a reference FE representation;
- Explorations of possible approaches for constructing reduced order representations for both of the above;
- Comparative perspectives on the applicability of the two different types of reduction that are not often seen together in the literature.

In comparing the results of the two approaches for the provided examples, it is concluded that the employment of the WJROMs has a great potential for being efficient strategies for bolted joint applications. The main drawback here is that the available techniques in the literature for contact constitutive relationships for such whole-joint representations is still not mature enough to consider them completely consistent (up to the first order rotations and moments).

With regards to the RMROMs, the results indicate that consistent ROMs may be constructed using this technique for bolted joint applications to yield significant size reduction. However, other formulations for the re-meshing must be explored since a more careful consideration of the expected interfacial physics could potentially lead to a representation that is more efficient than the U-method (which turned out to perform comparably here). A promising possibility is the use of classical adaptive mesh refinement strategies (see [42,39], for instance) to conduct the remeshing "online" with the non-linear calculations. The "training-free" spirit of the current investigation is, however, slightly compromised here.

#### **Declaration of Competing Interest**

The authors declare that they have no known competing financial interests or personal relationships that could have appeared to influence the work reported in this paper.

## **CRediT authorship contribution statement**

**Nidish Narayanaa Balaji:** Data curation, Formal analysis, Investigation, Methodology, Software, Validation, Visualization, Writing - original draft. **Tobias Dreher:** Investigation, Software, Visualization. **Malte Krack:** Resources, Supervision, Writing - review & editing. **Matthew R.W. Brake:** Conceptualization, Funding acquisition, Project administration, Resources, Supervision, Writing - review & editing.

## Acknowledgments

The authors wish to acknowledge the software package Metis [34] (version 5.1.0), which both facilitated the whole joint modeling reductions and generated further ideas for interface reduction using graph clustering techniques as part of our future work.

Funding: This material is based upon work supported by the National Science Foundation under Grant No. 1847130.

## Appendix A. Rayleigh-quotient based non-linear modal analysis

The current appendix provides an overview of the key steps involved in RQNMA. The interested reader is directed to [7] for a full presentation along with comparisons.

Given a non-linear dynamical system of the form

$$\mathbf{M} \overset{"}{\underset{\sim}{u}} + \mathbf{K} \underset{\sim}{u} + F_{nl} \left( \overset{"}{\underset{\sim}{u}} ; u_0 \right) = F_s + F_{\text{ext}}(t), \tag{64}$$

with **M** and **K** denoting the mass and stiffness matrices respectively;  $F_s$  being a static load vector;  $F_{nl}$  being a non-linear force (possibly with hysteretic terms  $u_0$ ); and  $F_{ext}(t)$  being the external forcing terms. Denoting the solution of the static problem by  $u^*$  that satisfies

$$\mathbf{K} \overset{*}{\underbrace{\mathbf{u}}} + F_{nl} \left( \overset{*}{\underbrace{\mathbf{u}}} \right) = F_{s}, \tag{65}$$

RQNMA provides governing equations for obtaining non-linear modes as finite perturbations/deviations from  $\overset{*}{u}$ . For the system in Eq. 64, the system of equations

$$\mathbf{K} \underbrace{\mathbf{u} + F_{nl}}_{\sim} \left( \underbrace{\mathbf{u}}_{\sim}; \mathbf{u}_{0} \right) - F_{s} - \omega^{2} \mathbf{M} \left( \underbrace{\mathbf{u} - \mathbf{u}^{*}}_{\sim} \right) = 0$$

$$\left( \underbrace{\mathbf{u} - \mathbf{u}^{*}}_{\sim} \right)^{T} \mathbf{M} \left( \underbrace{\mathbf{u} - \mathbf{u}^{*}}_{\sim} \right) - q^{2} = 0,$$
(66)

have as solutions the Rayleigh-Quotient based Non-Linear Modes (RQNM's),  $\left\{u(q) - u\right\}$  and modal frequency  $\omega(q)$ , both parameterized by the modal amplitude q. Solving this for a set of modal displacements allows one to plot the hysteresis in the modal domain (modal displacement q versus modal acceleration  $q\omega^2$ ) by updating  $u_0$  at turning points. In the current case, however, since the structure is symmetric, the hysteretic loop is expected to be symmetric, i.e., obey Masing's rules. Therefore, cyclic dissipation may be estimated based on just the area under the q- $q\omega^2$  curve using (see [46,6]) for details)

$$D^{cyc}(Q) = -4Q^2\omega(Q)^2 + 8\int_0^Q Q\omega(Q)^2dQ,$$
(67)

where *Q* is the maximal response modal amplitude. The integral is evaluated numerically by conducting the analysis at Gauss–Lobatto quadrature points (quadrature points including ends) and carrying out the weighted summation. The equivalent linear viscous damping factor is calculated by comparing this with the cyclic energy dissipated by a linear viscous damping term:

$$\zeta^{\text{eff}}(Q) = \frac{D^{\text{cyc}}(Q)}{2\pi 0^2 \omega^2}.$$
(68)

In practice, since the results are needed on a coarse grid  $Q_1, Q_2, \ldots$ , numerical integration is conducted (using quadrature points) between these and accumulated for the total dissipation estimate as described in section 3.2.

## Appendix B. Force-traction relationships in the whole joint ROMs

The present appendix provides visual representations of the relationships between the forces and tractions for patches reduced using the whole joint procedure. The mathematical expressions given in Eq. 5, are plotted for unit forcing along each component. The five-patch WJROM developed in section 3.1.1 will be used for the illustrations.

The whole joint forces are set as unit forcing in the six components (three forces and three moments) on the virtual node corresponding to the central patch in the ROM. The area of this patch is  $7.0678 \times 10^{-4}$  m<sup>2</sup> and the second moment of area tensor (in matrix notation) is

$$\begin{bmatrix} \mathbf{I}_{XX} & \mathbf{I}_{XY} & \mathbf{I}_{XZ} \\ \mathbf{I}_{YX} & \mathbf{I}_{YY} & \mathbf{I}_{YZ} \\ \mathbf{I}_{ZX} & \mathbf{I}_{ZY} & \mathbf{I}_{ZZ} \end{bmatrix} = \begin{bmatrix} 4.0725 \times 10^{-8} \, m^4 & 0 & 0 \\ 0 & 5.6907 \times 10^{-8} \, m^4 & 0 \\ 0 & 0 & 9.7632 \times 10^{-8} \, m^4 \end{bmatrix}.$$
(69)

Fig. 24 depicts the traction fields for each of the forcing cases.

## Appendix C. Sample re-meshing procedure for the BRB interface

The present appendix provides a step-by-step illustration of the developed approach for generative a mesh based on a field objective (normalized to have a value from 0 to 1). The algorithm consists of three major steps:

- 1. Place nodes on appropriate contour lines of the field objective
- 2. Adjust the nodes to retain key geometric features of the reference mesh
- 3. Mesh the nodes based on different quality metrics

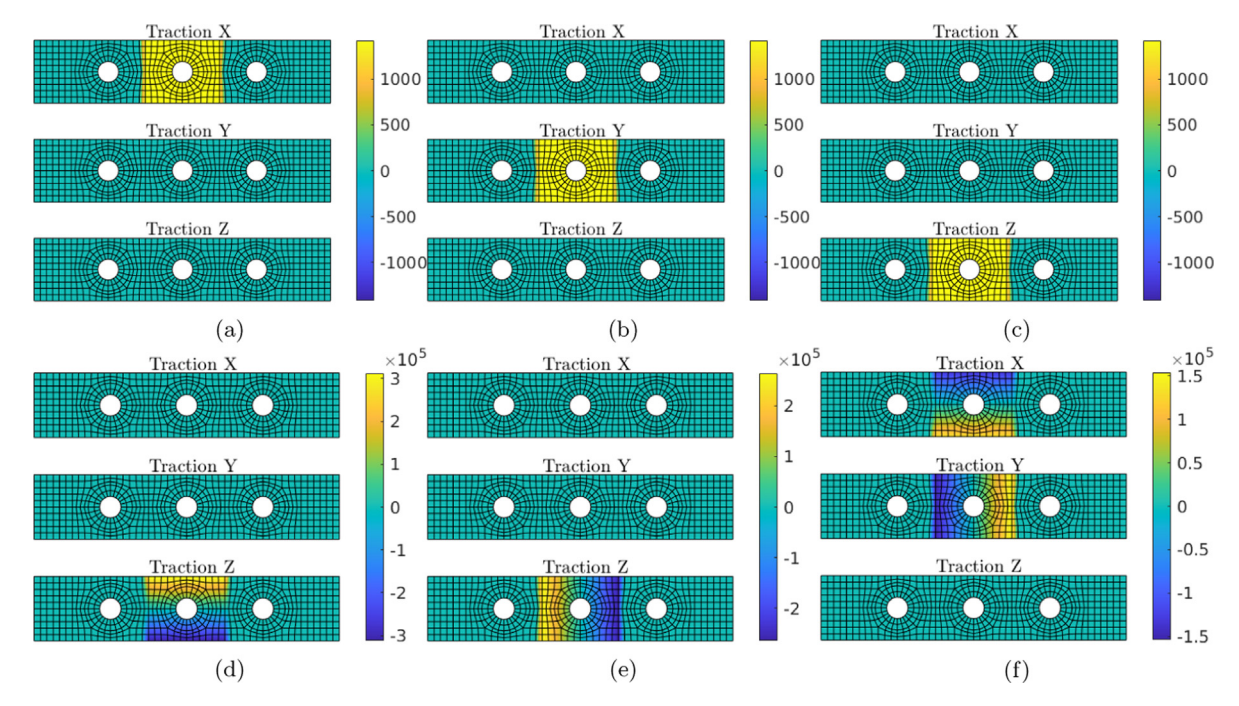


Fig. 24. Traction fields (all units in Pa) corresponding to (a-c) 1 N forces in the X, Y, and Z directions respectively, and (d-f) 1 Nm moments in the X, Y, and Z directions respectively. The positive X and Y directions are across the left-right and bottom-top directions on the plane of the paper respectively, and the positive Z direction is such that they form a right-handed system.

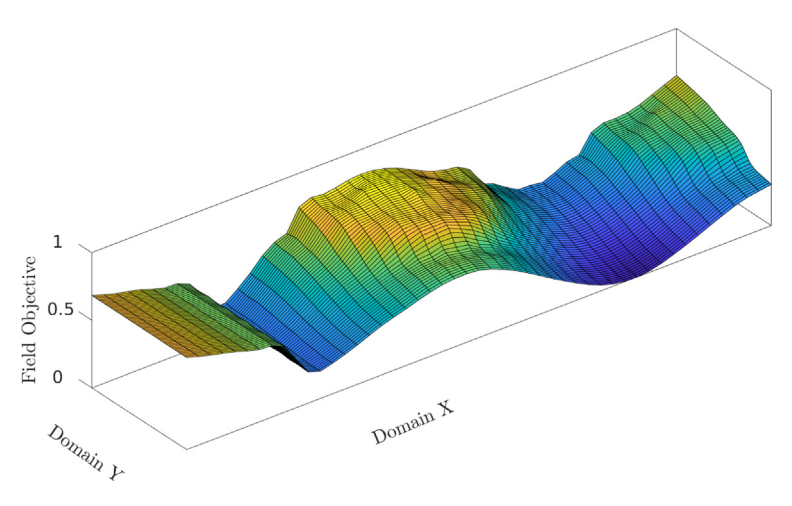


Fig. 25. 3D interpolation of objective function.

Given a reduction level (in terms of required number of elements), the above steps are conducted for different numbers of contour lines and "seeding factors" (controlling how nodes are seeded on each contour line) and the appropriate configuration is chosen based on how closely the number of elements in the resulting mesh matches the required reduction level.

Consider the PD-objective remeshing for the BRB interface. Using a biharmonic interpolation (implemented in MATLAB), a 3D surface of the objective function is developed over a quarter of the domain (see Fig. 25). As previously mentioned, the remeshing procedure is conducted on just a quarter in order to ensure that the resulting mesh is symmetric. Note that this interpolation defines the field even over the regions where there is a hole in the original domain. Contour lines of this surface are generated and nodes are seeded on it (step 1). In order to avoid the effects of local extrema on the field objective (arising due to a non-smooth field, interpolation relics, etc.), contour lines that are much shorter in comparison to others are removed for this step. A "seeding factor" is used to control the spacing between the nodes on each contour level. Different combinations of the number of contour levels and seeding factors are considered to determine the right setting that yields a mesh

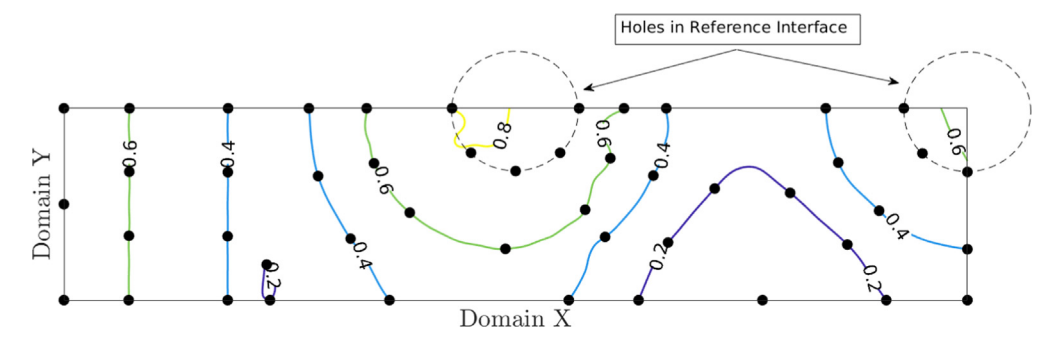


Fig. 26. Contour lines of the field objective (labels indicate normalized contour levels). The black markers denote the seeded nodes. The dashed circles indicate the holes in the reference interface that are used for the adjustments.

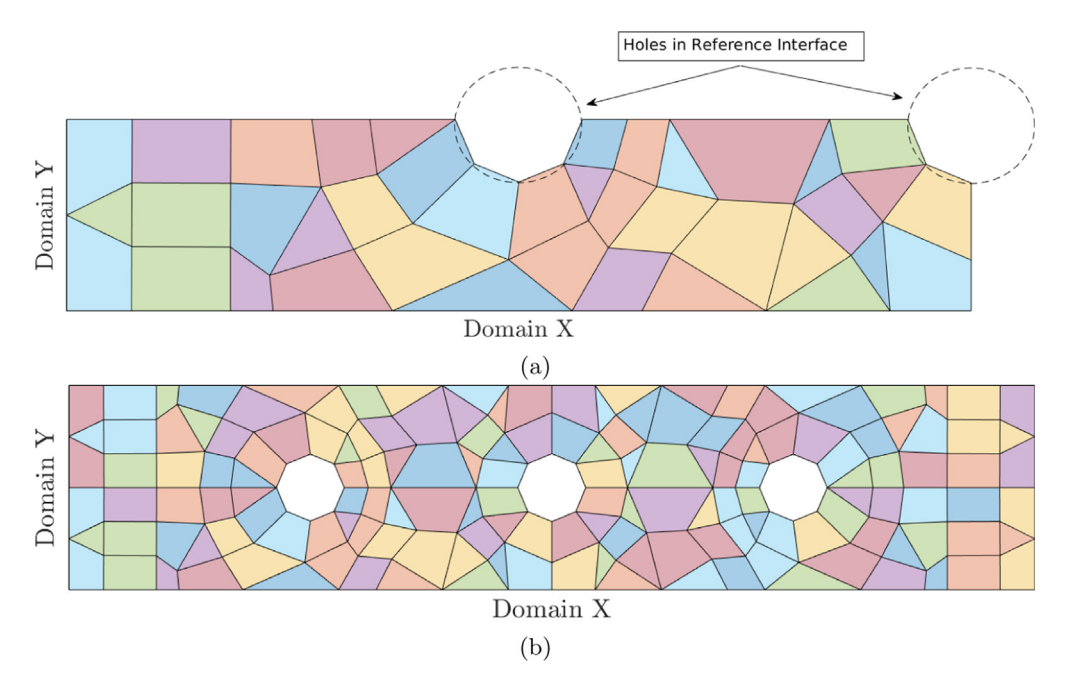


Fig. 27. Meshes generated on the quarter and full (upon reflection) domains. The element coloring is arbitrary.

close enough to the required reduction level. Next, the nodes within the region of the holes and corners are adjusted so as to preserve the reference geometry. Fig. 26 depicts the contour lines of the interpolated field above and the seeded (and adjusted) nodes from steps 1–2. Nodes that were previously seeded within the bolt region (i.e., outside the reference domain) are adjusted to lie along the boundary. In addition to this, other adjustments are carried out, such as collapsing closely spaced nodes into a single node, ensuring that there is a node at the corner points, etc.

The above seeded nodes are then meshed using triangular elements using Delaunay triangulation (as implemented in the MATLAB routine delaunay <sup>18</sup>). More nodes are added here to preserve shape regularity of the elements. After this, pairs of adjoining triangular elements are combined to form a single quadrilateral element if the resulting element is deemed to be of acceptable quality (based on an upper limit of 0.75 set for the equi-angular skewness). Fig. 27a depicts the meshed surface from this step. It can be seen that some triangular elements are retained in the final output since it was not possible to combine them appropriately to produce acceptable quadrilateral elements. Mirroring this mesh twice over the domain yields the mesh of the total domain (interface), as shown in Fig. 27b.

<sup>18</sup> https://www.mathworks.com/help/matlab/ref/delaunay.html.

#### References

- [1] METIS Serial Graph Partitioning and Fill-reducing Matrix Ordering Karypis Lab. URL URL: http://glaros.dtc.umn.edu/gkhome/metis/metis/overview.
- [2] M. Afzal, I. Lopez Arteaga, L. Kari, An analytical calculation of the Jacobian matrix for 3d friction contact model applied to turbine blade shroud contact. Comput. Struct. 177 (2016) 204–217. ISSN 00457949. doi: 10.1016/j.compstruc.2016.08.014.
- [3] R.J. Allemang, The modal assurance criterion-twenty years of use and abuse, Sound Vib. 37 (8) (2003) 14-23.
- [4] M.S. Allen, R.M. Lacayo, M.R.W. Brake, Quasi-static modal analysis based on implicit condensation for structures with nonlinear joints, in: International Conference on Noise and Vibration Engineering, Leuven, Belgium, September 2016.
- 5] Mechanical APDL ANSYS, Theory Reference, ANSYS Inc, Canonsburg, 2006.
- [6] N.N. Balaji, M.R.W. Brake, The surrogate system hypothesis for joint mechanics, Mech. Syst. Signal Process. 126 (2019) 42–64. ISSN 0888-3270. doi: 10.1016/j.ymssp.2019.02.013.
- [7] N.N. Balaji, M.R.W. Brake, A quasi-static non-linear modal analysis procedure extending rayleigh quotient stationarity for non-conservative dynamical systems, Comput. Struct. 230 (2020) 106184.
- [8] N.N. Balaji, W. Chen, M.R.W. Brake, Traction-based multi-scale nonlinear dynamic modeling of bolted joints: formulation, application, and trends in micro-scale interface evolution, Mech. Syst. Signal Process. 139 (2020) 106615.
- [9] J. Becker, L. Gaul, Cms methods for efficient damping prediction for structures with friction, Proceedings of the IMAC-XXVI, Orlando, 2008.
- [10] J.H. Bickford, Introduction to the Design and Behavior of Bolted Joints: Non-Gasketed Joints. CRC Press, 0 edition, August 2007. ISBN 978-0-429-12826-4. doi: 10.1201/9780849381874. URL URL:https://www.taylorfrancis.com/books/9780849381874.
- [11] S. Bograd, P. Reuß, A. Schmidt, L. Gaul, M. Mayer, Modeling the dynamics of mechanical joints, Mech. Syst. Signal Process. 25 (2011) 2801–2826.
- [12] K. Brahmi, N. Bouhaddi, R. Fillod, Reduction of junction degrees of freedom in certain methods of dynamic substructure synthesis, in: Proceedings of the 13th International Modal Analysis Conference, Nashville, Tennssee, USA, February 1995, pp. 1763–1769.
- [13] M.R.W. Brake (Ed.), The Mechanics of Jointed Structures, Springer, 2017.
- [14] M.R.W. Brake, C.R. Little, A.R. Lewis, M.T. O'Gorman, Reconciling whole joint models and the preservation of local kinematics, in: International Design Engineering Technical Conference, Cleveland, OH, August 2017, ASME.
- [15] M.R.W. Brake, C.W. Schwingshackl, P. Reuß, On the observed variability and repeatability in jointed structures, Mech. Syst. Signal Process. 129 (2019) 282–307.
- [16] M.R.W. Brake, An overview of constitutive models, in: The Mechanics of Jointed Structures, Springer, 2018, pp. 207-221.
- [17] M.P. Castanier, Y.C. Tan, C. Pierre, Characteristic constraint modes for component mode synthesis, AIAA J. 39 (6) (2001) 1182-1187.
- [18] S.B. Cooper, M. Rosatello, A. Mathis, K. Johnson, M.R.W. Brake, M.S. Allen, A.A. Ferri, D.R. Roettgen, B.R. Pacini, R.L. Mayes, Effect of far-field structure on joint properties, in: 35th International Modal Analysis Conference (IMAC XXXV), Garden Grove, CA, January 2017.
- [19] R.R. Craig, M.C.C. Bampton, Coupling of substructures for dynamic analyses, AIAA J. 6 (7) (1968) 1313–1319.
- [20] R.R. Craig, C.J. Chang, Free-interface methods of substructure coupling for dynamic analysis, AIAA J. 14 (1976) 1633-1635.
- [21] T. Dreher, N.N. Balaji, J. Groß, M.R.W. Brake, M. Krack, Gerrymandering for interfaces: Modeling the mechanics of jointed structures, in: 37th International Modal Analysis Conference (IMAC XXXVII), Orlando, FL, January 2019.
- [22] B. Etienne, Use of Generalized Interface Degrees of Freedom in Component Mode Synthesis, Information Scientifique et Technique et Publications, 1996
- [23] C.M. Firrone, S. Zucca, M.M. Gola, The effect of underplatform dampers on the forced response of bladed disks by a coupled static/dynamic harmonic balance method, Int. J. Non-Linear Mech. 46 (2011) 363–375.
- [24] L. Gaul, C.A. Brebbia. Computational Methods in Contact Mechanics IV. Computational Methods in Contact Mechanics, WIT Press, 1999. ISBN 9781853124655. URL URL:https://books.google.com/books?id=M6oeAQAAIAA]. .
- [25] L. Gaul, R. Nitsche, The role of friction in mechanical joints, ASME Appl. Mech. Rev. 54 (2001) 93–110.
- [26] J. Geisler, K. Willner, Modeling of jointed structures using zero thickness interface elements, Proc. Appl. Math. Mech. 7 (2007) 4050009–4050010.
- [27] J. Groß, R.M. Lacayo, J. Armand, M.R.W. Brake, C. Schwingshackl, P. Reuß, L. Salles, T. Truster, R.J. Kuether. A numerical round robin for the prediction of the dynamics of jointed structures, in: 34th International Modal Analysis Conference (IMAC XXXIV), Orlando, FL, January 2016.
- [28] W.C. Hurty, Dynamic analysis of structural systems using component modes, AIAA J. 3 (1960) 678-685.
- [29] D.J. Inman, Analysis and Report on SD2000: A Workshop to Determine Structural Dynamics Research for the Millenium:. Technical report, Defense Technical Information Center, Fort Belvoir, VA, April 2000. URL URL:http://www.dtic.mil/docs/citations/ADA376719..
- [30] S. Jain, P. Tiso, Simulation-free hyper-reduction for geometrically nonlinear structural dynamics: a quadratic manifold lifting approach, J. Comput. Nonlinear Dyn. 13 (7) (2018). ISSN 1555-1415. doi: 10.1115/1.4040021. .
- [31] S. Jain, P. Tiso, Hyper-reduction over nonlinear manifolds for large nonlinear mechanical systems, J. Comput. Nonlinear Dyn. 14 (8) (2019).
- [32] S. Jain, P. Tiso, J.B. Rutzmoser, D.J. Rixen, A quadratic manifold for model order reduction of nonlinear structural dynamics, Comput. Struct. 188 (2017) 80–94. ISSN 0045-7949. doi: 10.1016/j.compstruc.2017.04.005.
- [33] G. Karypis, V. Kumar, A fast and high quality multilevel scheme for partitioning irregular graphs, SIAM J. Sci. Comput. 20 (1) (1998) 359–392.
- [34] G. Karypis, V. Kumar. A software package for partitioning unstructured graphs, partitioning meshes, and computing fill-reducing orderings of sparse matrices. University of Minnesota, Department of Computer Science and Engineering, Army HPC Research Center, Minneapolis, MN, 1998.
- [35] H.K. Khalil, Nonlinear systems, Upper Saddle River (2002).
- [36] D. Krattiger, L. Wu, M. Zacharczuk, M. Buck, R.J. Kuether, M.S. Allen, P. Tiso, M.R.W. Brake, Interface reduction for hurty/craig-bampton substructured models: review and improvements, Mech. Syst. Signal Process. 114 (2019) 579–603. ISSN 0888-3270. doi: 10.1016/j.ymssp.2018.05.031.
- [37] V.N. Kublanovskaya, Analysis of singular matrix pencils, J. Soviet Math. 23 (1) (1983) 1939–1950. ISSN 1573-8795. doi: 10.1007/BF01093276. URL URL: https://doi.org/10.1007/BF01093276. .
- [38] R.J. Kuether, D.A. Najera, Parameter estimation of joint models using global optimization, in: Dynamics of Coupled Structures, vol. 4, Springer, 2017, pp. 29–39.
- [39] Y.L. Kuo, The enhanced r-refinement finite element analysis of two-dimensional elastic problems, J. Comput. Theor. Nanosci. 9 (7) (2012) 908–917. ISSN 1546-1955. .
- [40] R. Lacayo, L. Pesaresi, J. Groß, D. Fochler, J. Armand, L. Salles, C. Schwingshackl, M. Allen, M.R.W. Brake, Nonlinear modeling of structures with bolted joints: a comparison of two approaches based on a time-domain and frequency-domain solver, Mech. Syst. Signal Process. 114 (2019) 413–438.
- [41] R.M. Lacayo, M.S. Allen, Updating structural models containing nonlinear Iwan joints using quasi-static modal analysis, Mech. Syst. Signal Process. 118 (2019) 133–157. ISSN 08883270. doi: 10.1016/j.ymssp.2018.08.034.
- [42] J. Lang, W. Cao, W. Huang, R.D. Russell, A two-dimensional moving finite element method with local refinement based on a posteriori error estimates, Appl. Numer. Math. 46 (1) (2003) 75–94. ISSN 01689274. doi: 10.1016/S0168-9274(03)00013-8. URL URL:https://linkinghub.elsevier.com/retrieve/pii/S0168927403000138.
- [43] E. Lindberg, N.E. Hörlin, P. Göransson, Component mode synthesis using undeformed interface coupling modes to connect soft and stiff substructures, Shock Vib. 20 (1) (2013) 157–170. ISSN 1070-9622, 1875-9203. doi: 10.1155/2013/262354.
- [44] R.H. MacNeal, The NASTRAN theoretical manual, vol. 221. Scientific and Technical Information Office, National Aeronautics and Space, 1970..
- [45] Abaqus User Manual. Abaqus theory guide. Version, 6, 2014. .
- [46] A.T. Mathis, N.N. Balaji, R.J. Kuether, A.R. Brink, M.R.W. Brake, D.D. Quinn, A review of damping models for structures with mechanical joints, Appl. Mech. Rev. in press.

- [47] M. Mayer, L. Gaul, Modeling of contact interfaces using segment-to-segment-elements for FE vibration analysis, in: 23rd International Modal Analysis Conference (IMAC XXIII). Bethel. CT. 2005.
- [48] S. Medina, D. Nowell, D. Dini, Analytical and numerical models for tangential stiffness of rough elastic contacts, Tribol. Lett. 49 (1) (2013) 103–115. ISSN 1023-8883, 1573-2711. doi: 10.1007/s11249-012-0049-y.
- [49] R.D. Mindlin, Compliance of elastic bodies in contact, ASME J. Appl. Mech. 16 (1949) 259–268.
- [50] M. Mitra, S. Zucca, B.I. Epureanu, Adaptive microslip projection for reduction of frictional and contact nonlinearities in shrouded blisks, J. Computat. Nonlinear Dyn. 11 (4) (2016). ISSN 1555-1415. doi: 10.1115/1.4033003.
- [51] A. Quarteroni, A. Valli, Numerical Approximation of Partial Differential Equations. Springer Series in Computational Mathematics, Springer Berlin Heidelberg, 2008. ISBN 9783540852674.
- [52] D.J. Rixen, A dual Craig-Bampton method for dynamic substructuring, J. Comput. Appl. Math. 168 (2004) 383-391.
- [53] J.B. Rutzmoser, D.J. Rixen, A lean and efficient snapshot generation technique for the hyper-reduction of nonlinear structural dynamics, Comput. Methods Appl. Mech. Eng. 325 (2017) 330–349.
- [54] J.B. Rutzmoser, D.J. Rixen, P. Tiso, S. Jain, Generalization of quadratic manifolds for reduced order modeling of nonlinear structural dynamics, Comput. Struct. 192 (2017) 196–209.
- [55] D. Ryckelynck, A priori hyperreduction method: an adaptive approach, J. Comput. Phys. 202 (1) (2005) 346–366. ISSN 00219991. doi: 10.1016/j. jcp.2004.07.015.
- [56] S.E. Schaeffer, Graph clustering, Comput. Sci. Rev. 1 (1) (2007) 27–64. ISSN 1574-0137. doi: 10.1016/j.cosrev.2007.05.001. URL URL:http://www.sciencedirect.com/science/article/pii/S1574013707000020.
- [57] D.J. Segalman, Modelling joint friction in structural dynamics, Struct. Control Health Monit. 13 (1) (2006) 430–453. ISSN 1545-2255, 1545-2263. doi: 10.1002/stc.119.
- [58] N.G. Trillos, D. Slepcev, A variational approach to the consistency of spectral clustering, Appl. Comput. Harmonic Anal. 45 (2) (2018) 239–281. ISSN 1063-5203. doi: 10.1016/j.acha.2016.09.003. URL URL:http://www.sciencedirect.com/science/article/pii/S106352031630063X.
- [59] C. Walshaw, M. Cross, Mesh partitioning: a multilevel balancing and refinement algorithm, SIAM J. Sci. Comput. 22 (1) (2000) 63–80. ISSN 1064-8275, 1095-7197. doi: 10.1137/S1064827598337373.
- [60] K. Willner, L. Gaul, A penalty approach for contact description by FEM based on interface physics, in: Contact Mechanics II, volume 7 of WIT Transactions on Engineering Sciences, Ferrera, Italy, July 1995, pp. 1743–3533. ISBN 978-1-85312-326-9. doi: 10.2495/CON950301.
- [61] P. Wriggers, G. Zavarise, Computational contact mechanics, Encycl. Comput. Mech. (2004).
- [62] Stefano Zucca, Christian Maria Firrone, Nonlinear dynamics of mechanical systems with friction contacts: coupled static and dynamic Multi-Harmonic Balance Method and multiple solutions, J. Sound Vib. 333 (3) (2014) 916–926. ISSN 0022460X. doi: 10.1016/j.jsv.2013.09.032. URL URL:http://linkinghub.elsevier.com/retrieve/pii/S0022460X13007864.